Interphase characterization by means of ultrasound methods : application to periprosthetic tissues

Ilaria Scala

To cite this version:

Ilaria Scala. Interphase characterization by means of ultrasound methods : application to periprosthetic tissues. Signal and Image Processing. Université Paris-Est, 2018. English. NNT : 2018PESC1107 . tel-02137406

HAL Id: tel-02137406
https://theses.hal.science/tel-02137406

Submitted on 23 May 2019

UNIVERSITÉ PARIS-EST CRÉTEIL

ECOLE DOCTORALE SIE : Sciences Ingénierie et Environnement

Thèse pour l'obtention du grade de

DOCTEUR DE L'UNIVERSITÉ PARIS-EST

Spécialité : Mécanique

ILARIA SCALA

CARACTÉRISATION D'INTERPHASE PAR DES MÉTHODES ULTRASONORES : APPLICATION AUX TISSUS PÉRI-PROTHÉTIQUES

Thèse dirigée par

Salah NAILI

et Giuseppe ROSI

Composition du jury :

Mme. Cécile BARON	Chargé de Recherche au CNRS, ISM, Marseille	Rapporteur
M. Jean-Francois GANGHOFFER	Professeur, Université de Lorraine, LEM3	Président
M. Pierre LEVITZ	Directeur de Recherche au CNRS, PHENIX	Examinateur
Mme. Angela MADEO	Professeur, INSA Lyon, GEOMAS	Rapporteur
M. Salah NAILI	Professeur, Université Paris-Est, Créteil, MSME	Directeur de thèse
M. Giuseppe ROSI	Maître de Conférences, Université Paris-Est, Créteil, MSME	Co-encadrant de thèse

Acknowledgements

First, I would like to express my gratitude to my PhD Supervisor, Prof. Salah Naili. I am grateful for its availability and its wise advise. He welcomed me into the laboratory of which he is director, and he gave me the resources to work in the better condition. Additionally, he also gave me the opportunity to teach, which made me more confident at both professional and personal level.

Then, I would thank my PhD co-Supervisor, Giuseppe Rosi. He has been the first person I met in the laboratory and it is in large measure thanks to him if I have started and challenged myself with this multidisciplinary PhD. I thank him for his knowledge and advice which guided me during these three years.

I would like to thank the members of the jury who have done me the honor of evaluating my work: Mrs. Cécile Baron and Mrs. Angela Madeo as rapporteurs; M. Jean-François Ganghoffer and M. Pierre Levitz as examiners.

I thank with deep gratitude my collogues all, companions of adventure, some of them became, above all, friends during this long journey. Thanks to Romain, for his crucial support during these three years, and to Erica, for being a reference point for me. Their friendship made me able to overcome the obstacles, especially during the first year, and to never feel alone. Thanks to Alexis for its kindness and for the great time spent togheter. I want to thank also the others PhD students that I met during this path: Madge (someone really special to which I wish all the best), Ivan, Manon, Yoann (I have really appreciated the time spent togheter during the conference in Dublin), Davide, Son, Antoisse, Hai and Bao.

Therefore, I would like to thank all the members of the MSME laboratory for welcoming and always be nice with me. A big thank to Hung, for his valuable help/support (professional and personal) and its joyfulness, and to Isabelle, for her joy of life, her understanding and her empathy.

Thank you to my Italian friends for being present for me, even after my depar-

ture, in both good and bad times. In particular, thanks to Karen, Ilaria and Alice.

Thank you Antoine for all the love, the support and the care you constantly give to me. You are the best thing that happens to me during these three years.

Last but not least, the deepest gratitude is to my family. You always supported me and my choices, even if it means to move abroad. Your love and your trust are the most important to me.

Contents

Chapitre 1

Introduction générale

1.1 Contexte du projet

Ce travail de thèse s'inscrit dans la problématique complexe de la caractérisation ultrasonore de l'interface os-implant.
Utiliser des ultrasons dans le cadre de la caractérisation du tissu osseux est une pratique assez répandue dans le domaine médical pour plusieurs raisons. D'abord les ultrasons sont parmi les techniques ayant la capacité de fournir des informations sur les propriétés biomécaniques de l'os, qui autrement ne seraient pas accessibles. Selon la fréquence utilisée, différentes échelles des propriétés du tissu osseux sont explorées. De plus, les ultrasons sont désormais couramment utilisés en clinique pour leurs caractères non invasif et non destructif, leur capacité à fournir des résultats rapidement, leur facilité d'utilisation et leur transportabilité par rapport à d'autres moyens de diagnostic (*e.g.* les techniques basées sur les rayons X). De plus, cette technique est non ionisante et relativement peu coûteuse. Ce domaine de recherche est relativement récent et il génère un intérêt croissant dans la communauté scientifique aussi bien en acoustique, imagerie médicale, mathématiques appliquées, mécanique, biomécanique, ingénierie biomédicale et biologique.

Cependant, l'interface os-implant reste encore très difficile à caractériser. Cette interface consiste en une région de transition entre l'os et l'implant. Pour cette raison, plus que d'interface, nous allons parler d'*interphase*. C'est dans cette zone qu'a lieu le processus d'ostéointegration, qui, en accord avec la définition de Brånemark (1977) peut être défini comme l'établissement d'un contact "intime" à l'interface entre l'os et l'implant [20]. Cette interphase joue un rôle crucial puisque ses propriétés mécaniques affectent considérablement la tenue à long-terme des implants (couramment utilisés en chirurgie pour suppléer une fonction détériorée de l'organe originel). De plus, le tissu néoformé, comme le tissu osseux en général, est un tissu vivant multi échelle, en raison de sa hiérarchie structurale complexe et

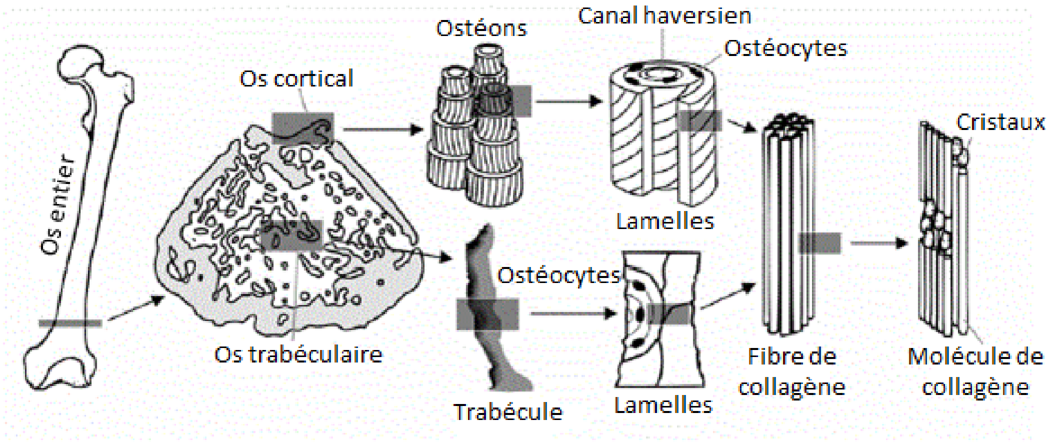

FIGURE 1.1 – Représentation schématique des différentes échelles qui composent la structure hiérarchique de l'os (adaptée partir de [22]).

son organisation à plusieurs niveaux, chacun avec ses interactions spécifiques. Ces niveaux d'échelles induisent les fonctions biologiques et mécaniques, et peuvent être divisées comme suit :

- l'échelle macro, qui représente l'os entier (cm) ;
- l'échelle méso, qui comprend l'os cortical et trabéculaire (mm) ;
- l'échelle micro, qui représente l'ostéon et la trabécule ($\sim$ 10-500 μm) ;
- l'échelle sous-micro, celle des lamellae ($\sim$ 1-10 μm) ;
- l'échelle nano, à laquelle on trouve les micro fibrilles, les fibrilles et les fibres ($\sim$ 100 nm - 1 μm) ;
- l'échelle sous-nano, où nous trouvons les cristaux d'hydroxyapatite (HA) et les molécules de tropocollagène (TC) ($\sim$ 300 nm) [9].

L'objectif de ce travail est d'utiliser des modèles à l'échelle macro qui prennent toutefois en compte ce qu'il se passe à l'échelle inférieure (*i.e.* l'échelle méso). Une représentation schématique de la nature multi échelle de l'os est illustrée dans la Fig. 1.1.

Ensuite, il est aussi important de prendre en compte que, dans le système que nous considérons, un implant se substitue à un organe dans ses propriétés physiques et dans ses fonctionnalités. Considérons, par exemple, un implant dentaire. Comme représenté dans la Fig. 1.2, l'implant fait office de racine artificielle insérée dans l'os de la mâchoire. Un pilier prothétique intermédiaire est vissé dans l'implant et sort de la gencive pour servir d'ancrage à la couronne. La principale différence par rapport à une dent est la façon dont l'implant est en contact avec les tissus des gencives et de l'os environnant.

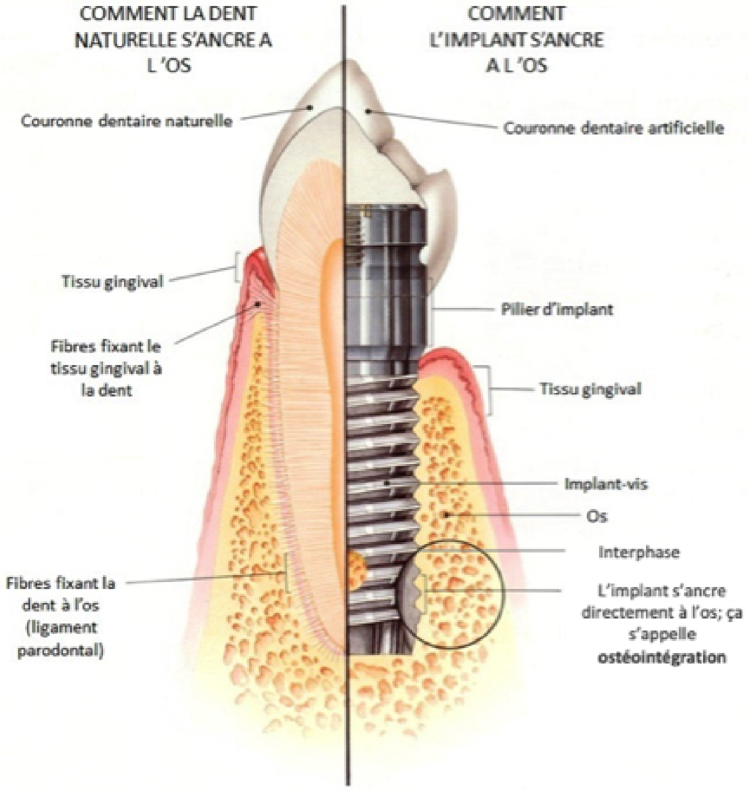

FIGURE 1.2 – Représentation des différentes parties d'une dent et de l'implant qui la remplace (adaptée de [104]).

Nous avons donc trois domaines principaux : l'implant, l'interphase et le tissu osseux. Nous allons maintenant nous concentrer sur ce dernier. Le tissu osseux est un tissu connectif, caractérisé par une matrice extracellulaire calcifiée qui lui donne sa rigidité ainsi que sa résistance mécanique. Il peut être ou pas lamellaire, selon la disposition des fibres de collagène. Le tissu non lamellaire peut être trouvé dans l'embryon et dans le fœtus, ou aussi dans l'os qui se reforme de façon temporaire tout de suite après une fracture. Par ailleurs, le tissu lamellaire est le résultat de plusieurs itérations de remaniement du tissu non lamellaire, présent chez les adultes. Le tissu osseux lamellaire, à son tour, se répartit en os spongieux (ou trabéculaire) et os compact (ou cortical) (Fig. 1.3). L'os trabéculaire est principalement localisé dans la partie interne de l'os. Comme son nom vernaculaire l'indique, il ressemble à une éponge et présente un espace entre les trabécules. Ces trabécules sont différemment orientées et entrecroisées. De plus, elles délimitent les cavités de moelle osseuse. L'os trabéculaire présente donc une structure alvéolaire,

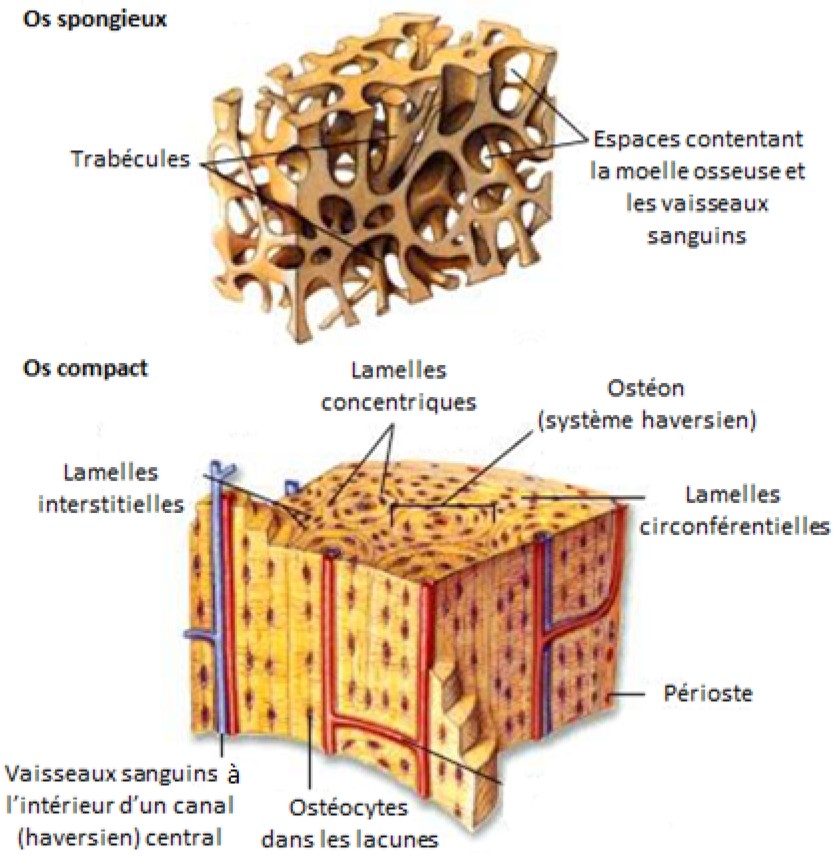

Figure 1.3 – Os spongieux (ou trabéculaire) et os compact (ou cortical).

ce qui le rend moins dense. A cause de la distribution des trabécules, qui dépend des lignes de charge, il peut supporter des sollicitations venant de différentes directions. Pour sa part, l'os compact forme la partie externe de l'os. Il s'agit d'un os dur, solide et compact car, contrairement à l'os trabéculaire, il ne présente pas de cavités macroscopiques significatives en dimension. Il y a des petits canaux réservés aux vaisseaux sanguins et aux cellules qui le maintiennent en vie.

La caractérisation de l'interphase os-implant est donc un sujet complexe. A ce jour, il n'existe pas de méthodes satisfaisantes pour le suivi des propriétés de cette interphase. En effet, même si les implants (en titane) sont utilisés dans divers champs d'applications (*e.g.* chirurgie orthopédique, maxillofaciale, dentaire), de nombreux échecs chirurgicaux sont toujours observés. Les échecs implantaires sont dûs à une mauvaise ou incomplète compréhension de la complexité du tissu osseux.

Cette thèse vise donc à développer et valider numériquement des modèles méca-

niques originaux ainsi que des méthodes de traitement du signal pour caractériser quantitativement les propriétés mécaniques et microstructurales du système os-implant, en utilisant des méthodes ultrasonores. En effet, puisque il s'agit d'une structure multi échelle (cf. Fig. 1.1), un travail de modélisation et/ou d'interprétation du signal ultrasonore s'avère cruciale.
Ici, la complexité du comportement de l'os néoformé peut être prise en compte en considérant les propriétés d'une interphase dont l'épaisseur est très fine. On rappelle que les difficultés principales résident dans le fait que cette interphase est un milieu complexe très hétérogène, mélange de phases fluides et solides dont les propriétés (densité de masse, rigidité, etc.) évoluent au cours du temps. Afin de modéliser proprement l'interaction entre les ultrasons et le système composé de l'implant, de l'interphase et du tissu osseux, il est donc nécessaire de développer des modèles adaptés, capables de prendre en compte la forte hétérogénéité de ce système.

1.2 Méthodologie

L'analyse des phénomènes *via* le traitement du signal ultrasonore permet de relier les principales caractéristiques des signaux aux propriétés physiques du milieu. Cependant, ces phénomènes liés à la propagation d'ondes ultrasonores dans un milieu hétérogène sont très complexes. Pour cette raison, la caractérisation de l'interphase tissu osseux-implant implique tout d'abord une compréhension profonde des phénomènes mis en jeu lors de la propagation des ultrasons. Donc, en amont du travail de modélisation, il est crucial de déterminer quels sont les phénomènes prépondérants.
En raison de la complexité du problème, une modélisation du comportement du tissu osseux s'avère essentielle. Cela va nous aider ensuite à décrire plus précisément le tissu osseux qui entoure l'implant. L'objectif est donc de fournir des modèles relativement simples, mais qui permettent de prendre en compte le comportement multi échelle du tissu osseux (cf. Fig. 1.1). Pour faire cela, nous allons d'abord investiguer l'interaction d'une onde ultrasonore avec le tissu osseux. Dans ce contexte, on utilise traditionnellement la théorie de Biot, qui est considérée comme pionnière dans la mécanique des milieux poreux [16, 17, 18]. Cependant, quand le milieu est très poreux et que la microstructure commence à jouer un rôle non négligeable, cette théorie n'est plus assez précise [5]. Afin de prendre en compte les effets dus à la microstructure, un modèle continu généralisé a été utilisé ici [102]. Plus précisément, il s'agit de la stratégie de modélisation dite du *deuxième gradient*, qui comporte l'introduction de deux termes supplémentaires dans l'équation de la conservation de l'énergie qui font intervenir des dérivées d'ordre supérieur du champ de déplacement. Dans ce contexte, un test de transmission/réflexion a

été réalisé sur un échantillon poroélastique immergé dans un fluide. Cela a mis en évidence la fiabilité du modèle. En effet, les paramètres ajoutés pour prendre en compte les effets dus à la microstructure influencent significativement la réflexion ainsi que la transmission de l'onde. En plus, l'analyse de dispersion a montré un comportement en accord avec celui obtenu dans les expériences pour un échantillon poreux. Une fois ce modèle validé, on s'intéresse à l'interaction entre les ondes ultrasonores et l'interphase. Pour cela, l'interphase entre l'os et l'implant a été modélisée comme une couche avec des propriétés élastiques et inertielles. De cette façon, on prend en compte la complexité introduite par la présence de l'os néoformé. Les effets d'une transition entre un milieu homogène et un milieu continu microstructuré sur les propriétés de réflexion ont été étudiés.
Ensuite, et toujours dans le but de caractériser l'interphase os-implant, une technique avancée de traitement du signal a été utilisée *via* l'approche multifractale. Dans le domaine médical, cette approche a déjà commencé à être exploitée afin de caractériser le tissu osseux [43, 103, 115] ou de discriminer, par exemple, un sujet sain d'un sujet ostéoporotique [40, 61]. Cependant, l'analyse multifractale n'a jamais été utilisée dans le but d'évaluer la stabilité d'un implant dentaire. On parle de stabilité d'un implant lorsque celui ci est capable de supporter les chargements mécaniques du quotidien, sans altération ni de ses propriétés ni de celles du tissu osseux environnant. Dans ce contexte, la caractérisation à partir des techniques de traitement du signal est rendue difficile surtout pour deux raisons. D'un côté, il faut considérer que pour les expériences le nombre de capteurs est limité et que l'atténuation due aux tissus osseux est non négligeable, ce qui est une source de perturbation des signaux. De l'autre, puisque ces signaux sont issus des réflexions multiples des ondes ultrasonores ayant lieu à l'interphase, leur nature et leur interprétation sont complexes.

1.3 Résumé des chapitres

1.3.1 Contenu du chapitre 2

Le travail présenté dans ce chapitre a donné lieu à la production d'un article scientifique dans le journal *Zeitschrift für angewandte Mathematik und Physik* [102] et à une communication dans un congrès à comité de lecture avec actes publiés [105].
Ici, on utilise la stratégie de modélisation du deuxième gradient, permettant de prendre en compte les effets dus à la présence de la microstructure. En effet, lorsque la longueur d'onde s'approche de la taille caractéristique de la microstrocture, le modèle classique de Biot n'est pas assez précis. On considère alors une généralisation de la théorie de Biot, le deuxième gradient, qui ajoute les dérivées

d'ordre supérieur du champ de déplacement. De cette façon, l'équation de bilan ainsi que les conditions limites contiennent des termes liés à la microstructure. Pour cette étude la configuration géométrique consiste en un milieu poroélastique (*e.g.* l'os) immergé dans un domaine fluide (*e.g.* l'eau) entre une source et un récepteur (Fig. 1.4).

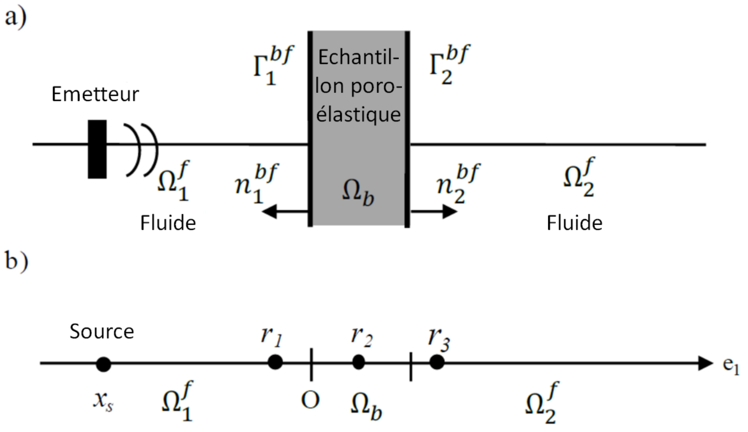

FIGURE 1.4 – Configuration d'intérêt : a) schéma du test de transmission/réflexion ; b) modèle unidimensionnel, où les positions approximatives des récepteurs r_1, r_2 et r_3 sont indiquées.

On determine la réponse de la propagation d'une onde plane unidimensionnelle dans le domaine temporel en suivant deux méthodes : d'un côté avec les transformées de Laplace et Fourier, de l'autre avec la méthode par éléments finis (*via* le logiciel commercial Comsol Multiphysics). La stratégie numérique a été validée. Les résultats montrent que les effets additionnels dus à l'insertion du deuxième gradient sont bien visibles dans la réponse temporelle des champs de pression. De plus, les résultats sont en accord avec ce qu'on peut observer expérimentalement [63]. En effet, on observe nettement le phénomène de rétro diffusion des ondes (*backscatter* en anglais) et une dépendance de la vitesse de phase et de l'atténuation sur la fréquence.

1.3.2 Contenu du chapitre 3

Le travail présenté dans ce chapitre a donné lieu à la production d'un article scientifique dans le journal *Continuum Mechanics and Thermodynamics* [108]. Ici, l'objectif est la modélisation d'une interphase comme une interface (pas d'épaisseur) en gardant les informations de l'interphase d'origine. Afin d'éviter que le détail géométrique de l'interphase (*i.e.* sa taille caractéristique par rapport à sa longueur d'onde) engendre des maillages trop fins, nous voulons donc réduire l'interphase, représentant notre référence, à une interface équivalente, qui est un modèle réduit (cf. Fig. 1.5). Pour faire cela, seules les propriétés d'élasticité de l'interphase

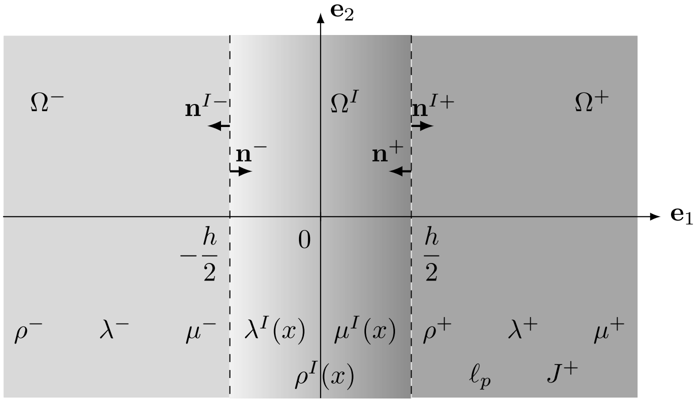

(a) Interphase finie

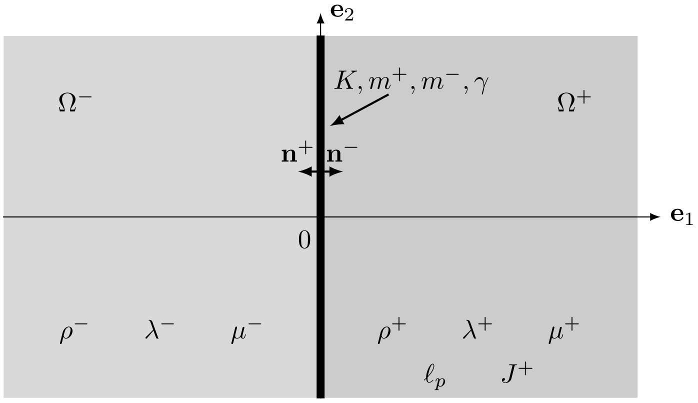

(b) Interface

FIGURE 1.5 – Configurations géométriques représentant a) l'interphase finie (Ω^I) et b) l'interface équivalent entre l'os (Ω^+) et l'implant (Ω^-).

sont habituellement considérées. La façon dont la masse est distribuée n'est donc pas prise en considération. Dans l'étude présentée dans ce chapitre, nous considérons aussi les propriétés inertielles pour décrire l'interface.

On va donc avoir une configuration dans laquelle une interface s'interpose entre un milieu homogène et un milieu hétérogène microstructuré. Dans le domaine biomécanique, cette configuration peut représenter une interface entre l'implant (milieu homogène) et l'os (milieu hétérogène microstructuré). Afin d'éviter un brusque changement des propriétés d'un milieu à l'autre, on considère une transition entre les deux. L'interface présente donc un profil de densité non uniforme. Cela se rap-

proche de la réalité, où le remodelage osseux qui a lieu entre l'os et l'implant engendre une distribution non constante du tissu osseux néoformé.
Les résultats pour deux types de profils de densité, affine et quadratique, sont représentés. Les courbes des coefficients de réflexion reproduisent bien le modèle de référence à basses fréquences. Le modèle est donc validé.

1.3.3 Contenu du chapitre 4

Le travail présenté dans ce dernier chapitre a donné lieu à la production d'un article scientifique dans le journal *Biomedical Signal Processing & Control* [107] et à une communication dans un congrès à comité de lecture avec actes publiés [106]. Ici, on s'intéresse à la caractérisation du système os-implant à l'aide de méthodes avancées de traitement du signal. Plus précisément, c'est l'approche multifractale qui a été utilisée afin d'extraire des informations significatives concernant la stabilité dite primaire à partir des signaux ultrasonores provenant d'une sonde vissée dans l'implant.
Dans le cadre de la propagation ultrasonore dans un milieu hétérogène, l'utilisation de l'approche multifractale n'est pas très fréquent. De plus, l'idée d'exploiter la structure multifractale du signal afin d'évaluer la stabilité de l'implant est nouvelle.
La configuration géométrique présente un implant (dentaire) initialement entièrement vissé dans l'os (voir Fig. 1.6). Cet implant est ensuite progressivement dévissé, afin d'introduire une diminution de la stabilité de plus en plus significative dans le système. Cette configuration a été utilisée dans les expériences ainsi que dans les simulations. Les résultats numériques ont été obtenus à l'aide du logiciel commercial Comsol Multiphysics. De plus, dans les simulations numériques, des couches absorbantes parfaitement adaptées ont été considérés dans la réalisation de cette configuration géométrique afin de faire en sorte que les ondes incidentes ne se réfléchissent pas à l'interface. Afin de simplifier les calculs, une configuration axisymétrique a été considérée. Les résultats expérimentaux et numériques ont donc été comparés et analysés. En particulier, dans le cadre des méthodes multi échelles, l'observation de la valeur moyenne des fonctions d'échelle a été exploitée. La comparaison avec l'indicateur de stabilité développé au sein du laboratoire a montré une cohérence. De plus, une étude de sensibilité a été conduite afin d'investiguer l'influence de deux paramètres : la fréquence centrale et la densité de l'os trabéculaire. Suite aux résultats, il a été conclu qu'il n'y a pas d'influence significative.

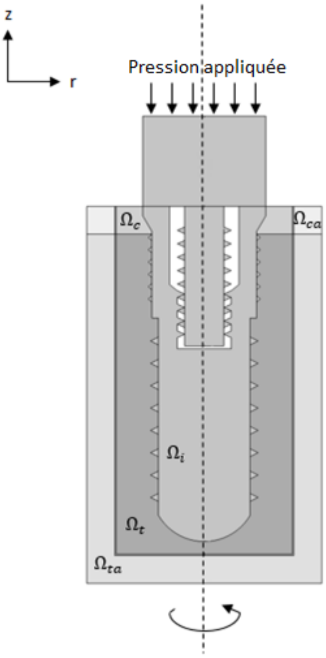

FIGURE 1.6 – Section transversale de la configuration géométrique 3-D [107]. Les domaines sont différenciés avec les indices : l'os trabéculaire (Ω_t), l'os corticale (Ω_c), l'implant (Ω_i), et les couches absorbantes associées à l'os trabéculaire et à l'os cortical (respectivement Ω_{ta} et Ω_{ca}).

Chapter 2

Wave propagation in second gradient poroelastic medium with micro inertia: closed-form and finite element solutions

---

The work presented in this chapter is issued from the following publication:

> G. Rosi, I. Scala, V.-H. Nguyen, and S. Naili. Wave propagation in strain gradient poroelastic medium with microinertia: closed-form and finite element solutions. *Zeitschrift für angewandte Mathematik und Physik*, 68(3): 58, 2017.

Abstract

This chapter is about ultrasonic wave propagation in microstructured porous media. The classic Biot's model is enriched using a second gradient approach to be able to capture high order effects when the wavelength approaches the characteristic size of the microstructure. In order to reproduce actual transmission/reflection experiments performed on poroelastic samples, and to validate the choice of the model, the computation of the time domain response is necessary, as it allows for a direct comparison with experimental results. For obtaining the time response, we use two strategies: on one hand we compute the closed form solution by using the Laplace and Fourier transforms techniques; on the other hand we used a finite element method. The results are presented for a transmission/reflection test performed on a poroelastic sample immersed in water. The effects introduced by the second gradient terms are visible in the time response, and in agreement with experimental observations. The results can be exploited in the characterization of mechanical properties of poroelastic media by enhancing the reliability of quantitative ultrasound techniques.

Keywords: analytical solution, cancellous bone, FEM, plane wave, poroelasticity, second gradient, ultrasound.

2.1 Introduction

For several engineering applications, including *e.g.* geotechnics and biomechanics, the study of wave propagation in a fluid-saturated poroelastic medium is an important subject of major interest. In this framework, the classic starting point is represented by the Biot's seminal works [17]. From here, several analytic and numerical studies have been carried out [28, 89, 109, 120]. However, it is well known that for highly porous materials, and in all cases when the microstructure starts playing a role in the observed phenomena (*e.g.* when the characteristic size of the perturbation approaches the size of the pores), Biot's theory is not accurate enough, as it does not directly take into account microstructure [5]. In such situation, many studies have been carried out by using image-based models, which contain all details of microstructures, and as consequence, may provide a good prediction of wave phenomena induced by microstructure complexities. In this framework, simulations have been performed by using Finite Difference in Time Domain method (FDTD) or Finite Element Method [77, 117, 119]. However, simulations on image-based models require very high computational costs, and are only applicable when considering small samples.

In our approach we assume that the microstructure is taken into account with a generalization of the Biot's theory that introduces gradients of elastic strain in the potential energy, as well as the gradients of velocities in the kinetic energy. The most important consequence in adding these new terms to the energy is that the resulting balance equation and boundary conditions will naturally involve additional terms, now related to the microstructure. From the point of view of wave propagation, the main result is that phase velocity and attenuation now have an additional dependence on frequency. This approach is conceptually different from introducing a dynamic permeability, as it involves dynamic properties of the solid matrix at the microscopic scale (through the addition of characteristic internal lengths), rather than the effects of its geometry on fluid flow. The use of second gradient (or equivalently strain gradient) within the poroelastic framework is not new. A detailed variational derivation of the balance and boundary equations can be found in [29, 32, 69, 111, 112]. Applications to well-known problems of soil dynamics, such as consolidation tests, show that the theory allows for a better agreement with experiments with respect to the classical Biot's theory (see *e.g.* [69, 87, 88]). Wave propagation has also been studied, (see *e.g.* [70, 97]), and the rich effects at the boundaries were described. In the aforementioned papers, the authors only deal with harmonic excitations. However, most of the reflection/transmission tests performed on poroelastic specimens use pulse excitation, and thus a transient analysis of the problem is more appropriate. The transient response is studied in [88] in the case of a poroelastic column, but not in the framework of a reflection/transmission problem. Moreover, the transient response allows to see more in detail the dispersion effects, and the results are more easily comparable with experimental signals. The interest in studying the harmonic response is of course still high, and the two approaches can be efficiently combined.

One of the main motivations of the present study is the increasing popularity of Quantitative Ultrasound (QUS) techniques. In particular QUS techniques have been more and more appreciated not only because they are able to investigate bone mass, but also because they are able to give information about its mechanical quality. The measure depends on an estimation of phase velocity and on the attenuation of the transmitted wave through the bone. Many devices for *in vitro* tests, based on this technique, refer to through-transmission measures in order to establish the broadband ultrasound attenuation and the phase velocity [37, 57, 58, 59, 83, 85, 131]. That of transverse transmission is a common test, according to which a poroelastic (*e.g.* bone) specimen is inserted in water between a source and a receiver which can detect waves. Reflected and transmitted waves characteristics obviously depend on the internal structure of the specimen. Objective of this paper is going a step further towards the interpretation of the QUS' experimental results, starting from the work carried out in [78, 79, 80, 81, 82].

In order to verify if the model is appropriate to describe the aforementioned phenomena, it is important to compute the time domain response. In this paper, we use two techniques: on one hand we compute the closed form solution by using the Laplace and Fourier transforms techniques; on the other hand we use a finite element method.

The chapter is structured as follows. After this introduction, the problem is presented in Section 2.2. Object of Section 2.3 is the derivation of the governing equations and boundary conditions. In Section 2.4 the one-dimensional plane wave propagation problem is presented, and the closed-form solution is derived. Section 2.5 is devoted to the presentation of the variational equations that will be used for computing the finite element solution. Finally, in Section 2.6, the results of the numerical simulations on a case study are presented and discussed. Section 2.7 contains conclusions and perspectives.

2.2 Statement of the problem

The geometrical configuration considered in this problem consists of two half-spaces, Ω_1^f and Ω_2^f, and a poroelastic layer in the middle, which occupies the domain Ω^b of thickness L in the direction $\underline{e}_1$ and unbounded with respect to the other two directions. The two plane interfaces between the poroelastic layer (Ω^b) and the fluid domains (Ω_1^f and Ω_2^f) are denoted by Γ_1^{bf} and Γ_2^{bf}, respectively.

In Fig. 2.1a, a 2D scheme of the test is represented. An acoustic source is located in the fluid domain Ω_1^f, while three receivers r_1, r_2 and r_3 are located in the domains Ω_1^f, Ω^b and Ω_2^f, respectively. We assume that the beam axis, which defines the propagation direction of the wave, coincides with the axis $\underline{e}_1$. Since we are interested in the propagation of plane longitudinal (pressure) waves, the problem will be simplified by taking into account a one-dimensional geometry, as shown in Fig. 2.1b. This choice does not influence the generality of the results.

In what follows we will use an index notation. Thus, by considering a general vector a_i, with respect to an orthonormal Cartesian basis, we will denote, for example, the spatial gradient by a comma (*i.e.* $a_{i,j}$), the divergence as $a_{i,i}$ and the curl as $\epsilon_{ijk}a_{jk}$, where ϵ_{ijk} is the Levi-Civita symbol.

2.3 Governing equations

In this section, we will display the governing equations in all different domains separately.

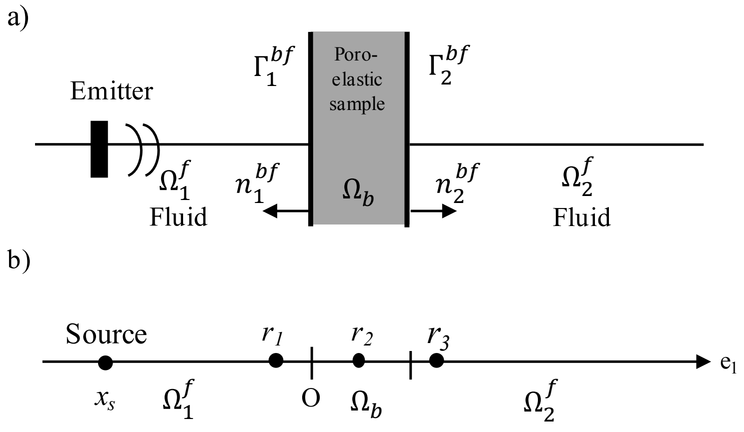

Figure 2.1 – Configuration of interest: a) sketch of the transmission/reflection test; b) One-dimensional model, with highlighted the approximate location of the receivers r_1, r_2 and r_3.

2.3.1 Governing equations in fluid domains

The fluids in the domains Ω_1^f and Ω_2^f are modeled as inviscid acoustic fluids and are supposed to be identical. Thus, the wave equation for this fluid may be expressed in terms of the respective pressure fields p_i ($i = 1, 2$, with reference to the fluid domain considered) as

$$\ddot{p}_i - c_f^2 (p_i)_{,jj} = 0, \tag{2.1}$$

where $c_f = \sqrt{\frac{K_f}{\rho_f}}$ is the speed of sound in the fluid at equilibrium, K_f is the bulk modulus of the fluid, and ρ_f is the mass density of the fluid at equilibrium.

2.3.2 Governing equations in the porous second gradient solid

In order to describe the behavior of a microstructured fluid saturated porous material, an enriched theory of anisotropic poroelasticity is taken into account. The model we present here is based on the well known model of Biot [17]. With the aim of describing the behaviour of a homogeneous or slightly heterogeneous anisotropic medium, the classical Biot theory is enough accurate. However, with increased frequency or wavenumber, it is not able to capture all the relevant phenomena.
The second gradient, also called strain gradient, is useful to take into account the influence of local micro-heterogeneities on the behavior of the continuum at

macroscopic level [86, 87]. It contains the first strain gradient as a particular case, as we will show later. The second gradient theory has already been used in the reflection/transmission problems [30, 49, 95, 98, 99] in frequency domain and its features have been found to be useful to capture the behavior at high frequency.

In the following, for describing the linear dynamic behavior of the considered poroelastic medium, we denote the Lagrangian displacement vector fields of the solid skeleton and of the fluid as u_i and $(u_f)_i$, respectively. The relative displacement of the fluid with respect to the solid skeleton (weighted by the porosity ϕ) is $w_i = \phi((u_f)_i - u_i)$. For a second gradient porous media, the equations of motion read as

$$\left(\sigma_{ij} - \tau_{ijk,k}\right)_{,j} = \rho \ddot{u}_i + \rho_f \ddot{w}_i - \eta(\ddot{u}_{i,j})_{,j}, \tag{2.2}$$

$$-p_{,i} = \rho_f \ddot{u}_i + k_{ij}^{-1} \dot{w}_j + b_{ij} \ddot{w}_j, \tag{2.3}$$

where σ_{ij} is the stress tensor, τ_{ijk} the hyperstress tensor, p is the interstitial pore pressure, $\rho = \phi\rho_f + (1-\phi)\rho_s$ is the mass density of the mixture, ρ_s and ρ_f are respectively the mass densities of the solid skeleton and of the fluid, ϕ is the porosity, k_{ij} is a symmetric second-order and frequency-dependent tensor that represents the permeability, and the tensor b_{ij} is defined as $b_{ij} = (\rho_f a_{ij})/\phi$ where a_{ij} represents the tortuosity tensor. More details about the variational derivation of Eqs. (2.2) and (2.3) can be found in [86]. As shown in Eq. (2.2), unlike the previous studies on this subject, here we do not neglect the term of micro-inertia (*i.e.* $\eta \neq 0$) in the equations describing wave propagation.

The constitutive laws for an anisotropic linear poroelastic material are well known, and given by

$$\sigma_{ij} = C_{ijkl}\varepsilon_{kl} - \alpha_{ij}\, p, \tag{2.4a}$$

$$-p = M(w_{i,i} + \alpha_{ij}\varepsilon_{ij}), \tag{2.4b}$$

where C_{ijkl} is the elasticity fourth-order tensor of drained porous material, α_{ij} is a symmetric second-order tensor which represents the Biot effective tensor, M is the Biot scalar modulus, ε_{ij} is the infinitesimal strain tensor, which is defined as the symmetric part of $u_{i,j}$. Since we place ourselves in the case of a centrosymmetric material, no coupling is present between the stress tensor σ_{ij} and the gradient of the strain tensor.

More attention should be devoted to the expression of the constitutive law for the hyperstress tensor. In the most general form, always in the case of a centrosymmetric material, this law reads

$$\tau_{ijk} = A_{ijklmn}\varepsilon_{lm,n}, \tag{2.5}$$

where A_{ijklmn} is a sixth order tensor (see [8] for details concerning its matrix representations). For the sake of simplicity, in this work, we consider a constitutive law that shares the symmetries of the one linking the drained stress tensor to the strain tensor, that introduces only one characteristic length ℓ

$$\tau_{ijk} = \ell^2 C_{ijkl} \varepsilon_{jk,l}. \tag{2.6}$$

This ansatz is justified by the simplified 1D problem that we aim to study, but when dealing with 2D or 3D problems a more complete form should be used [6, 95].

2.3.3 Continuity conditions at interfaces

We suppose an open pore condition at the interfaces between fluids and porous solid. Then the interface conditions between the poroelastic solid and the i^{th} fluid, for $i = 1, 2$, read

- continuity of pressure

$$p = p_i, \tag{2.7}$$

- consequence of the continuity of normal velocity

$$(p_{,i} + \rho(\ddot{w}_i + \ddot{u}_i))n_i = 0, \tag{2.8}$$

- continuity of stress fields

$$t_i = -p n_i, \tag{2.9}$$

- vanishing hypertraction

$$R_i = 0, \tag{2.10}$$

where the traction t_i and hypertraction R_i vectors are given by

$$t_i = (\sigma_{ij} - \tau_{ijk,k} + \eta \ddot{u}_{i,j})n_j - P_{ml}(P_{mj}\tau_{ijk}n_k)_{,l}, \tag{2.11}$$

$$R_i = \tau_{ijk} n_j n_k, \tag{2.12}$$

where it has been introduced the projector onto the surface of normal unit vector n_i. If we denote as δ_{ij} the impulse symbol, this projector onto n_i can be expressed as $P_{ij} = \delta_{ij} - n_i n_j$. For more details about these conditions, one can refer to [79].

2.3.4 Boundary conditions

On the boundary of the domain Ω_1^f, the effect of the acoustical source is described as a boundary pressure $p_0(t)$. Thus, the boundary conditions read

$$\begin{cases} p_1 = p_0(t) & \text{in} \quad x_1 = x_s, \\ p_2 \to 0 & \text{as} \quad x_1 \to +\infty, \end{cases} \tag{2.13}$$

where x_s is the abscissa of the source.

2.4 Semi-analytical 1-D solution of plane waves in Laplace domain

In this section, a closed-form solution of the 1D formulation problem will be presented using a method based on the Laplace transform.

2.4.1 One-dimensional problem in time-domain

We start by considering that the only non-vanishing components of all displacement fields are those parallel to the unit vector $\underline{e}_1$, and that all fields are function only of the coordinate x_1 (*i.e.* all the derivatives are vanishing, with the exception of $(\cdot)_{,i} = \partial(\cdot)/\partial x_1$). For simplification purpose, we will omit the indexes of the first component of the vectors (or matrices) in 3D equations, *i.e.*: $u_1 \mapsto u$, $w_1 \mapsto w$, $\sigma_{11} \mapsto \sigma$, $\epsilon_{11} \mapsto \epsilon$, $\tau_{111} \mapsto \tau$, $C_{1111} \mapsto C$, $k_{11} \mapsto k$, $\alpha_{11} \mapsto \alpha$, $b_{11} \mapsto b$. In the fluid domains, the equation (2.1) may be simplified into the following form

$$\ddot{p}_1 - c_f^2 p_{1,11} = 0 \qquad \text{for} \qquad x_s \leq x_1 \leq 0, \tag{2.14a}$$

$$\ddot{p}_2 - c_f^2 p_{2,11} = 0 \qquad \text{for} \qquad x_1 \geq 0. \tag{2.14b}$$

In the solid domain ($0 \leq x_1 \leq L$), the 1D momentum balance equations (2.2)-(2.3) become

$$\sigma_{,1} - \alpha p_{,1} - \tau_{,11} = \rho \ddot{u} + \rho_f \ddot{w} - \eta \ddot{u}_{,11}, \tag{2.15a}$$

$$-p_{,1} = \rho_f \ddot{u} + k^{-1} \dot{w} + b \ddot{w}, \tag{2.15b}$$

and the constitutive equations read

$$\sigma = C u_{,1} - \alpha p, \tag{2.16a}$$

$$\tau = \ell^2 C u_{,1}, \tag{2.16b}$$

$$p = -M(\alpha u_{,1} + w_{,1}). \tag{2.16c}$$

Finally, for the continuity conditions at the interface between the porous material and the i^{th} fluid domain, we have the following simplification

$$p = p_i, \tag{2.17a}$$

$$\rho(\ddot{w} + \ddot{u}) = -p_{i,1}, \tag{2.17b}$$

$$\sigma - \tau_{,11} + \eta \ddot{u}_{,1} = -p_i, \tag{2.17c}$$

$$\tau = 0. \tag{2.17d}$$

2.4.2 One-dimensional problem in Laplace domain

In order to solve above system of PDEs, which depends on both time (t) and space (x), we will use the Laplace transform technique. First, the Laplace transform with respect to time is applied. Then, in the Laplace domain, the solution of the transformed PDEs (with respect to x) is analytically derived by using the boundary conditions. Last, the time solution can be computed by using a numerical inverse Laplace transform.

As an example, the Laplace transform of a space-time field $f(x,t)$ is the function $\tilde{f}(x,s)$ and is a unilateral transform defined by

$$\tilde{f}(x,s) := \mathcal{L}[f(x,t)] = \int_0^{+\infty} f(x,t)e^{-st}\,\mathrm{d}t, \tag{2.18}$$

where s is the complex Laplace variable.

2.4.3 Solutions of pressures in Ω_1^f and Ω_2^f

In the i^{th} fluid, since initial conditions are vanishing, equations of motion in the Laplace domain read

$$s^2\tilde{p}_i - c^2\tilde{p}_{i,11} = 0. \tag{2.19}$$

Noting that $\tilde{p}_1(x_s,s) = \tilde{p}_0$, where $\tilde{p}_0$ is the Laplace transform of time-dependent pressure pulse function, the general solution of $\tilde{p}_1$ in Eq. (2.19) can be expressed as

$$\tilde{p}_1 = Q_1(e^{\xi x} - e_s^2 e^{-\xi x}) + \tilde{p}_0 e_s e^{-\xi x}, \tag{2.20}$$

where $\xi := \frac{s}{c}$, $e_s := e^{\xi x_s}$, Q_1 is a complex constant. Similarly, noting that $\tilde{p}_2 \to 0$ as $x \to +\infty$ the general solution of $\tilde{p}_2$ in Eq. (2.19) is

$$\tilde{p}_2 = Q_2 e^{-\xi(x-L)}, \tag{2.21}$$

where Q_2 is a complex constant and L represents the thickness of the bone specimen.

2.4.4 Solutions of waves in the porous layer $\Omega^b = [0, L]$

In the porous medium, the equations of motion in Laplace domain, for vanishing initial conditions, read

$$s^2(\rho - \beta\rho_f)\tilde{u} - (C + s^2\eta)\tilde{u}_{,11} + \ell^2 C\tilde{u}_{,1111} + (\alpha - \beta)\tilde{p}_{,1} = 0, \tag{2.22}$$

$$\frac{\tilde{p}}{M} - \frac{\beta}{s^2\rho_f}\tilde{p}_{,11} + (\alpha - \beta)\tilde{u}_{,1} = 0, \tag{2.23}$$

where $\beta = \rho_f ks/(1+bks)$. We used the constitutive equations that allow us to eliminate the filtration displacement $\tilde{w}$.
By looking for the general solutions of Eqs. (2.22) and (2.23), under the forms $\tilde{u} = Ue^{\lambda sx}$ and $\tilde{p} = Pe^{\lambda sx}$, respectively, where U, P and λ are constants to be determined, the system of Eqs. (2.22) and (2.23) may be rewritten in matrix form as

$$\underline{\underline{\mathrm{A}}} \begin{bmatrix} U \\ P \end{bmatrix} e^{\lambda sx} = \begin{bmatrix} 0 \\ 0 \end{bmatrix},$$

where

$$\underline{\underline{\mathrm{A}}} = \begin{bmatrix} (C+s^2\eta)\lambda^2 - Cs^2\lambda^4\ell^2 + (\beta\rho_f - \rho) & \frac{1}{s}(\beta-\alpha)\lambda \\ s(\alpha-\beta)\lambda & \frac{1}{M} - \frac{\beta\lambda^2}{\rho_f} \end{bmatrix}.$$

Non trivial solutions of this system impose that $\det(A) = 0$, where det denotes the determinant operator. That leads to the characteristic equation

$$\begin{aligned} \frac{C\ell^2\beta s^2}{\rho_f}\lambda^6 - &\left(\frac{C\ell^2 s^2}{M} + \frac{(C+s^2\eta)\beta}{\rho_f}\right)\lambda^4 + \\ &+ \left(\frac{C+s^2\eta}{M} + (\alpha-\beta)^2 - \frac{(\rho-\beta\rho_f)\beta}{\rho_f}\right)\lambda^2 + \frac{\rho-\beta\rho_f}{M} = 0. \end{aligned} \tag{2.24}$$

It is important to remark that, differently from the classic Biot poroelastic wave problem, the characteristic equation is now bicubic with respect to λ. Hence, Eq. (2.24) has six conjugate roots λ_i (for $i = 1, \ldots, 6$).

Thus, the general solutions for $\tilde{u}(x)$ and $\tilde{p}(x)$ read, respectively,

$$\tilde{u}(x) = \sum_{i=1}^{6} U_i e^{\lambda_i sx} \quad \text{and} \quad \tilde{p}(x) = \sum_{i=1}^{6} P_i e^{\lambda_i sx}. \tag{2.25}$$

By substituting the general solutions of $\tilde{p}$ and $\tilde{u}$ into Eq. (2.22), one may rewrite $\tilde{p}(x)$ by $\tilde{p}(x) = \sum_{i=1}^{6} \gamma_i U_i e^{\lambda_i sx}$, where the parameters γ_i are defined as

$$\gamma_i = \frac{((C+s^2\eta)\lambda_i^2 - C\ell^2 s^2\lambda_i^4 - (\rho-\beta\rho_f))s}{(\alpha-\beta)\lambda_i}.$$

2.4.5 Closed-form solutions for $\tilde{p_1}$ and $\tilde{p_2}$ in the Laplace domain

We are eventually left within 8 unknown coefficients (Q_1, Q_2, and U_i for $i = 1, \ldots, 6$) that shall be determined from the 8 interface conditions at two

fluid-porous interfaces (see Eqs. (2.17a)-(2.17d)).
We first use the two conditions $\tilde{p}(0,s)=\tilde{p}_1(0,s)$ and $\tilde{p}(L,s)=\tilde{p}_2(L,s)$ to express Q_1 and Q_2 in terms of U_i

$$Q_1=\frac{\sum_{i=1}^{6}\gamma_i U_i-\tilde{p}_0 e_s}{1-e_s^2},\quad Q_2=\sum_{i=1}^{6}\gamma_i U_i. \tag{2.26}$$

The remaining interface conditions (2.17b), (2.17c) and (2.17d) provide six equations to be solved for the unknowns U_i, after eliminating coefficients Q_1 and Q_2,

$$\begin{aligned}
&\sum_{i=1}^{6} A_i U_i = 0, \quad &&\sum_{i=1}^{6} A_i e_i U_i = 0,\\
&\sum_{i=1}^{6} B_i U_i = 0, \quad &&\sum_{i=1}^{6} B_i e_i U_i = 0,\\
&\sum_{i=1}^{6} C_i U_i = \tilde{f}, \quad &&\sum_{i=1}^{6} D_i e_i U_i = 0,
\end{aligned} \tag{2.27}$$

in which the coefficients are given by

$$A_i=(1-\ell^2 s^2)\lambda_i s C+(1-\alpha)\gamma_i+\eta\lambda_i s^3,\qquad B_i=\ell^2 s^2\lambda_i^2 C,\qquad C_i=\bar{\gamma}_i\xi+G_i,$$

$$D_i=-\gamma_i\xi+G_i,\qquad e_i=e^{\lambda_i s L},\qquad \tilde{f}=\frac{2\tilde{p}_0\xi e_s}{1-e_s^2},$$

where

$$\bar{\gamma}_i=\frac{1+e_s^2}{1-e_s^2}\gamma_i,\quad G_i=\rho_f s^2\left(1-\beta(1+\frac{\lambda_i\gamma_i}{s\rho_f})\right).$$

Using a matrix representation, these equations may be rewritten as

$$\begin{bmatrix}
A_1 & A_2 & A_3 & A_4 & A_5 & A_6\\
\frac{A_1}{e_1} & \frac{A_2}{e_2} & \frac{A_3}{e_3} & \frac{A_4}{e_4} & \frac{A_5}{e_5} & \frac{A_6}{e_6}\\
B_1 & B_2 & B_3 & B_4 & B_5 & B_6\\
\frac{B_1}{e_1} & \frac{B_2}{e_2} & \frac{B_3}{e_3} & \frac{B_4}{e_4} & \frac{B_5}{e_5} & \frac{B_6}{e_6}\\
C_1 & C_2 & C_3 & C_4 & C_5 & C_6\\
\frac{D_1}{e_1} & \frac{D_2}{e_2} & \frac{D_3}{e_3} & \frac{D_4}{e_4} & \frac{D_5}{e_5} & \frac{D_6}{e_6}
\end{bmatrix}
\begin{pmatrix}U_1\\U_2\\U_3\\U_4\\U_5\\U_6\end{pmatrix}
=\begin{pmatrix}0\\0\\0\\0\\\tilde{f}\\0\end{pmatrix}. \tag{2.28}$$

2.4.6 Computation of solution in the time domain

In order to obtain the solutions of p_1 and p_2 (from Eqs. (2.20)-(2.21)) in both fluid domains as well as the solutions of $p(x,t)$ and $u(x,t)$ (see Eq. (2.25)), we have to come back to the time domain. Thus, an inverse Laplace transform is required. For this study, the Laplace transform was performed by using the convolution quadrature method (CQM) [110].

2.5 Finite element simulation

In this section, we compute the weak form of the problem, with the aim of numerically evaluate the time domain solution using the finite elements method. The results will be then compared with those obtained using the closed-form solution.

2.5.1 Variational equation in the fluid domains

Upon integrating the Eq. (2.14a) by parts against the function $\bar{p}_1$ over the fluid domain Ω_1^f, we obtain variational equation of fluid pressure p_1

$$\int_{x_s}^{0} \bar{p}_1 \left(\frac{1}{c_0^2}\,\ddot{p}_1\right) \mathrm{d}x + \int_{x_s}^{0} (\bar{p}_{1,1})(p_{1,1})\mathrm{d}x + \left[\bar{p}_1(p_{1,1})\right]_{x_s}^{0} = 0, \tag{2.29}$$

where $\bar{p}_1$ is the test function.
By using the boundary condition, Eq. (2.17b), and the admissible boundary condition of the test function $\bar{p}_1(x_s) = 0$, we obtain

$$\int_{x_s}^{0} \bar{p}_1 \left(\frac{1}{c_0^2}\,\ddot{p}_1\right) \mathrm{d}x + \int_{x_s}^{0} (\bar{p}_{1,1})(p_{,1})\mathrm{d}x + \bar{p}_1(0)\left[\rho_0(\ddot{w}(0) + \ddot{u}(0)\right] = 0. \tag{2.30}$$

For finite element simulation in the half-space Ω_2^f, we define a finite domain $x_1 \in [L, L+L_2]$, where L_2 is a length given. Then the variational equation for the fluid pressure p_2 in the fluid domain Ω_2^f may be derived as

$$\int_{L}^{L_2} \bar{p}_2 \left(\frac{1}{c_0^2}\,\ddot{p}_2\right) \mathrm{d}x \int_{L}^{L_2} (\bar{p}_{2,1})(p_{2,1})\mathrm{d}x - \bar{p}_2(L)\left[\rho_0(\ddot{u}(L) + \ddot{w}(L)\right] = 0, \tag{2.31}$$

where $\bar{p}_2$ is the test function.

2.5.2 Variational equation in the porous domain

By introducing two test functions $\bar{u}$ and $\bar{w}$ for u and w, respectively, the variational equations in Ω^b read

$$\begin{aligned}
&\int\limits_0^L \bar{u}\left(\rho\ddot{u}+\rho_f\ddot{w}\right)\mathrm{d}x-\int_0^L(\bar{w}_{,1})p\mathrm{d}x+\int_0^L(\bar{u}_{,1})\left(\sigma-\tau_{,1}+\eta\ddot{u}_{,1}\right)\mathrm{d}x\\
&\qquad\qquad-\left[\bar{u}\left(\sigma-\tau_{,1}+\eta=\ddot{u}_{,1}\right)\right]_0^L=0,\\
&\int\limits_0^L \bar{w}\left(\rho_f\ddot{u}+k^{-1}\dot{w}+b\ddot{w}\right)\mathrm{d}x-\int_0^L(\bar{w}_{,1})p\mathrm{d}x+\left[(\bar{w})p\right]_0^L=0.
\end{aligned}\tag{2.32}$$

The term concerning τ may be further developed as

$$-\int\limits_0^L(\bar{u}_{,1})\tau_{,1}\mathrm{d}x=\int\limits_0^L(\bar{u}_{,11})\ell^2C(u_{,11})\mathrm{d}x-\left[(\bar{u}_{,1})\tau\right]_0^L.\tag{2.33}$$

By taking into account the continuity conditions at two interfaces $x=0$ and $x=L$, we obtain

$$\begin{aligned}
&\int_0^L \bar{u}\left(\rho\ddot{u}+\rho_f\ddot{w}\right)\mathrm{d}x+\int_0^L(\bar{u}_{,1})\left(C+\alpha^2M\right)u_{1,1}\mathrm{d}x+\int_0^L(\bar{u}_{,1})\alpha Mw_{,1}\mathrm{d}x\\
&\qquad+\int_0^L(\bar{u}_{,1})\left(\eta\ddot{u}_{,1}\right)\mathrm{d}x+\int_0^L(\bar{u}_{,11})\ell^2Cu_{1,11}\mathrm{d}x\\
&\qquad+\bar{u}(L)p_2(L)-\bar{u}(0)p_1(0)=0,\\
&\int_0^L \bar{w}\left(\rho_f\ddot{u}+k^{-1}\dot{w}+b\ddot{w}\right)\mathrm{d}x+\int_0^L(\bar{w}_{,1})\alpha Mu_{,1}\mathrm{d}x+\int_0^L(\bar{w}_{,1})Mw_{,1}\mathrm{d}x\\
&\qquad+\bar{w}(L)p_2(L)-\bar{w}(0)p_1(0)=0.
\end{aligned}$$

2.6 Numerical results

This section is devoted to the presentation of some numerical results. In the first part, we describe the parameters used in the numerical tests, and their effect on phase velocity and attenuation. In the second part, we study the transient propagation of a plane wave. In order to check the semi-analytic scheme obtained *via* the Laplace transform and the convolution quadrature method, we illustrate the efficacy of the numerical scheme by determining the solution for different parameters, crosschecking the prediction with finite element solutions.

M (Pa)	α ($-$)	C_{11} (Pa)	k^{-1} (Pa$\cdot$ s/m)	b (kg/m^3)	f_0 (MHz)	P_0 (Pa)
2.735×10^9	0.95584	1.5783×10^9	2.221×10^7	1.328×10^3	1	1

Table 2.1 – Relevant coefficients considered in the present work.

2.6.1 Parameters for the computations

The poroelastic specimen is immersed in water, the physical characteristics of which are given by the bulk modulus $K_f = 2.5$ GPa and the mass density $\rho_f = 1000$ kg/m^3. We consider the physical parameters of a typical human cancellous bone, *i.e.* the porosity $\phi = 0.8$, the mass density of the solid phase $\rho_s = 1960$ kg/m^3, the Young's modulus $E_s = 20$ GPa and the Poisson's ratio $\nu = 0.30$ were chosen [79].

The thickness of the bone specimen is $L = 0.01$ m. The distance between the source and the bone specimen boundary Γ_1^{bf} is 0.02 m. In order to record the radio-frequency signals of the reflected and transmitted waves, in the fluid domains Ω_1^f and Ω_2^f we placed two receivers r_1 and r_3, respectively: receiver r_1 is placed on $\underset{\sim}{e}_1$-axis at the position $x = -0.002$ m (*i.e.* at a distance of 0.002 m from the boundary Γ_1^{bf} of the bone specimen) to sample the pressure p_1, while receiver r_3 is placed on $\underset{\sim}{e}_1$-axis at $x = 0.012$ m (*i.e.* at a distance of 0.002 m from the boundary Γ_2^{bf} of the bone specimen) to sample the pressure p_2. Since we are also interested in analyzing the pressure field p_s in the specimen, we placed a receiver r_2 in the middle of the poroelastic layer, at $x_1 = 0.005$ m.

The pressure source in Ω_1^f has the following form

$$p_0(t) = P_0 e^{-4(f_0 t - 1)^2} \sin(2\pi f_0 t),$$

where P_0 is a constant and f_0 is the central frequency.

The other parameters used in this study are given in Table 2.1. For what concerns the properties of the poroelastic layer, we recall here that the wave propagation is parallel to the main trabecular alignment of cancellous bone.

2.6.2 Validation of the closed form solution using the finite element method

With the aim of checking the analytic results, we provide in this section a comparison between the pressure computed at the receivers position computed using the closed-form and finite element method. The finite element code has been developed starting from the weak formulation presented in Sec. 2.5 and implemented

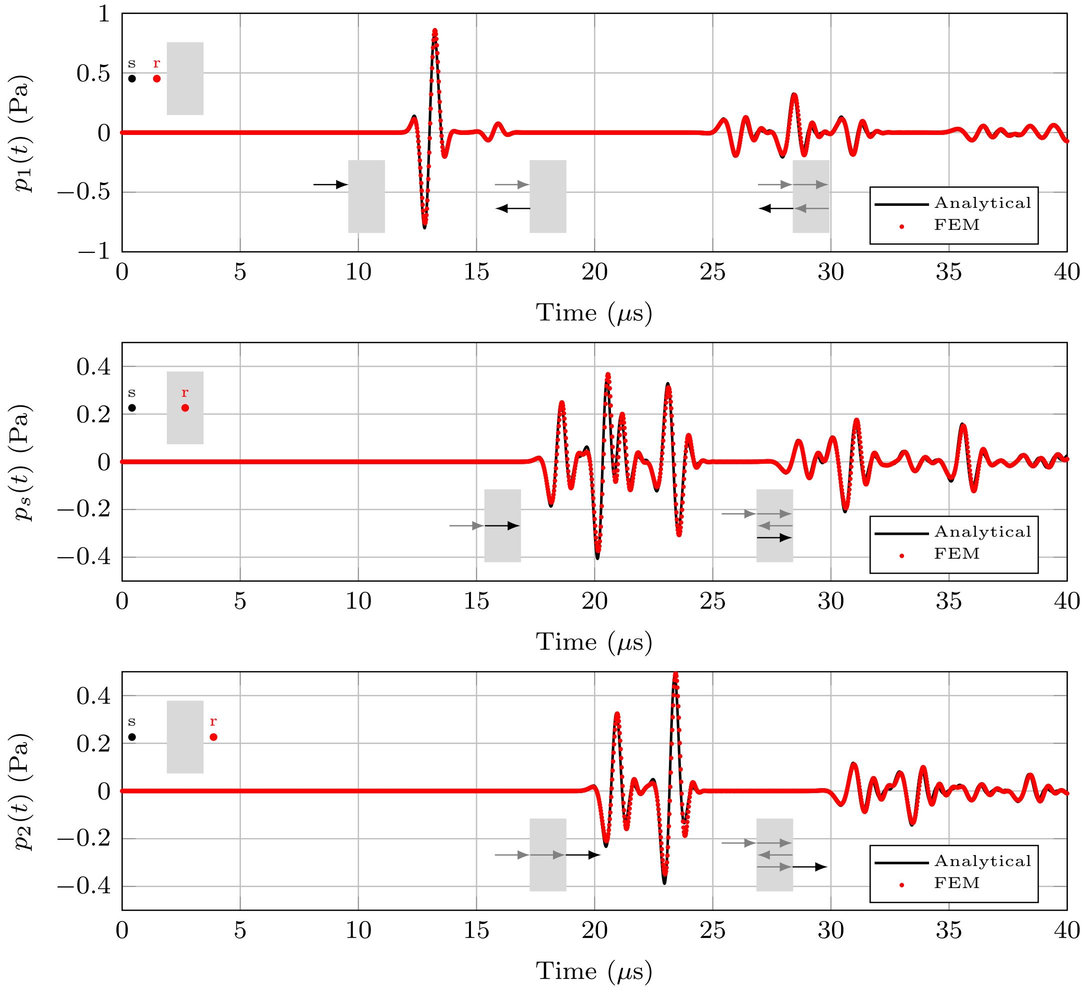

Figure 2.2 – Signal amplitudes for $\ell = 10^{-8}$ m and $\eta = 10^{-6}$ kg/m: $p_1(t)$ (at the top), $p_s(t)$ (in the middle) and $p_2(t)$ (at the bottom).

by means of the commercial software COMSOL Multiphysics (Stockholm, Sweden). We used the parameters listed in Tab. 2.1. The second gradient parameters have been chosen in the following way to $\ell = 10^{-8}$ m and $\eta = 10^{-6}$ kg/m. A more detailed discussion of the influence of these parameters on phase velocity and attenuation will be the object of the next section. The pressure fields computed with both methods are presented in Fig. 2.2. In each plot, in the upper left corner, we introduced a scheme illustrating where the sources and receivers are located. Moreover, in the lower part of the plot, each wave is identified by means of the corresponding sketch that indicates if it is an incident, reflected or transmitted wave. As it can be seen from the plots, the solutions are superposed,

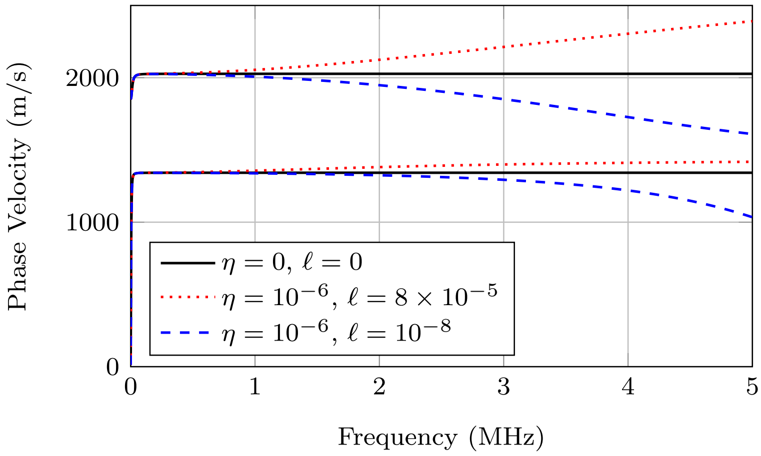

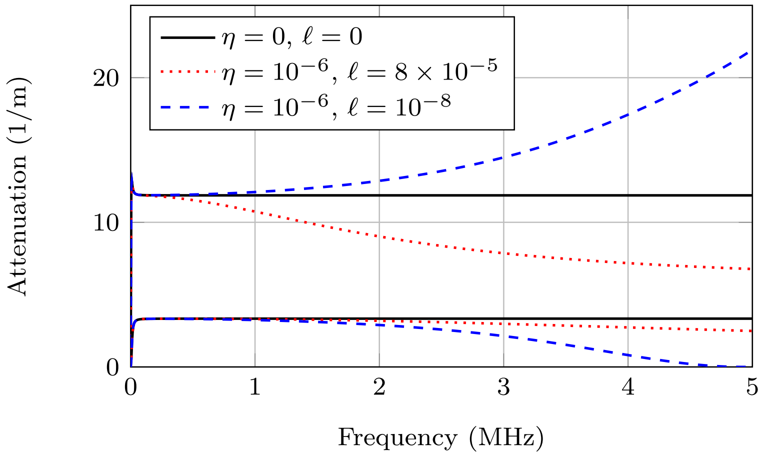

Figure 2.3 – (Colors online) Dispersion curves of phase velocities (on the left) and attenuation (on the right) for the following cases: $\ell = 0$ m and $\eta = 0$ kg/m (continuous black line), $\ell = 10^{-7}$ m and $\eta = 10^{-6}$ kg/m (dashed blue line), $\ell = 10^{-8}$ m and $\eta = 10^{-6}$ kg/m (dotted red line).

meaning that the closed-form solution is a reliable method for computing the response pressure. Since the objective of this section is to check and validate the two numeric approaches, we leave all considerations and interpretation of the results to Sec. 2.6.4.

2.6.3 About phase velocity and attenuation

The dispersion analysis allows to describe the effect that a wave traveling within a medium has on the properties. In particular, the dispersion relations relate wavelength/wavenumber to the frequency. Now, before proceeding with the analysis of phase velocity and attenuation, a quick recall of the quantities involved may be useful.

Phase velocity can be expressed in function of the roots of λ_i of Eq. (2.24) as

$$v^p(\omega) = \mathrm{Re}\left\{\frac{1}{\lambda(i\omega)}\right\},$$

where Re denotes the real part of the complex number.

The attenuation can be computed as

$$a^p(\omega) = -\mathrm{Im}\left\{\omega\lambda(i\omega)\right\},$$

where Im denotes the imaginary part of the complex number.

In this section, we will focus only on the roots corresponding to propagative waves. As it can be seen in Fig. 2.3, both phase velocity and attenuation are dispersive, when the higher gradient constitutive parameters (the characteristic length ℓ and the micro inertia η) are both different from zero. The non dispersive case, *i.e.* when the aforementioned coefficients are set to zero, will be kept as a benchmark. Among all other possible parameters combinations, we chose to consider the following cases:

- **No dispersion**: phase velocities are constant, obtained for $\ell = 0$ m and $\eta = 0$ kg/m.

- **Normal dispersion**: phase velocities are decreasing when increasing the frequency, obtained for $\ell = 10^{-8}$ m and $\eta = 10^{-6}$ kg/m. This is also called *negative dispersion* in the literature.

- **Anomalous dispersion**: phase velocities are increasing when increasing the frequency, obtained for $\ell = 8 \times 10^{-5}$ m and $\eta = 10^{-6}$ kg/m. Also called *positive dispersion.*

All these kinds of dispersion can be observed experimentally (see *e.g.* [51, 126, 127]). In fact, accorting to an experimental study realizet by Haïat et al. [51], both positive and negative dispersion can be observed according to the characteristics of the bone sample considered. Therefore, in the work of Marutyan et al. [72], it is introduced the idea that negative dispersion can be associated to from the interference of two broadband ultrasonic pulses arriving on the receiver with a given time delay.

The curves of the attenuation coefficient for different values of the parameters are plotted in Fig. 2.3. First of all, it is interesting to remark that the trend with frequency is opposite with respect to the one observed for phase velocity. Indeed, in the case of normal dispersion, the attenuation is increasing with frequency. An opposite behavior can be observed for anomalous dispersion. It is important to remark that in both cases the attenuation introduced by means of the permeability alone has different effect with respect of the case when a gradient behavior is added. Again, there is experimental evidence of both behaviors in the literature [54, 93, 125]. Thus, when considering the effects due to the microstructure, the dispersion analysis shows a strong dependance on the ultrasound frequency.

2.6.4 Plane wave propagation, closed-form solution

In this section, we discuss the results obtained by means of the semi-analytic method, based on the Laplace technique, for the closed-form solution. The plots are presented in Fig. 2.4, where the curves represent the pressure signals recorded by three receivers positioned as specified in section 2.6.1. Each subplot contains the results corresponding to the three different dispersion cases discussed in the previous section. We start the discussion from the top plot, that represents the evolution of the pressure field $p_1(t)$ as measured by the sensor r_1. This signal contains contributions (in order of arrival) from the incident wave, the wave reflected from the boundary Γ_1^{bf}, as sketched in the lower part of the graph. As it can be noticed, the second gradient parameters do not affect the wave reflected from the first boundary (*i.e.* Γ_1^{bf}), while they influence the other contributions. In the terms related to the reflection from the second boundary (*i.e.* Γ_2^{bf}) we can clearly distinguish the fast and slow waves, a classic result in Biot's theory. These two waves are considerably affected by the second gradient parameters, for both normal and anomalous dispersion. In particular, as the phase velocity and attenuation depend on frequency, both amplitude and time of arrival of signals are affected. These considerations are more evident when analyzing the signal recorded from the sensor positioned in the poroelastic domain (middle graph of Fig. 2.4). The last plot of Fig. 2.4 concerns the transmitted signal, as recorded from the receiver positioned in the second fluid. Here we can observe a clear separation between the fast and slow waves and we can notice that the effects of the second gradient parameters are more evident on the second contribution to the transmitted signal, as this part corresponds to multiple reflections inside the poroelastic sample. These results show that the second gradient contribution affects the time domain response of the specimen in a way that is compatible to what can be observed in experiments (see *e.g.* [63] for bone). Since the value of the micro inertia η can be related to the characteristic size of the microstructure, and since ℓ is proportional to a characteristic length of the microstructure (*e.g.* the transverse size of the

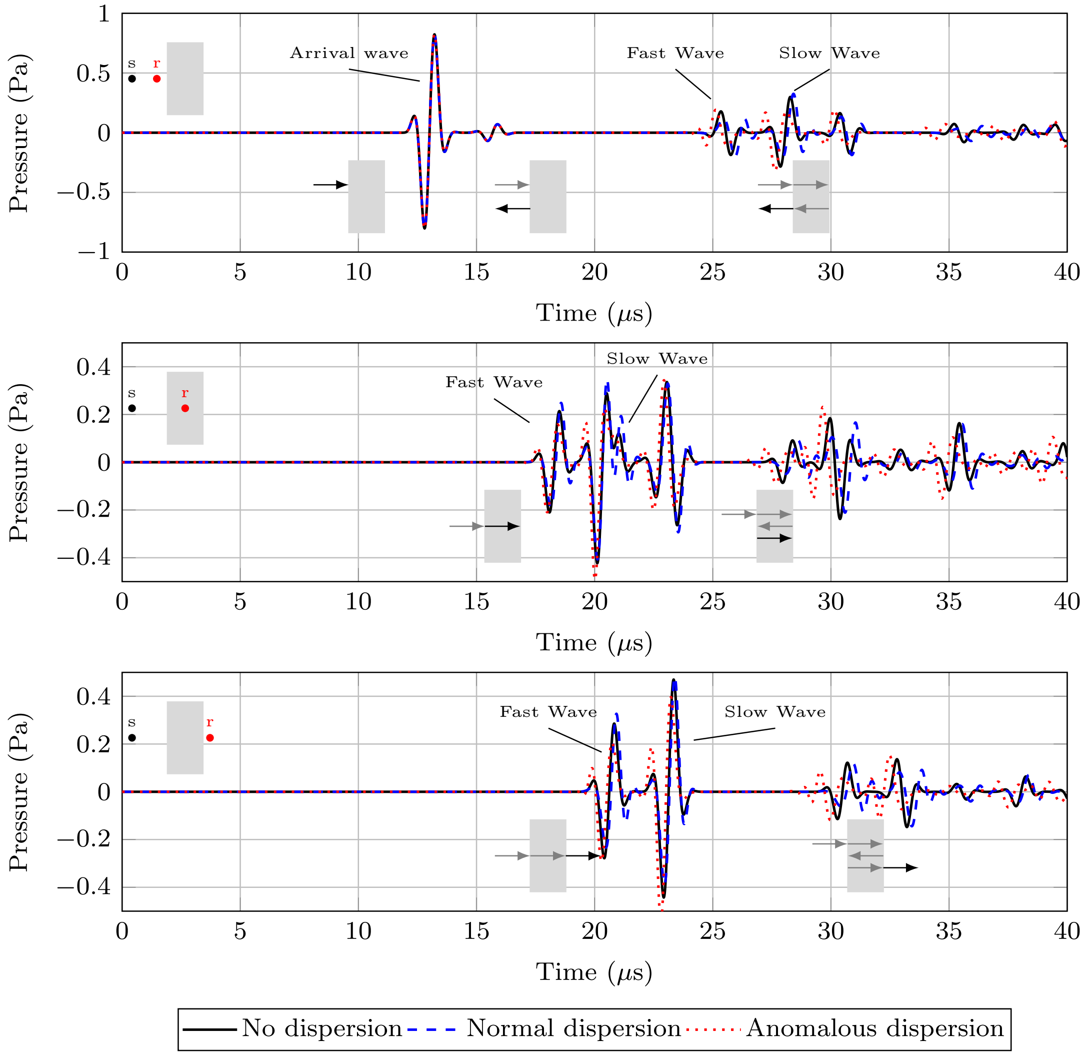

Figure 2.4 – In the upper left of each figure a scheme illustrating the position of the two probes (*e.g.* the source and the receiver) to the specimen is provided. Therefore, in the schematic representations on the bottom, the arrows stand for transmitted and reflected waves. The figures above show the three signal amplitudes: $p_1(t)$ (at the top), $p_s(t)$ (in the middle) and $p_2(t)$ (at the bottom). In each one, three particular cases are displayed: $\ell = 0$ m and $\eta = 0$ kg/m (continuous line), $l = 8 \times 10^{-5}$ m and $\eta = 10^{-6}$ kg/m (dashed line), $\ell = 10^{-8}$ m and $\eta = 10^{-6}$ kg/m (dotted line).

micro-structural elements like trabeculae in trabecular bone), some useful information about microstructures can be retrieved from the experimental analysis of these signals. It is important to note that for higher values of η, since the phase velocity decreases with frequency, a backscattering-like effect is observable.

2.7 Conclusion

In this work, we presented a closed-form time domain solution for the reflection/transmission problem involving a microstructured poroelastic solid.

The main results presented in this paper are the following:

- The analytical closed-form solution of the reflection/transmission problem for a second gradient poroelastic solid has been obtained.
- The closed-form solution is compared with the finite element solution. The solutions are in agreement, showing that both techniques are reliable.
- The phase velocity and attenuation curves are qualitatively in agreement with those observed in experiments for poroelastic specimens.
- Reflected and transmitted pressure fields are affected by the values of the microstructure second gradient parameters.

As a final remark about the interest of using the closed-form, we can cite the fact that the solution can be computed only for a given set of points of the domain, e.g. where the sensors are placed, in contrast with a finite element code, that computes the solution in every node of the mesh. This can lead to a considerable reduction in terms of computational costs.

The main perspectives are related to the validation of this model with an experimental campaign. We do expect that the introduction of the higher gradient coefficients can lead to a better agreement of the poroelastic model with respect to experimental data, especially in the case of high porosity. Experimental validation on bone or artificial bioresorbable materials (as discussed in [46]) is also envisaged.

Chapter 3

Effects of the microstructure and density profiles on wave propagation across an interface with material properties

---

The work presented in this chapter is issued fro the following publication:

> I. Scala, G. Rosi, L. Placidi, V.-H. Nguyen, and S. Naili. Wave propagation across an interphase with material properties. *Continuum Mechanics and Thermodynamics*, 1-16, 2019.

Abstract

The characterization of the interphase condition between two materials is current in mechanics. In general, its modeling is achieved by considering an interface with only purely elastic properties. In this chapter, following previous works, also inertial interface properties are taken into account. For sufficiently low frequency regime, we investigate two density profiles (affine and quadratic), for the interphase. Moreover, the interface and the interphase are placed between two solids with different characteristics. The first one is non-dispersive, while for the second one three cases are considered: a) solid without microstructure, *i.e.* a Cauchy continuum, b) solid with microstructure characterized by normal dispersion, *i.e.* a second gradient continuum, and c) by anomalous dispersion. The reflection coefficients are plotted for each case. These results are evaluated with respect to a benchmark finite elements simulation of the finite heterogeneous interphase, and the error is discussed. It is shown that the effects of microstructure can be appreciated at higher frequencies and that the proposed model results to be accurate.

Keywords: density profiles, interface, interphase, reflection coefficient, second gradient, wave propagation.

3.1 Introduction

Wave propagation in heterogeneous materials is a subject of interest in mechanics since the pioneering work of Mindlin in 1964 [75] or even, as remarked in [33], 120 years before in the published papers of Piola, see also [12, 31, 36, 42]. Once a plane wave in a half-space heterogeneous material interacts with another half-space, a crucial importance is assigned to the transition interphase between the two phases [13, 90, 91, 96]. Actually, in this chapter, an interphase with a finite thickness and its own properties (which are not the same of those of the two semi-spaces) will be considered.

Heterogeneous and homogeneous materials and interphases generally behaves unelastically [1, 15, 76]. However, in the literature, models that include only their elastic properties have been largely investigated [10, 11, 48, 50, 65, 66, 67, 94].

For instance, Jeannin et al. [60] modeled the interface surrounding rigid inclusions in sandstone as a two-dimensional geometrical model of a thin layer; or even, Chaboche et al. [24] modeled the interphase non-linear behavior by continuum elements, and then replaced the interphase elements with interface elements with null thickness. Moreover, when a transition between two materials, among which at least one is heterogeneous, is present, this is usually not an abrupt jump of properties but has rather the form of an interphase. Besides, the importance of considering not only elastic but also inertial properties has been considered in the literature [14, 21, 90].

Concerning the heterogenous microstructured materials [60], it is well known that materials with microscopic heterogeneous features exhibit frequency dependent properties, among others phase velocity and directivity [35, 84, 132]. Once the phenomenological observation, both in simulations and in experiments, is well established, modeling the dynamic behavior of these materials is not trivial. The reason is that both as simulations and experiments involve the geometrical complexity of the interphase. Indeed, predicting how the aforementioned properties change when modifying the heterogeneity or the constituents of the material is an open problem. To this end, the formulation of a continuum equivalent problem has been seen as a possible answer [23, 92]. However, the classic theory of elasticity is based on fields that are averaged on a given representative volume. Thus, when the perturbation has a size that is comparable with some geometrical features of the microstructure, the accuracy of the model decreases considerably. In the case of elastic waves, this is related to the wavelength being comparable to one of these characteristic sizes [19, 55]. These sizes could be related to the radius of pores, inclusions or the cross section of ligaments.

In this framework, the main challenge comes from the choice of the theory to be used. In this work we consider two half-infinite spaces that are separated by a thick interphase. One of the half-space is supposed to be filled by a homogeneous isotropic material, modeled with a standard Cauchy elastic continuum, the other is supposed to be heterogeneous and modeled with a non-standard second gradient elastic continuum. An elastic pressure wave with normal incidence travels within the first half-space and interacts with the interphase. Reflection and transmission conditions are studied as well as their coupling effects with the second half-space. In other words, this work aims to investigate the effects of a second gradient model on the reflection properties of the interphase.

Following the results presented in [101], of which this work represents a continuation, we use two models for the interphase, corresponding to two different approaches. In the first one, we model the interphase with a surface (interface model) with no thickness and specific surface properties. In particular, we give to such a surface inertial and elastic properties described, respectively, by kinetic and internal energies. The kinetic energy is assumed to depend to an average mass density and to an interaction parameter, γ_b, discussed in [90]. The internal energy is assumed to be of elastic nature, the rigidity of which is identified by a simple traction test. In the second model, the interphase is considered a three-dimensional classic functionally dependent non polar elastic body with finite thickness, with an harmonic evolution in time and a non trivial evolution in space (interphase model).

The evolution in space of the interphase is evaluated with a finite element code. We have numerically studied both models.

In the numerical case studies, the implant-bone interphase problem has been considered. Actually, because of the remodeling effects, the properties of the interphase evolve with time [27, 44, 45, 47, 64]. Furthermore, in this framework, the interphase surrounding the implant plays a key-role for the implant stability [53].

This chapter is organized as follows. After this introduction, Sections 3.2.1 and 3.2 are devoted to the presentation of the two approaches described before, each one with its geometrical configuration, equations of motion and boundary conditions. After an uni-axial simplification (Section 3.3), in Section 3.4 the case studies are introduced and the correspondent simulation results are shown. Finally, Section 3.5 is devoted to the discussion and general conclusion on the results of this work. Also some future developments are proposed.

3.2 Governing equations and boundary conditions

3.2.1 Statement of the problem

Let $\boldsymbol{R}(O;\boldsymbol{e}_1,\boldsymbol{e}_2,\mathbf{e}_3)$ be the reference Cartesian frame where O is the origin and $(\boldsymbol{e}_1,\boldsymbol{e}_2,\mathbf{e}_3)$ an orthonormal basis for the space. If we consider a point M in $\boldsymbol{R}$, its coordinates are specified by (x_1,x_2,x_3) and the time by t. In the present work, two geometrical configurations are considered (see Fig. 3.1). In the first case, as shown in Fig. 3.1a, the geometrical configuration presents a layer of thickness h, named Ω^I, located between two half-spaces, denoted Ω^- and Ω^+. The interphase layer Ω^I being an heterogeneous isotropic Cauchy continuum. In the second case, as illustrated in Fig. 3.1b, the finite interphase is replaced by a zero thickness layer, by an interface. Moreover, the two half-spaces are as follows: the domain Ω^- is a classic homogeneous isotropic Cauchy continuum; the domain Ω^+ is a homogeneous, isotropic second gradient continuum (which would then take into account the effects of the microstructure).

It is worth to be noted that these configurations could represent a bone-implant interface, where Ω^- is the titanium implant, Ω^+ the microstructured bone and Ω^I the newly formed bone around the implant. In fact, also in this case the interphase characterization needs parameters evolving with time (due to the remodelling effects [27]).

In this section, the equations of motion in the domains of interest will be presented. It is important to keep in mind that, in what follows, every variable is a function of both spatial coordinates and time, and that every material parameter is constant unless differently specified (as it will be for the interphase Ω^I). Moreover,

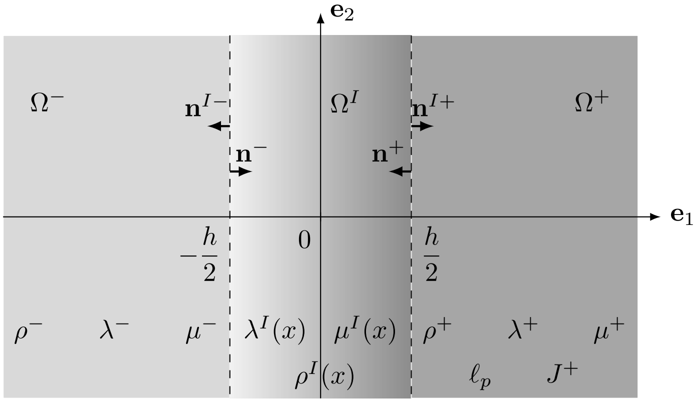

(a) Finite interphase

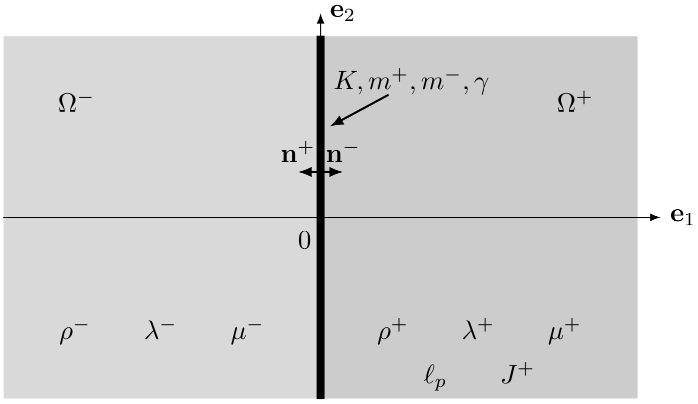

(b) Interface

Figure 3.1 – Geometrical configurations.

the superscripts $+$, $-$ and I will denote the belonging to the respective domains Ω^+, Ω^- and Ω^I. Furthermore, in this work, the Einstein notation, which implies summation over a set of indexed terms in a *formula*, has been assumed.

3.2.2 Equations of motion in the Cauchy domain Ω^-

Since we deal with a titanium implant, as already said in Sec. 3.2.1, the domain Ω^- is modeled as a classic homogeneous isotropic Cauchy continuum. So, starting from the variational principle, based on the first variation of the following action functional on the time interval $]0, T[$

$$\mathcal{A}^- = \int_{\Omega^- \times]0,T[} \left[T^- - U^- \right] dA, \tag{3.1}$$

the equations of motion will result, where dA represents the differential volume element.

Moreover, the kinetic and potential energy read, respectively,

$$T^- = \frac{1}{2}\rho^- \dot{u}_i^- \dot{u}_i^-, \qquad U^- = \frac{1}{2}\sigma_{ij}^- \varepsilon_{ij}^-, \tag{3.2}$$

where σ_{ij}^- represents the stress tensor, u_i^- the displacement vector, ρ^- the mass density and ε_{ij}^- denotes the infinitesimal strain tensor, defined as $\varepsilon_{ij}^- = \left(u_{i,j}^- + u_{j,i}^-\right)/2$. The superposed dot denotes a derivative with respect to time. Here, we will assume that volume forces are neglected. Consequently, the equations of motion read

$$\sigma_{ij,j}^- = \rho^- \ddot{u}_i^-, \qquad \text{for } i, j = 1, 2, 3. \tag{3.3}$$

Then, a constitutive law has to be included to the aforementioned equations, which, for an isotropic homogeneous material, read as

$$\sigma_{ij}^- = C_{ijkl}^- \varepsilon_{kl}^-, \tag{3.4}$$

where C_{ijkl} are the components of the fourth-order elastic tensor. Using (3.4) in (3.3), the equations of motion read

$$C_{ijkl}^- u_{k,lj}^- = \rho^- \ddot{u}_i^-. \tag{3.5}$$

3.2.3 Equations of motion in the second gradient domain Ω^+

As already mentioned in Sec. 3.2.1, the half-space Ω^+, in which the microstructured continuum is located, is modeled as an isotropic second gradient elastic continuum. For further details about this model, the reader may refer to Chapter 2 [75]. Again, the computation is based on the first variation of the action functional

$$\mathcal{A}^+ = \int_{\Omega^+ \times]0,T[} \left[T^+ - U^+\right] dA, \tag{3.6}$$

where the kinetic density reads as follows

$$T^+ = \frac{1}{2}\rho^+ \dot{u}_i^+ \dot{u}_i^+ + \frac{1}{2} J_{ijmn}^+ \dot{u}_{i,j}^+ \dot{u}_{m,n}^+, \tag{3.7}$$

where ρ^+ is the bulk mass density and J_{ijmn}^+ represent the components of the micro inertia fourth-order tensor. Therefore, the potential energy density is

$$U^+ = \frac{1}{2}\sigma_{ij}^+ \varepsilon_{ij}^+ + \frac{1}{2}\tau_{ijk}^+ \eta_{ijk}^+, \tag{3.8}$$

where we denote with $\eta^+_{ijk} = \varepsilon^+_{ij,k}$ the gradient of the strain tensor and with τ^+_{ijk} the hyperstress tensor.
As a result, the equation of motion of a second gradient medium reads

$$s^+_{ij,j} = \rho^+ \ddot{u}^+_i - J^+_{ijmn} \ddot{u}^+_{j,mn}, \qquad \text{for } i,j,m,n = 1,2,3, \tag{3.9}$$

where $s^+_{ij,j}$ are the components of the *effective* second-order symmetric stress tensor, which is defined as

$$s^+_{ij} = \sigma^+_{ij} - \tau^+_{ijk,k}. \tag{3.10}$$

The complete set of constitutive equations, in the generic case, would read

$$\begin{cases} \sigma^+_{ij} = C^+_{ijlm} \varepsilon^+_{lm} + M^+_{ijlmn} \eta^+_{lmn} \\ \tau^+_{ijk} = M^+_{lmijk} \varepsilon^+_{lm} + A^+_{ijklmn} \eta^+_{lmn} \end{cases}, \tag{3.11}$$

where C^+_{ijlm} are the components of the fourth-order elastic tensor, A^+_{ijklmn} those of the sixth-order hyperelastic tensor and M^+_{ijlmn} those of the fifth-order coupling tensor. But, when we consider a centro-symmetric material, and this is the case of the present chapter, the components of the coupling tensor M^+_{ijlmn} vanishes and the constitutive equations are simplified as follows

$$\begin{cases} \sigma^+_{ij} = C^+_{ijlm} \varepsilon^+_{lm} \\ \tau^+_{ijk} = A^+_{ijklmn} \eta^+_{lmn} \end{cases}. \tag{3.12}$$

Now, by using (3.12) in (3.9), we obtain the following equations of motion

$$C^+_{ijlm} u^+_{l,mj} - A^+_{ijklmn} u^+_{l,jkmn} = \rho^+ \ddot{u}^+_i - J^+_{ijmn} \ddot{u}^+_{j,mn}. \tag{3.13}$$

3.2.4 Interface models and boundary conditions

In this section, the two models will be discussed separately and their respectively boundary conditions derived.

3.2.4.1 The case of a finite interphase (occupying the domain Ω^I)

The interphase domain Ω^I is also modeled as a classic Cauchy continuum, but, since it is an inhomogeneous medium, the equations of motion differ from those one presented in Eq. (3.3) and thus read

$$\sigma^I_{ij,j}(\boldsymbol{x}, t) = \rho^I(x_1) \ddot{u}^I_i(\boldsymbol{x}, t), \qquad \text{for } i,j = 1,2,3, \tag{3.14}$$

where $\boldsymbol{x}$ is the position vector and $\rho^I(x_1)$ is the mass density, function of the coordinate x_1. Consequently, also the constitutive law here reads

$$\sigma^I_{ij}(\boldsymbol{x},t) = C^I_{ijkl}(x_1)\varepsilon^I_{kl}(\boldsymbol{x},t). \tag{3.15}$$

Thus, using (3.15) in (3.14), we obtain the following equations of motion

$$C^I_{ijkl}(x_1)\varepsilon^I_{kl}(\boldsymbol{x},t) = \rho^I(x_1)\ddot{u}^I_i(\boldsymbol{x},t). \tag{3.16}$$

At the interface between the domains Ω^- and Ω^I, we suppose the continuity of the displacement field, as well as the continuity of tractions

$$\text{at } x_1 = -\frac{h}{2}, \quad \forall t \quad : \begin{cases} t^-_i + t^I_i = 0 \\ u^-_i\left(-\frac{h}{2}, x_2, x_3, t\right) = u^I_i\left(-\frac{h}{2}, x_2, x_3, t\right) \end{cases} \quad \text{for } i,j = 1,2,3, \tag{3.17}$$

where vectors $\boldsymbol{t}$ are tractions, and are defined by

$$t^-_i = \sigma^-_{ij}\left(-\frac{h}{2}, x_2, x_3, t\right) n^-_j, \tag{3.18}$$

$$t^I_i = \sigma^I_{ij}\left(-\frac{h}{2}, x_2, x_3, t\right) n^{I+}_j, \tag{3.19}$$

where $\boldsymbol{n}^{\pm, I\pm}$ represent the normal unit vectors with respect to the interphase and the interface, as shown in Figs. 3.1a and 3.1b.

In the case of the interface between the interphase layer and the second gradient solid, the boundary conditions are more complex because it must be also considered what happens on the double force. However, since, as already said, the solid Ω^I is a standard Cauchy continuum, the boundary conditions can be simplified by considering the double force equal to zero.

Indeed, in second gradient elasticity, bulk equations are supplemented with the boundary conditions:

$$\begin{cases} t^+_i = (s^+_{ij} + J^+_{ijkl}\ddot{u}^+_{k,l})n^+_j - P^+_{ml}(P^+_{mj}\tau^+_{ijk}n^+_k)_{,l} \\ R^+_i = \tau^+_{ijk}n^+_j n^+_k \end{cases}, \tag{3.20}$$

where $\boldsymbol{R}$ is the hyper traction vector. The quantity $P^+_{ij} = \delta_{ij} - n^+_i n^+_j$ represents the projector onto the surface normal to n^+_i.

Thus, in our case, we have

$$\text{at } x_1 = \frac{h}{2}, \quad \forall t \quad : \begin{cases} t^I_i + t^+ = 0 \\ R^+_i = 0 \\ u^I_i\left(\frac{h}{2}, x_2, x_3, t\right) = u^+_i\left(\frac{h}{2}, x_2, x_3, t\right) \end{cases} \quad \text{for } i,j = 1,2,3. \tag{3.21}$$

3.2.4.2 The case of a surface with material properties

Here, the interphase is modeled by adding surface energy terms related to the energy balance.

We use the following surface energy densities

$$T_S = \frac{1}{2}\left[m^+_{ij}\dot{u}^+_i\dot{u}^+_j + m^-_{ij}\dot{u}^-_i\dot{u}^-_j + 2\gamma_{ij}\dot{u}^+_i\dot{u}^-_j\right], \tag{3.22}$$

where $m^{\pm}_{ij}$ represent the masses concentrated on both sides of the interface and γ_{ij} the components of a kinetic interaction tensor. The role of γ_{ij} is to couple velocities on $+$ and $-$ side of the surface. The potential energy has been instead chosen as

$$U_S = \frac{1}{2}K_{ij}\llbracket u_i\rrbracket\llbracket u_j\rrbracket, \tag{3.23}$$

where K_{ij} is a second-order surface rigidity tensor, which allows to model the interphase as a soft interface [10, 11], and $\llbracket u_i\rrbracket = u^+_i(0) - u^-_i(0)$ represents the jump of the displacement at the interface. To simplify the treatment, we will consider the following form for the involved tensors

$$K_{ij} = \begin{bmatrix} K_1 & 0 & 0 \\ 0 & K_2 & 0 \\ 0 & 0 & K_3 \end{bmatrix}, \qquad m^+_{ij} = m^+\delta_{ij}, \qquad m^-_{ij} = m^-\delta_{ij}, \qquad \gamma_{ij} = \gamma_b\delta_{ij}. \tag{3.24}$$

The action functional reads

$$\mathcal{A}_S = \int_{\partial\Omega\times(0,T)} \left[T_S - U_S\right]. \tag{3.25}$$

From the least action principle on the total action $\mathcal{A}^{tot} = \mathcal{A}^- + \mathcal{A}^+ + \mathcal{A}_S$, we obtain the same balance equations as in Secs. 3.2.2 and 3.2.3, with the following additional boundary conditions

$$\begin{aligned}\left(s^+_{ij} + J^+\ddot{u}^+_{i,j}\right)n^+_j - \left(\delta_{mj} - n^+_m n^+_j\right)\left(\delta_{ml} - n^+_m n^+_l\right)\left(\tau^+_{imk}n^+_k\right)_{,l} &= \\ = -K_{ij}\llbracket u_j\rrbracket - m^+_{ij}\ddot{u}^+_j - \gamma_{ij}\ddot{u}^-_j&,\end{aligned} \tag{3.26}$$

$$\sigma^-_{ij}n^-_j = +K_{ij}\llbracket u_j\rrbracket - m^-_{ij}\ddot{u}^-_j - \gamma_{ij}\ddot{u}^+_j, \tag{3.27}$$

$$\tau^-_{ijk}n^+_j n^+_k = 0. \tag{3.28}$$

Indeed, in Eqs. (3.26)-(3.27) we can see the classic elastic term proportional to the jump of the displacement, as well as the additional inertial and coupling terms.

Concerning the identification of the parameters, a proposition is recalled here, following [7]. First, we recall here the differences between the two models, as depicted in Figs. 3.1a and 3.1b. In the interphase model we deal with an inhomogeneous and linear three-dimensional elastic body with a kinetic energy per unit surface T_I and mass density $\rho^I(x_1)$, that is a function of the coordinate x_1. If the velocity field of the interface $\dot{u}_i^I$ is also a function only of the coordinate x_1, then we have that the kinetic energy density per unit surface is

$$T_I = \int_{-h/2}^{h/2} \rho^I(x_1)\dot{u}_i^I(x_1)\dot{u}_i^I(x_1)dx_1. \tag{3.29}$$

Therefore, in the second model an infinitesimally thin 2D elastic surface presents a kinetic energy per unit surface T_S that is unequivocally defined by the constants m^-, m^+ and γ_b. Thus, following the simplification proposed in Eqs. (3.24), we get

$$T_S = \frac{1}{2}m^- v_i^- v_i^- + \frac{1}{2}m^+ v_i^+ v_i^+ + \gamma_b v_i^+ v_i^-, \tag{3.30}$$

where v_i^- and v_i^+ are the velocity values, respectively, on the left- and on the right-hand side of the interphase.

In both models continuity of displacement, displacement gradient, force and double forces are assured by the proposed boundary conditions. As already done in [101], we observe that, for sufficiently low values of frequencies and in the first case, also the velocity field $\dot{u}^I$ is approximately an affine function of the coordinate x_1, *i.e.*

$$\dot{u}_i^I(x_1) = \frac{1}{2}\left(v_i^+ + v_i^-\right) + \frac{x_1}{h}\left(v_i^+ - v_i^-\right). \tag{3.31}$$

By insertion of (3.31) into (3.29), we have,

$$T_I = T_S = \frac{1}{2}m^+ v_i^+ v_i^+ + \frac{1}{2}m^- v_i^- v_i^- + \gamma_b v_i^+ v_i^-, \tag{3.32}$$

where

$$m^+ = \frac{M_0}{4} + \frac{M_1}{h} + \frac{M_2}{h^2}, \quad m^- = \frac{M_0}{4} - \frac{M_1}{h} + \frac{M_2}{h^2}, \quad \gamma_b = \frac{M_0}{4} + 2\frac{M_2}{h^2}. \tag{3.33}$$

In the last expression, we introduced the following definition

$$M_\alpha = \int_{-h/2}^{h/2} x_1^\alpha \rho^I(x_1)dx_1, \qquad \text{for} \qquad \alpha = 0, 1, 2. \tag{3.34}$$

It is important to remark that this identification is independent on the density profile, provided that the hypothesis (3.31) holds.

3.3 Pressure plane wave propagation

As detailed in [75], for an isotropic case, the constitutive tensors for the two halfspaces read

$$\begin{aligned}
C^{\pm}_{ijkl} &= \lambda^{\pm}\delta_{ij}\delta_{kl} + \mu^{\pm}\left(\delta_{ik}\delta_{jl} + \delta_{il}\delta_{jk}\right), && (3.35)\\
A^{\pm}_{ijklmn} &= a_1\left(\delta_{ij}\delta_{kl}\delta_{mn} + \delta_{ij}\delta_{km}\delta_{ln} + \delta_{ij}\delta_{kn}\delta_{lm} + \delta_{in}\delta_{jk}\delta_{lm}\right) + a_2\left(\delta_{ij}\delta_{kn}\delta_{lm}\right), \\
&\quad + a_3\left(\delta_{ik}\delta_{jl}\delta_{mn} + \delta_{ik}\delta_{jm}\delta_{ln} + \delta_{il}\delta_{jk}\delta_{mn} + \delta_{im}\delta_{jk}\delta_{ln}\right) + a_4\left(\delta_{il}\delta_{jm}\delta_{kn} + \delta_{im}\delta_{jl}\delta_{kn}\right), && (3.36)\\
&\quad + a_5\left(\delta_{il}\delta_{jn}\delta_{km} + \delta_{im}\delta_{jn}\delta_{kl} + \delta_{in}\delta_{jl}\delta_{km} + \delta_{in}\delta_{jm}\delta_{kl}\right), \\
J^{+}_{ijkl} &= J^{+}_1\delta_{ij}\delta_{kl} + J^{+}_2\delta_{ik}\delta_{jl} + J^{+}_3\delta_{il}\delta_{jk}, && (3.37)
\end{aligned}$$

where λ and μ are the classic Lamé coefficients. We consider a general displacement of the form

$$u^{\pm}(\boldsymbol{x},t) = \begin{pmatrix} u_1(x_1,t) \\ 0 \\ 0 \end{pmatrix}, \tag{3.38}$$

since the only non-vanishing derivative is with respect to x_1.
Therefore, we have

$$\begin{cases} (c_p^-)^2 u^-_{1,11} = \ddot{u}^-_1 \\ (c_p^+)^2(1-\ell^2\partial_{11})u^+_{1,11} = \ddot{u}^+_1 - \dfrac{1}{6}h_p^2\ddot{u}^+_{1,11} \end{cases}, \tag{3.39}$$

where

$$\ell^2 = \frac{4a_1 + a_2 + 4a_3 + 2a_4 + 4a_5}{\lambda^+}, \qquad h_p^2 = \frac{6}{\rho^+}(J_1^+ + J_2^+ + J_3^+), \qquad c_p^{\pm} = \sqrt{\frac{\lambda^+ + 2\mu^+}{\rho^+}}. \tag{3.40}$$

in which ℓ is a characteristic length. The quantities $c_p^{\pm}$ represent the phase velocities when ℓ and h_p are set to zero.

We consider here the case of a P-wave with normal incidence. Then, the wave solutions have the following form

$$u_1^- = \big(A_i\exp(ik_p^- x_1) + A_r\exp(-ik_p^- x_1)\big)\exp(-i\omega t), \tag{3.41}$$

$$u_1^+ = \big(A_t\exp(ik_p^+ x_1) + B_t\exp(-\alpha_p^+ x_1)\big)\exp(-i\omega t), \tag{3.42}$$

where ω represents the angular frequency and A_i, A_r, A_t and B_t are complex amplitudes. In addition, $k_p^{\pm}$ and α_p^+ are defined as follows

$$k_p^- = \frac{\omega}{c_p^-}, \tag{3.43}$$

$$k_p^+ = \sqrt{\frac{-(c_p^+)^2 + \frac{1}{6}h_p^2\omega^2 + \sqrt{4\ell^2(c_p^+)^2\omega^2 + \left((c_p^+)^2 - \frac{1}{6}h_p^2\omega^2\right)^2}}{2\ell^2(c_p^+)^2}}, \tag{3.44}$$

$$\alpha_p^+ = \sqrt{\frac{(c_p^+)^2 - \frac{1}{6}h_p^2\omega^2 + \sqrt{4\ell^2(c_p^+)^2\omega^2 + \left(-(c_p^+)^2 - \frac{1}{6}h_p^2\omega^2\right)^2}}{2\ell^2(c_p^+)^2}}. \tag{3.45}$$

3.3.1 Finite interphase

In the case of a finite interphase, we have the following harmonic solution

$$u_1^I = f(x)\exp(-i\omega t), \qquad u_2^I = u_3^I = 0. \tag{3.46}$$

Then, Eq. (3.16) becomes

$$c_{11,1}^I f_{,1} + c_p^I f_{,11} + \omega^2 \rho^I f = 0, \tag{3.47}$$

where we introduced the bulk modulus $c_{11}^I = \lambda^I + 2\mu^I$. The boundary conditions now read

$$\text{at } x = -\frac{h}{2} \Rightarrow \quad \begin{cases} c_{11}^- u_{1,1}^- = c_{11}^I u_{1,1}^I \\ u_1^- = u_1^I \end{cases}, \tag{3.48}$$

$$\text{at } x = \frac{h}{2} \Rightarrow \quad \begin{cases} c_{11}^I u_{1,1}^I = -c_{11}^+\left(u_{1,1}^+ - \ell^2 u_{1,111}^+\right) - \frac{1}{6}h_p^2 \ddot{u}_{1,1}^+ \\ u_1^- = u_1^I \end{cases}. \tag{3.49}$$

Therefore, the boundary value problem for the function $f(x_1)$ is obtained by using the wave solutions (Eqs. (3.41)-(3.46)) and by eliminating the variables A_t, A_r and B_t. Thus, it reads

$$\begin{cases} \left[c_{11}^I f_{,1}\right]_{,1} + \omega^2\rho^I f = 0 \\ c_{11}^I\left(-h/2\right) f_{,1}\left(-h/2\right) = -ic_{11}^- k_p^- f\left(-h/2\right) + i2c_{11}^- k_p^- A_i \exp\left(i\frac{h}{2}k_p^-\right) \\ c_{11}^I\left(h/2\right) f_{,1}\left(h/2\right) = \frac{\alpha_p k_p^+}{i\alpha + k_p^+}\left(c_{11}^+\left(1 - ik_p^+\alpha_p\ell^2\right) - \frac{1}{6}h_p^2\omega^2\right) f\left(h/2\right) \end{cases}, \tag{3.50}$$

where first there is an ordinary differential equation with respect to the coordinate x_1 and then two Neumann boundary conditions on the interfaces $x_1 = -h/2$ and $x_1 = h/2$, respectively.

Case	h_p (mm)	ℓ (mm)	**Description**
1	0	0	No dispersion
2	5.17	0.14	Normal dispersion
3	0.14	3.17	Anomalous dispersion

Table 3.1 – Dispersion cases considered with the respective values of the characteristic length ℓ and of the term related to the microinertia h_p.

3.3.2 Inertial interface

In the case of interface with material properties the boundary conditions read

$$\begin{cases} -c_{11}^{+}u_{1,1} + \ell^2 c_{11}^{+}u_{1,111} + \dfrac{1}{6}h_p^2\ddot{u}_{1,1} = -K_1[\![u_1]\!] - m^{+}\ddot{u}_1^{+} - \gamma_b\ddot{u}_1^{-}, \\ c_{11}^{-}u_{1,1} = K_1[\![u_1]\!] - m^{-}\ddot{u}_1^{-} - \gamma_b\ddot{u}_1^{+}, \\ u_{1,11} = 0. \end{cases} \tag{3.51}$$

3.4 Case studies and numerical examples

In this section we take into account several case studies, in order to explore the effective capabilities of the model. We will consider the following cases:

- Case 1: solid without microstructure;
- Case 2: solid with microstructure characterized by normal dispersion;
- Case 3: solid with microstructure characterized by anomalous dispersion.

This discrimination is useful for taking into account realistic configurations and to be able to investigate the effect of the microstructure. As shown in Tab. 3.1, the solid without microstructure corresponds to a non dispersive case, where the second gradient parameters (*i.e.* the characteristic length ℓ and the microinertia h_p) are set to zero. Then, with the addition of these parameters, and so by considering the microstructure, we distinguish a normal dispersion ($h_p > \ell$) and an anomalous dispersion ($\ell > h_p$).

The materials' parameters used for the numerical simulation are listed in Tab. 3.2.

ρ^- (kg/m^3)	E^- (GPa)	ν^-	ρ^+ (kg/m^3)	E^+ (MPa)	ν^+	h (mm)
4420	110	0.3	1280	96	0.3	7

Table 3.2 – Parameters used in the simulations.

Therefore, starting from Eq. (3.44), phase velocity has been computed as

$$c_p = \frac{\omega}{k_p^+}. \tag{3.52}$$

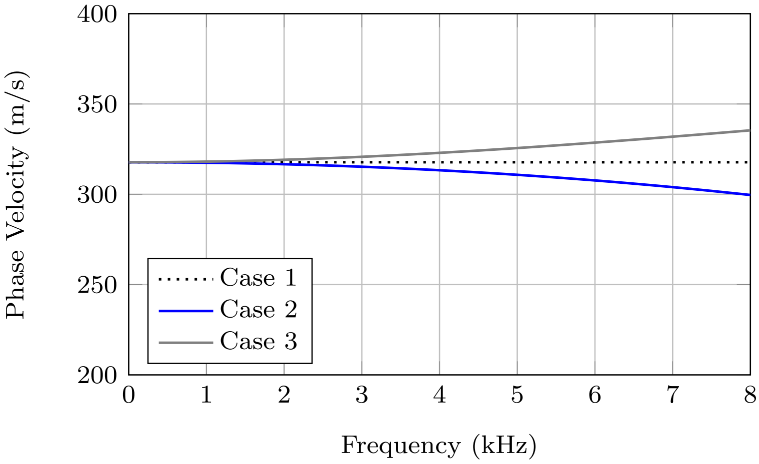

Figure 3.2 – Phase velocities for the different set of parameters.

Figure 3.2 shows the behavior of phase velocity with respect to frequency. In detail, it can be remarked that phase velocity is non dispersive when the gradient parameters are both equal to zero; it decreases with frequency for a normal dispersion and increases with frequency for an anomalous dispersion.
All aforementioned cases of dispersion can be found experimentally [52, 128].

3.4.1 Material properties of the interphase

For the other mechanical parameters we will use the following power law

$$E^I(x_1) = E^+ \left[\frac{\rho^I(x_1)}{\rho^+}\right]^{1.96}, \tag{3.53}$$

where $E^I(x_1)$ and E^+ are the Young's *moduli* in the interphase and in the positive half-space, respectively. This law is inspired to that used for bones in [27].

3.4.1.1 Affine distribution of density

Figure 3.3a shows the configuration, in which the density profile in the interphase is taken, and has the following form

$$\rho^I(x_1) = \frac{\rho^+(1-\xi)}{h}x_1 + \frac{\rho^+(1+\xi)}{2}, \tag{3.54}$$

that gives

$$m^- = \frac{M_0}{6}\frac{1+3\xi}{1+\xi}, \quad m^+ = \frac{M_0}{6}\frac{3+\xi}{1+\xi}, \quad \gamma = \frac{M_0}{6}. \tag{3.55}$$

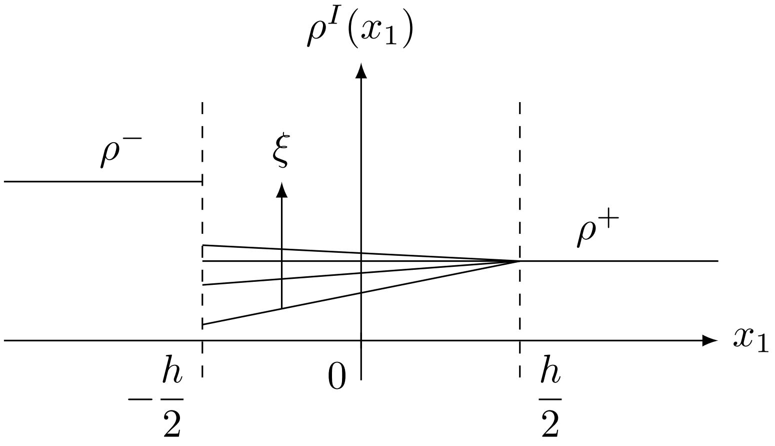

(a) Affine profile

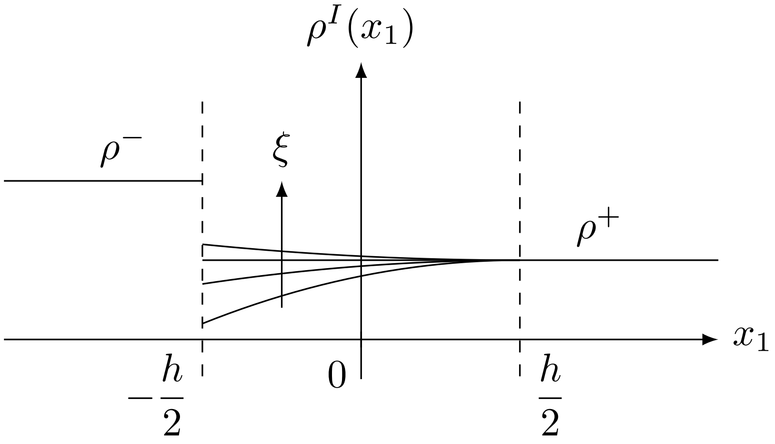

(b) Quadratic profile

Figure 3.3 – Example of density profiles in function of the dimensionless parameter ξ.

3.4.1.2 Quadratic distribution of density

Figure 3.3b shows the configuration, in which the density profile in the interphase is taken, and has the following form

$$\rho^I(x_1) = \frac{1}{4}\rho^+(3+\xi) + \frac{1-\xi}{h}\rho^+ x - \frac{1-\xi}{h^2}\rho^+ x^2, \tag{3.56}$$

that gives

$$m^- = \frac{M_0}{5}\frac{2+3\xi}{2+\xi}, \quad m^+ = \frac{M_0}{10}\frac{9+\xi}{2+\xi}, \quad \gamma = \frac{M_0}{10}\frac{7+3\xi}{2+\xi}. \tag{3.57}$$

3.4.2 Numerical study

In the following, the results issue from the numerical simulation are presented for the two methods investigated. More in detail, on one hand, in Sec. 3.4.2.1 the case of two semi-infinite spaces modeled by two standard Cauchy continua is represented; on the other hand, in Secs. 3.4.2.2 and 3.4.2.3, the situation in which one of the previous two semi-infinite spaces is a second gradient elastic material is illustrated. Moreover, in the results, we show the reflection coefficients as a function of frequency or as a function of the ratio between the thickness of the interphase (h) and the wavelength ($\overline{\lambda}$), that is equivalent because of the following relation

$$\frac{h}{\overline{\lambda}} = f\sqrt{\frac{M_0}{K_1}}, \tag{3.58}$$

where $\overline{\lambda}$ is the average wavelength, f represents the frequency and K_1 the P-wave modulus (see Eq. (3.24)). Because of the dependence of the ratio h/$\overline{\lambda}$ on the mass per unit surface of the interphase (M_0, which has been introduced in Eq. (3.34)), the information coming from this parameter are even more solid. For obtaining a benchmark useful to evaluate the accuracy of the inertial interface model, the differential equations (3.50) are computed *via* the finite element method using the commercial software Mathematica (Wolfram).

In what follows, the results will be presented separately according to the type of density profile of the interface (see Fig. 3.3). For a detailed overview on the numerical value characterizing the inertial surface, please refer to Tab. 3.3. In furter works concerning microstructured interphases, or in presence of damage, these values could also be computed by following approaches similar to those described in [113, 118].

Profile	ξ	M_0 (kg/m^2)	m^- (kg/m^2)	m^+ (kg/m^2)	γ_b (kg/m^2)	K_1 (N/m)
Affine	0.2	0.094	0.039	0.022	0.016	404.
	0.7	0.115	0.041	0.035	0.019	1018.
	1.2	0.137	0.044	0.048	0.023	1454.
Quadratic	0.2	0.077	0.034	0.017	0.013	269.
	0.7	0.109	0.039	0.033	0.018	911.
	1.2	0.141	0.045	0.049	0.023	1545.

Table 3.3 – Numerical values for the parameters characterizing the inertial surface.

3.4.2.1 Case 1: homogeneous continuum without dispersion

Figures 3.4 and 3.5 present three graphs, one for every value of the parameter ξ considered ($\xi = 0.2,\ 0.7,\ 1.2$) for an affine and a quadratic density profile of the interface, respectively. To the meaning of this value, please refer to Fig. 3.3. Therefore, keeping in mind that the interphase between the two semi-infinite spaces has been computed in three different ways, in Figs. 3.4 and 3.5 each curve represents a different interface model, as illustrated in the legend. In particular, black line, which corresponds to the finite element code (the computations refer to what presented in Sec. 3.2.4.1), is assumed as reference. Then, referring to Sec. 3.2.4.2, the red and blue dashed lines correspond to analytical computation considering surface energy. More in detail, on one hand, blue dashed line refers to an non-inertial interface, in which only elastic properties are considered; on the

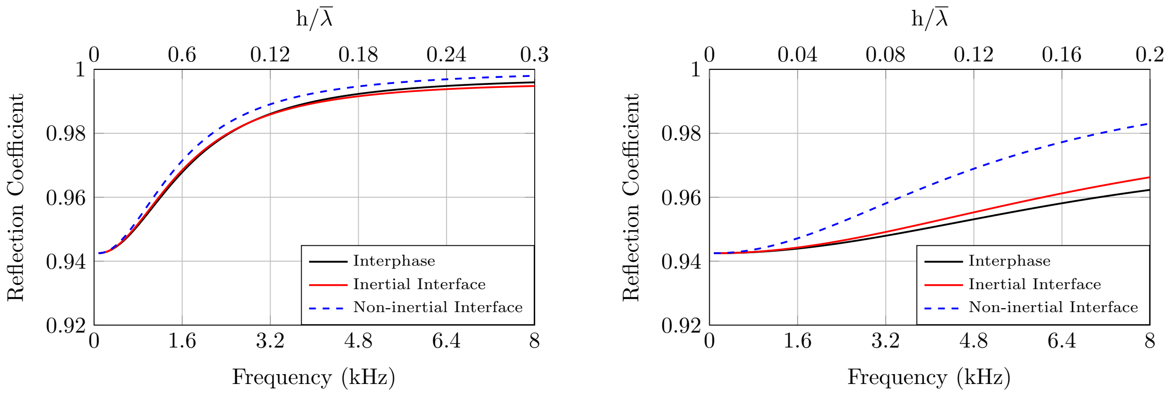

(a) ξ=0.2

(b) ξ=0.7

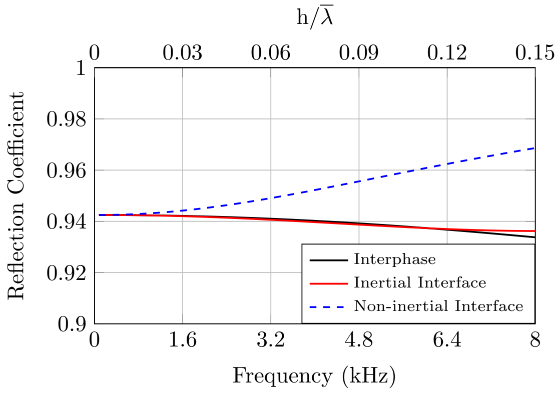

(c) ξ=1.2

Figure 3.4 – Reflection coefficient for case 1 (no dispersion) in the case of affine density profile.

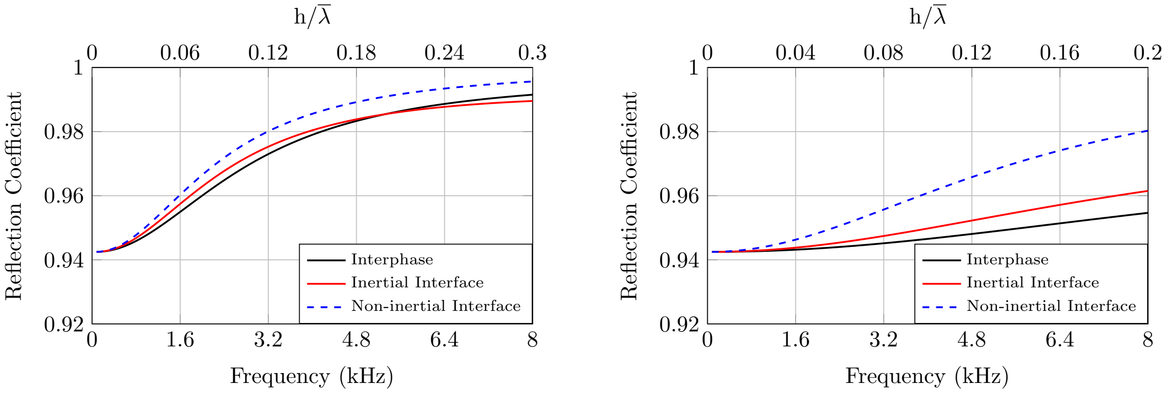

(a) ξ=0.2 (b) ξ=0.7

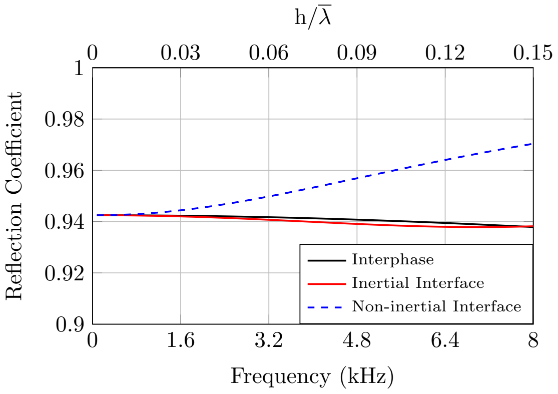

(c) ξ=1.2

Figure 3.5 – Reflection coefficient for case 1 (no dispersion) in the case of quadratic density profile.

other hand, red line corresponds to the inertial interface, in which both elastic and inertial properties are considered at the same time.

In the case of no-dispersion, the dependence on frequency is due to the presence of the interphase. A comparison of the results between an affine and a quadratic density profile confirms the accuracy of the model (in particular for the case of the affine density profile), with respect to the benchmark. For a more detailed analysis of the results, please refer to [101].

3.4.2.2 Case 2: microstructured continuum with normal dispersion

In this case, the interface is still modeled by a Cauchy continuum, while the medium occupying the domain Ω^+ is modeled as a second gradient continuum, as explained in Secs. 3.2.4.1 and 3.2.4.2. The results are presented in Figs. 3.6-3.7-

3.8-3.9.
The same general consideration can be done about the signification of the curves. These curves may be read as the evolution of the reflected coefficient over frequency, but also over the ratio $h/\overline{\lambda}$ (see Eq. (3.58)).

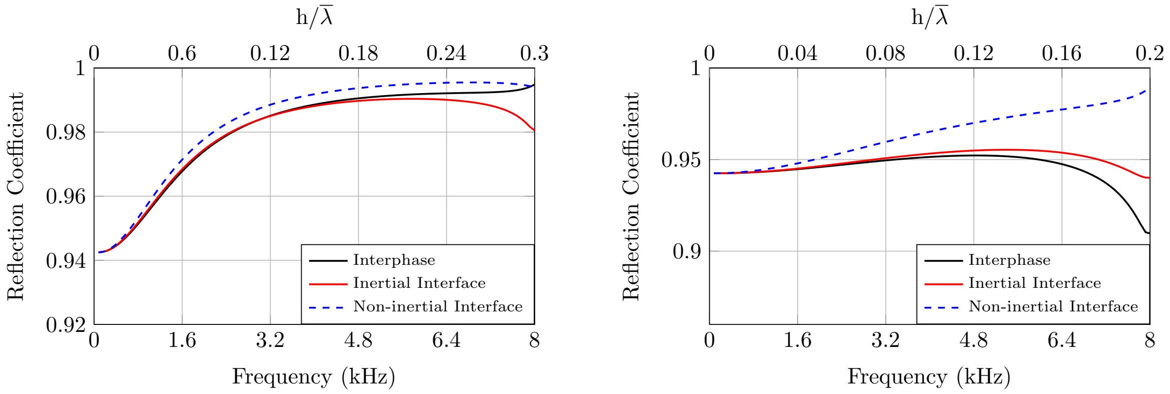

(a) ξ=0.2 (b) ξ=0.7

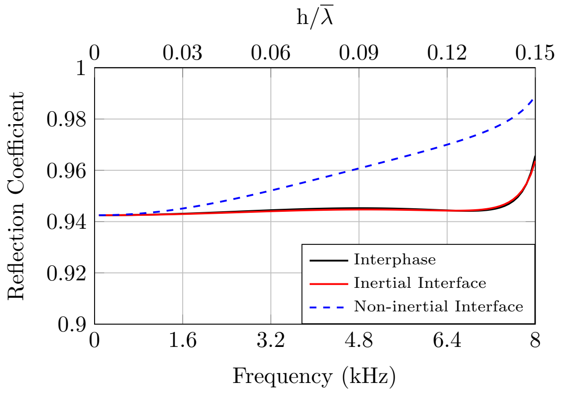

(c) ξ=1.2

Figure 3.6 – Reflection coefficient for case 2 (normal dispersion) in the case of affine density profile.

Starting from the case of normal dispersion, by comparing Figs. 3.4 and Figs. 3.6 or Figs. 3.5 and Figs. 3.7 (for an affine and a quadratic density profile, respectively), the addition of the second gradient is not evident immediately. In fact, at low frequencies, but also until ~ 5 kHz, the results are similar. This confirms what shown in Fig. 3.2, where the influence of the microstructured continuum model are starting to impact and, consequently, the results start diverging at higher frequencies. Therefore, it is possible to appreciate, especially in Figs. 3.6b-3.6c-3.7b-3.7c, that inertial model always better approximate the benchmark (*i.e.* the finite element code) than the non-inertial one. Moreover, at high values of the ratio $h/\overline{\lambda}$,

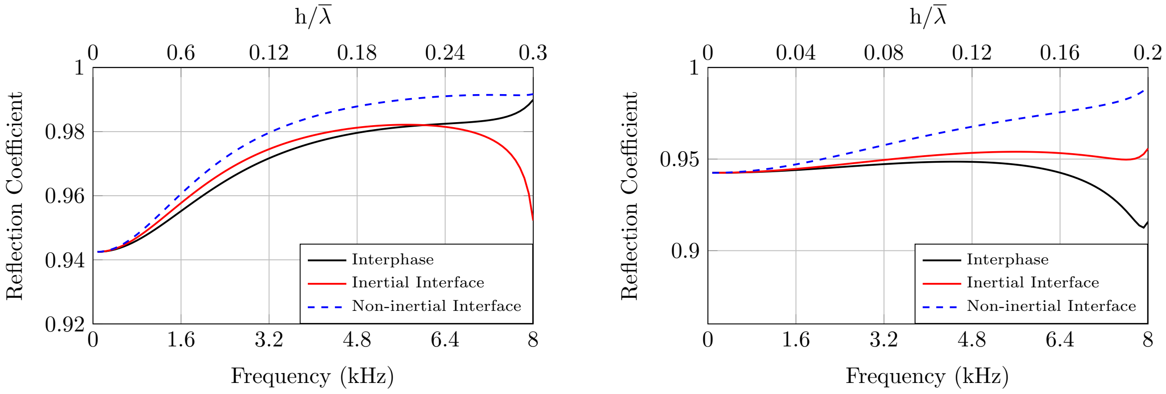

(a) ξ=0.2 (b) ξ=0.7

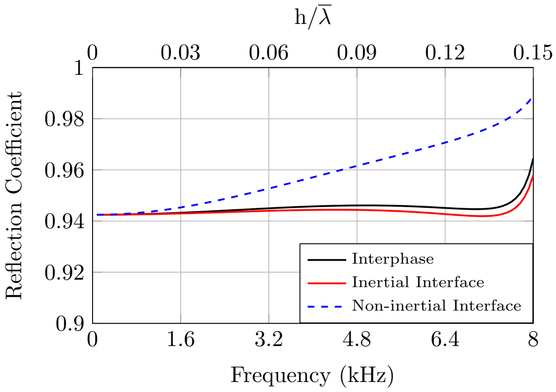

(c) ξ=1.2

Figure 3.7 – Reflection coefficient for case 2 (normal dispersion) in the case of quadratic density profile.

even the inertial model does not capture the correct behavior (*i.e.* the red and the black lines are not perfectly superposed). The reason of that lies in the fact that this model is based on a linear approximation of the velocity field across the surface, which hypothesis is clearly not fulfilled when the ratio $h/\overline{\lambda}$ increases. In addition, the percentage of error (calculated to the referential finite element model) with respect to the ratio $h/\overline{\lambda}$ for the three models has also been considered. More in detail, the errors result to be higher in the case of non-inertial surface ($\sim$ 6% and $\sim$ 5.2% at $h/\overline{\lambda}$=0.17 for the affine and the quadratic density profile, respectively) than in the case of inertial interface ($\sim$ 3.25% and $\sim$ 1.75% at $h/\overline{\lambda}$=0.17 for the affine and the quadratic density profile, respectively).

3.4.2.3 Case 3: microstructured continuum with anomalous dispersion

In the same way, the case of anomalous dispersion can be discussed. Actually, the same remarks can be done by comparing Figs. 3.4 and Figs. 3.8 or Figs. 3.5 and Figs. 3.9 (for an affine and a quadratic density profile, respectively). Also in this case, the second gradient addition does not occur for lower values of frequency. The proposed model still follows better the benchmark, even if not good as the case of normal dispersion. Concerning the errors, the same consideration can be carried out. Indeed, again, the errors result to be higher in the case of non-inertial interface ($\sim$ 3.2% and $\sim$ 3% at $h/\overline{\lambda}$=0.17 for the affine and the quadratic density profile, respectively) than in the case of inertial interface ($\sim$ 1.9% and $\sim$ 1.5% at $h/\overline{\lambda}$=0.17 for the affine and the quadratic density profile, respectively).

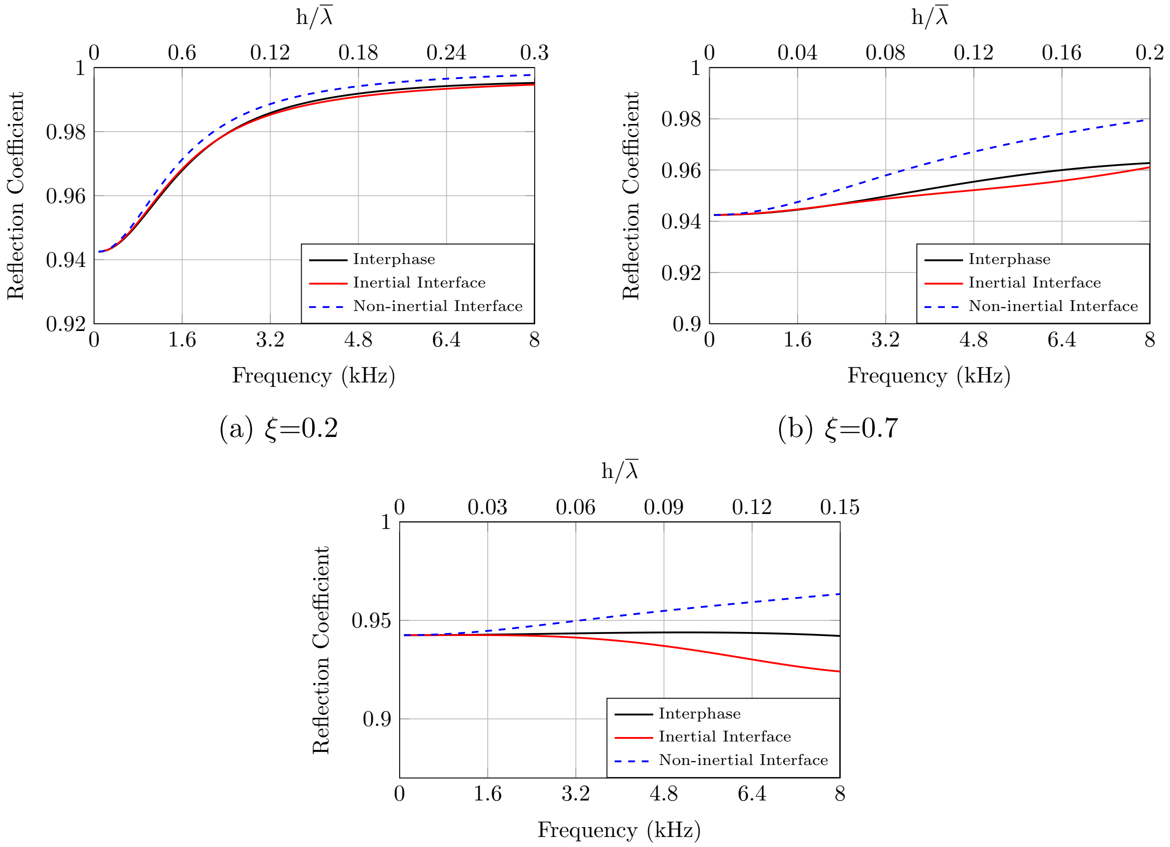

(a) ξ=0.2

(b) ξ=0.7

(c) ξ=1.2

Figure 3.8 – Reflection coefficient for case 3 (anomalous dispersion) in the case of affine density profile.

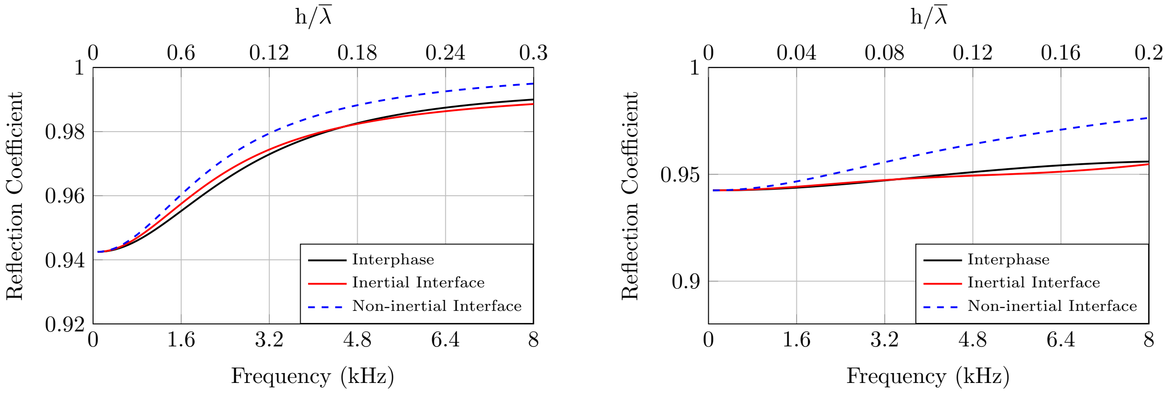

(a) ξ=0.2 (b) ξ=0.7

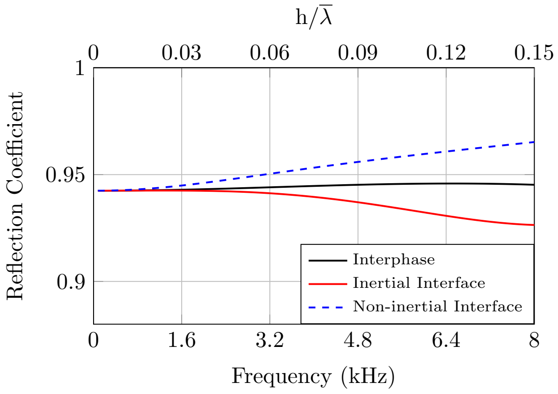

(c) ξ=1.2

Figure 3.9 – Reflection coefficient for case 3 (anomalous dispersion) in the case of quadratic density profile.

3.5 Discussion and conclusions

In a recent paper [101], we studied two standard continua on both sides of the interface/interphase. Here, a microstructured continuum on one side has been considered. In both cases, it was interesting to investigate the effects, on the reflection properties of the interface/interphase, of a transition between a homogeneous and a heterogeneous material, being an abrupt jump of properties not considered. Thus, the characteristics of this interphase is modeled *via* the dimensionless parameter ξ (see Fig. 3.3) and its thickness h. The characteristic length ℓ and the term related to the microinertia h_p (for an overview on the identification of these coefficients refers to [100]) model the microstructures continuum.

It is worth to be noted that the studied geometry resambles the case of the implant-bone interphase, that is located between the trabecular bone and a prosthetic implant. Furthermore, in this context, the parameter ξ can be related to the ostointegration level of the implant.

In Sec. 3.4.2, the results of the numerical simulations carried out by considering a homogeneous as well as a heterogeneous (or microstructured) continuum have been presented. As introduced in Sec. 3.4, three main cases have been considered, which are 1) the non dispersive, 2) the positive dispersive and 3) the negative dispersive cases. The results of the reflection coefficient with respect to the frequency (as well as with respect to the ratio $h/\overline{\lambda}$) have been presented and discussed in Sec. 3.4.2 for both cases of an affine and a quadratic density profile. In a low frequency regime, it is evident that the method proposed in this work better approximate the benchmark. Focusing on the density profile, the greater results are given by the affine one. By the way, also the results obtained for the quadratic density profile are satisfactory. Furthermore, for all cases under exams, the percentage of error with respect to the ratio $h/\overline{\lambda}$ for the three models turned out to be not significant (the maximum stand at $\sim 3.25\%$ and $\sim 1.75\%$ in the case of normal dispersion and at $\sim 1.9\%$ and $\sim 1.5\%$ in the case of anomalous dispersion for the affine and the quadratic density profile, respectively).

Moreover, as already discussed in Sec. 3.2.1, a simple configuration has been considered, where two half-spaces are separated by a layer of thickness h (*i.e.* the interphase).

On the basis of what discussed in the previous sections, in the following points the main considerations and remarks drawn in this work are listed:

- The reflection properties of the interphase have been investigated by considering the second continuum first as an homogeneous continuum and then as a microstructured continuum;
- At lower frequencies both continua show the same behavior, whereas at higher frequencies the effects of the microstructure (and so of the second gradient) can be appreciated;
- When the frequency increases, and the dispersion in the micro-structured medium becomes non-negligible, the second gradient model is more accurate;
- Among the two density profiles taken into account for the interphase, the affine distribution of density resulted to be more accurately represented than the quadratic one.

Concerning finite element computations, the proposed technique provides a considerable advantage in all cases in which the small thickness, or the complex geometry, of the interphase is responsible for mesh refinements and consequently of an increased number of elements in the computation.

Since here only P-waves have been investigated, a future work could test the model by considering S-waves. Furthermore, aiming at characterizing the problem of a bone-implant interphase, another perspective envisaged is represented by testing this model on a configuration in which the first half-space is composed by titanium (Ti) and the second one by a bone substitute (represented by a gyroid-shaped porous structure).

Chapter 4

Evaluation of the dental implant stability: ultrasonic characterization and signal processing

---

The work presented in this chapter is issued from the following publication:

> I. Scala, G. Rosi, V.-H. Nguyen, R. Vayron, G. Haïat, S. Seuret, S. Jaffard, and S. Naili. Ultrasonic characterization and multiscale analysis for the evaluation of dental implant stability: A sensitivity study. *Biomedical Signal Processing and Control*, 42: 37-44, 2018.

Abstract

With the aim of surgical success, the evaluation of dental implant long-term stability is an important task for dentists. About that, the complexity of the newly formed bone and the complex boundary conditions at the bone-implant interface induce the main difficulties. In this context, for the quantitative evaluation of primary and secondary stabilities of dental implants, ultrasound based techniques have already been proven to be effective. The microstructure, the mechanical properties and the geometry of the bone-implant system affect the ultrasonic response. The aim of this work is to extract relevant information about primary stability from the complex ultrasonic signal obtained from a probe screwed to the implant. To do this, signal processing based on multiscale analysis has been used. The comparison between experimental and numerical results has been carried out, and a correlation has been observed between the multifractal signature and the stability. Furthermore, a sensitivity study has shown that the variation of certain parameters (*i.e.* central frequency and trabecular bone density) does not lead to a change in the response.

Keywords: implant stability, multiscale analysis, numerical simulation, sensitivity study, wave propagation.

4.1 Introduction

A correct evaluation of dental implant stability is crucial for surgical success. First of all, two types of stability are of interest:(i) primary or mechanical stability and (ii) secondary or biological stability. Once the implant is inserted in the jawbone, some surface areas come into direct contact with bone. This contact results in primary or mechanical stability and depends on implant shape, bone quality and the preparation of the implant site. Primary stability gradually decreases during bone remodeling process. Thus, it corresponds to the implant stability immediately after surgery. However, secondary stability comes after, during the healing process, when bone remodels and osseointegration occurs. When the healing process is over, mechanical stability is totally replaced by biological stability. By the way, since a good secondary stability could not be obtained in the case of bad primary stability [114], we can say that, in general, the long- term stability strictly depends on its initial stability. In the same way, it is proven that long-term anchorage of a dental implant depends on the quantity and quality of the surrounding bone tissue, the peri-implant bone. Indeed, the bone remodeling occurring at the bone-implant interface [39] leads to changes in the bone architecture in the vicinity of the implant and in its mechanical properties [68]. From a mechanical point of view, modeling difficulties are mostly due to the complexity of newly formed bone tissue (a complex, anisotropic, porous-viscoelastic medium in constant remodeling), to its multiscale and time-evolving nature [38], but also to the boundary conditions at the bone-implant interphase. This means that primary and secondary stabilities are affected by several parameters, as bone quality, bone density or amount of bone in contact with the implant.

In literature, ultrasound based techniques have already been proven to be effective in the quantitative evaluation of primary and secondary stabilities of dental implant [73, 74, 121, 122, 123, 124], for both experiments and numerical simulations. The technique is based on the following assumptions: i) dental implants act as wave guides for ultrasounds; ii) propagation in wave guides is considerably affected by changes in boundary conditions, *i.e.* by different levels of stability. The objective is to inspect the ultrasonic response of the implant information and correlate it to the evolution of stability, by using signal processing techniques. As already pointed out, the ultrasonic response depends on parameters like bone structure, geometry or mechanical properties, which, *in vivo*, all vary in parallel, and whose effect on stability is not clear. Thus, with the aim of analyzing the effect of these parameters, mechanical modeling is a key resource. Indeed, numerical simulation is advantageous with respect to experiences because it can perform, in a controlled manner, a sensitivity analysis with respect to parameters such as bone density and stiffness.

Now, two main issues arise: i) how to evaluate the specific signature left from the aforementioned parameters on the signal and ii) the extraction of the information. Therefore, the signal issued from the measurements is complex. Furthermore, additional difficulties arise because of the limited number of sensors used in the experiences as well as the interference in the signals caused by the considerable attenuation in the tissue. In recent studies developed by our group, the envelope of the signal has been taken into account in signal processing (see *e.g.* [123]). In the literature, similar irregular and complex biological data have already been approached with fractal and/or multifractal analysis [25, 41, 43], with the aim of the characterization and the classification of complex signals. In order to analyze the signal in its wholeness, more advanced signal processing techniques based on wavelet techniques have been introduced in the context of multifractal analysis; but we will use them with a slightly different purpose since, as we will see, multifractal analysis as such cannot be performed for such signals.

Following the technique employed in [73, 74, 121, 122, 123, 124] different levels of implant stability will be artificially induced by a progressive unscrewing on the dental implant. This configuration has been used in both experimental and numerical analysis. The numerical results are obtained by using the finite element

method.
This chapter is structured as follows. After this introduction, Section 4.2 introduces the geometrical configuration of the problem (for which, with the aim of simplifying calculations, an axisymmetric geometry has been considered) and then provides the axial symmetric equations of motion; also the Finite Element (FE) analysis is introduced. Then, Section 4.3 presents a rapid overview on the wavelet based multiscale analysis. Section 4.4 is devoted to the presentation and discussion of the obtained results. Finally, Section 4.5 sets out conclusion and some perspectives.

4.2 Geometrical configuration and Finite Element (FE) analysis

The geometrical configuration reported in Fig. 4.1 shows the axial symmetry with respect to the implant central axis. According to that, an axisymmetric 2D model has been used. A contact planar transducer is placed on the emerging surface of the implant. A double-layer structure of a cortical bone 1 mm thick and an half-space of trabecular bone compose the considered bone model. In the geometrical configuration shown in Fig. 4.1, the titanium dental implant commercialized by Implants Diffusion International (IDI1240, IDI, Montreuil, France), with a length of $L = 11.5$ mm and a diameter of $D = 4$ mm, is recreated. In addition, a specific healing abutment, which helps the gum to heal properly, is inserted in the upper part of the implant. When the implant is totally inserted in the bone specimen, as it is in the configuration considered in this work, we deal with the typical clinical set-up. In the present study, volume forces are neglected and it is assumed that all the considered media exhibit isotropic homogeneous mechanical properties.
The cylindrical coordinates are used and designated by (r, θ, z).
The axisymmetric equations of motion in each subdomain are the following:

$$\rho \ddot{u}_r - \sigma_{rr,r} - \frac{1}{r}\sigma_{rz,z} - \frac{\sigma_{rr} - \sigma_{\theta\theta}}{r} = 0, \tag{4.1}$$

$$\rho \ddot{u}_z - \sigma_{zz,z} - \frac{\sigma_{rz}}{r} = 0, \tag{4.2}$$

where ρ stands for the mass density, u_r and u_z represent, respectively, the radial and axial components of the displacement vector; σ_{rr}, σ_{rz}, $\sigma_{\theta\theta}$, σ_{zz} are the components of the stress tensor $\boldsymbol{\sigma}$; furthermore, the double dot indicates the temporal second partial derivative. According to Hooke's relation, the constitutive relation for an isotropic homogeneous material can be expressed as

$$\boldsymbol{\sigma} = \frac{E\nu}{(1+\nu)(1-2\nu)} \operatorname{Tr}(\boldsymbol{\varepsilon})\mathbb{I} + \frac{E}{(1+\nu)}\boldsymbol{\varepsilon} \tag{4.3}$$

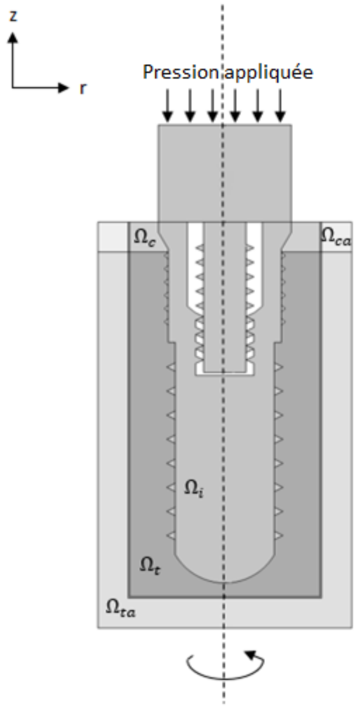

Figure 4.1 – Cross-section view of the 3-D axisymmetric geometrical configuration used in the numerical simulations. The domains are denoted with a subscript corresponding to the trabecular bone (Ω_t), the cortical bone (Ω_c), the implant (Ω_i), and the absorbing layers associated to trabecular and cortical bone (Ω_{ta} and Ω_{ca}, respectively).

where E and ν are Young's modulus and Poisson coefficient, respectively, Tr() is the trace operator of a tensor, $\mathbb{I}$ is the identity tensor and $\boldsymbol{\varepsilon}$ is the strain tensor whose non-zero components are given by

$$\varepsilon_{rr} = u_{r,r}, \qquad \varepsilon_{\theta\theta} = \frac{u_r}{r}, \qquad \varepsilon_{rz} = \frac{1}{2}\left(u_{r,z} + u_{z,r}\right), \qquad \varepsilon_{zz} = u_{z,z}. \tag{4.4}$$

Young's modulus has been considered to be related to the density ρ according to the following power-law relation [26]

$$E = E_0 \left(\frac{\rho}{\rho_0}\right)^{1.96}, \tag{4.5}$$

where the subscript $_0$ indicates the reference values for the Young's modulus E and the density ρ.

The contact planar transducer, placed on the upper emerging surface of the implant specimen (see Fig. 4.1), generates a signal corresponding to a time pulse uniform pressure whose temporal history is expressed as follows

$$p(t) = Ae^{-4(f_c t-1)^2}\sin(2\pi f_c t), \tag{4.6}$$

where A is the amplitude, f_c is the pulse central frequency and t is the time.
The continuity of displacement and stress fields between the subdomains is imposed. Moreover, in order to prevent the non-physical reflected wave generated from the lateral and bottom boundaries of the bone domains, an absorbing layer has been added to the model, as shown in Fig. 4.1. The domain is at rest for $t < 0$, *i.e.* stress and displacement are set to zero everywhere in the domain. At $t = 0$, the uniform pressure given by Eq. (4.6) is imposed on the upper emerging surface of the implant specimen.

4.2.1 Finite Element simulation

In this subsection, the resolution method is described. The boundary value problem defined in Sec. 4.2 was solved by using the software COMSOL Multiphysics (Stokholm, Sweden) which is based on the finite element method.
By the discretization of the equations, a linear system of ordinary differential equations is obtained, which is solved by an implicit generalized α-method in the time domain, a complete description of which can be found in [123]. Briefly, an unstructured mesh of triangular finite elements with quadratic Lagrange interpolating polynomials was used. A critical choice for the convergence of the numerical results concerns the steps of the temporal and spatial discretization. Thus, the element's size of each domain (see Fig. 4.1) was chosen equal to $\lambda_{min}/10$, where λ_{min} represents the smallest wavelength in the domain and it can be computed as $\lambda_{min} = c_{min}/f_{max}$ (for the isotropic elastic media considered here, c_{min} is the shear wave velocity) and f_{max} the maximum value of the frequency range. For this reason, we considered meshes with smoothly varied sizes of elements when there are interfaces between two materials. The mesh of the considered model contains around 10^6 degrees of freedom. The time step has been chosen in order to respect the Courant-Friedrichs-Lewy (CFL) condition, which represents a necessary condition for stability. Thus, in these simulations, the time step is set equal to 1.5×10^{-9} s.

4.2.2 Indicator of the implant stability

The ultrasonic response of the implant is measured by using an echographic mode. The output radio frequency (rf) signal was determined by computing the spatial average of the pressure at the upper surface of the implant (see Fig.4.1). In order to extract information, in [121, 122], the signal envelope, that is the smooth curve outlining the extremes of the signal, has been considered to build an indicator as a scalar quantity proportional to the implant stability. This indicator is indeed based on the temporal variation of the signal amplitude and is defined as

$$I = \sum_{i=1}^{N} S(it_0), \tag{4.7}$$

where N designates the samples number, t_0 is the sampling rate and $S(t)$ the signal envelope. In particular, this indicator has been developed to quantitatively estimate the mean amplitude of the signal. Thus, the signal envelope is computed by considering the absolute value of the Hilbert transform. As an example, in Fig. 4.2 an output signal obtained with our ultrasonic device is presented.
In this work we want to extend the signal processing analysis to the inner structure of the signal. Indeed, since the recorded signal came from multiple reflections at the bone-implant interface, a multi-scale or multi-fractal analysis seems to be appropriate. Details about this signal processing technique will be given in the next section.

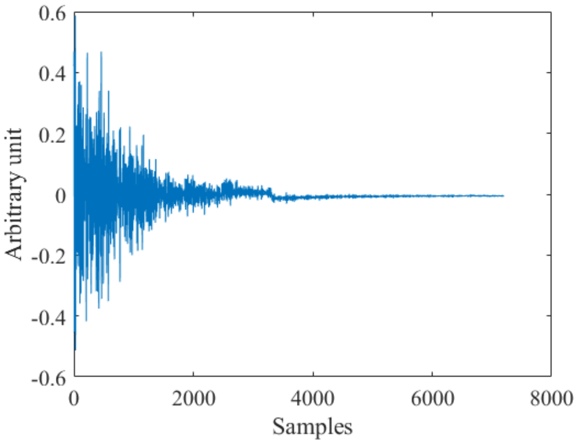

Figure 4.2 – Example of an output signal obtained with our ultrasonic device.

4.3 Signal processing and multiscale analysis

Multifractal analysis has been already employed in medicine to discriminate bone pathologies like osteoporosis [41, 61], to characterize microstructure of porous

media (and, in particular, bone tissue) [103] and infectious diseases [56], to differentiate dentate and edentulous regions [133] and more.
In this work, multifractal tools are employed to extract relevant information from the scaling properties of signals either derived from experimental and numerical data. The aim is to discriminate the implant stability. In fact, both the irregularity as well as the complexity of biological objects led the way to the fractal analysis approach. Multifractal analysis consists in determining *structure functions* associated with the data and discussing their relevance using classification methods or model selection.
The local regularity of a signal is important when dealing with a highly irregular signal. This irregularity strongly characterizes, for example, biomedical signals and images such as ECG, EEC, ultrasound or scan images, etc. These irregularities (or singularities) can be locally quantified by the so-called Hölder exponent ($h_X(t_0)$, where $X(t)$ is the signal). We talk about multifractal signal when the Hölder exponent is not constant (otherwise it is about monofractal signal). In this framework, the fluctuation of h versus t express the variability of the regularity. This is called multifractal spectrum ($D(h)$).
Thus, in this section, the key-concepts used in the following are brefly introduced.

4.3.1 Wavelet basis

Starting with the scaling function $\phi(x)$ and the wavelet $\psi(x)$ (regular and well localized), an orthonormal wavelet basis on $L^2(\mathbb{R})$ (where $L^p(\mathbb{R})$ is the Lebesgue space of p-power integrable functions on real numbers $\mathbb{R}$) is defined as the set of functions $\phi(x-k)$ and $2^{j/2}\psi(2^j x - k)$, where natural number $j \geq 0$ and $k \in \mathbb{Z}$ for which j and k are natural numbers belonging to $\mathbb{Z}$. The basis is "r-smooth" if $\phi(x)$ and $\psi(x)$ have derivatives up to order r which have fast decay. The quantity r is a parameter which has to be picked larger enough depending on the data analyzed; indeed it has to be larger than the highest Hölder exponent present in the data. We denote by $c_{j,k}$ and c_k the *wavelets coefficients* on the function f, which are defined by

$$c_{j,k} = 2^j \int_{\mathbb{R}} f(x)\psi(2^j x - k)dx, \qquad c_k = \int_{\mathbb{R}} f(x)\phi(x-k)dx. \tag{4.8}$$

These coefficients give information on the oscillations of f in the neighborhood of the dyadic interval $\lambda (= \lambda(j,k)) := [k2^{-j}, (k+1)2^{-j})$, which leads to a more compact notation, that is $c_\lambda = c_{j,k}$ and $\psi_\lambda(x) = \psi(2^j x - k)$. This kind of indexation is useful because the wavelet ψ_λ is fundamentally located near the dyadic interval λ. Furthermore, we denote by Λ_j the set of dyadic intervals λ of width 2^{-j}. A $L^1(\mathbb{R})$ normalization for wavelet coefficients is used because it is more natural in order to express scale invariance relations.

4.3.2 Wavelets structure functions

The wavelet structure functions of f are defined by

$$\forall j \in \mathbb{N}, \quad \forall p > 0, \qquad S_f(p,j) = 2^{-j} \sum_{\lambda \in \Lambda_j} |c_\lambda|^p \,, \tag{4.9}$$

where $\mathbb{N}$ refers to the set of all natural numbers.
Multifractal analysis usually proposes to use classification tools based on log-log plot regressions of structure functions (the so-called *scaling functions*, see [2, 3]). However, in our case, log-log plots do not display a clear scaling-invariance behavior (see Fig. 4.4). Therefore, it seems more relevant to base classification directly on the structure functions (note that a similar idea was followed in [4] for old photographic papers). One possibility is to consider quantities which are used in the wavelet characterization of homogeneous Besov spaces $\dot{B}^{0,p}_p(\mathbb{R})$ (the space $\dot{B}^{0,p}_p(\mathbb{R})$ is closely related with the $L^p(\mathbb{R})$ space, see [2, 3]). Besov regularity and the explicit estimation of Besov norms are widely used in signal and image processing, since equivalent noms were derived by Meyer and Donoho and his collaborators who showed how they can be used in denoising algorithms and inverse problems, see *e.g.* [34]. Recall that the wavelet characterization of these spaces implies that, if wavelets are smooth enough (which we assume), then

$$\| f \|^p_{\dot{B}^{0,p}_p(\mathbb{R})} \quad \sim \quad \sum_j 2^{-j} \sum_{\lambda \in \Lambda_j} |c_\lambda|^p = \sum_j S_f(p,j). \tag{4.10}$$

4.4 Results and discussion

To realize this study, we used the Wavelet Leader and Bootstrap [129, 130] based multifractal analysis (WLBMF) toolbox. This analysis has been performed to both experimental data and numerical simulations. As stated above, the signals we deal with have, from a qualitative point of view, a complex structure. Thus, the aim is to extract a quantification of implant stability, and study the sensitivity of this method with respect to changes in bone density, stiffness and with respect to the probe central frequency.

As already said, here we consider both experimental and numerical data. The numerical data are dervived on the basis of what explained in Sec. 4.2. The experimental data come from the work presented in [122]. Rapidly, we can remind that bone samples derive from the proximal part of bovine humeri has been considered. The choice of this particular anatomic location is due to the will of miming the human oral bone tissue. Then, according to what done in the clinic, a cilyndrical cavity has been realized in each bone sample before the implant insertion.

In both experiences and simulations, the variation of stability has been induced in a controlled manner by a progressive unscrewing of 2π-rad of the dental implant, that, in what follows, will be indicated by the number of rotations R. Higher values of the rotation parameters correspond to lower stabilities. A scheme of the implant unscrewing is presented in Fig. 4.3.

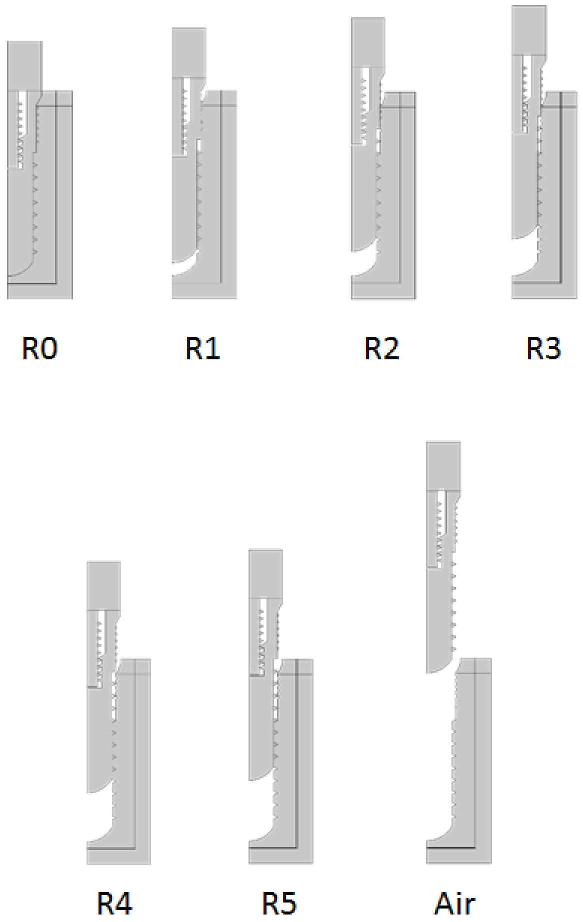

Figure 4.3 – Scheme of the implant unswrewing. We start from the implant completely inserted in the bone tissue, $R0$, then the implant is progressively unscrewed of $2 \times i\pi$-rad, Ri $(i = 0, ..., n)$. Finally, "Air" corresponds the implant completely unscrewed, which means that there is not bone tissue around the implant.

4.4.1 Structure functions

The consideration of structure functions for classification purposes goes back to the seminal work of Kolmogorov in turbulence in 1941 [62], and their wavelet counterpart was introduced by Arneodo and his collaborators at the end of the 1980s.

The results presented in what follows correspond to a specific selection of process parameters settings for the WLBMF toolbox. The two standard analysis methods have been performed, *i.e.* the discrete wavelet transform coefficients (DWT) and the Leaders' wavelets (LWT), with $N_\psi = 3$ vanishing moments. The choice of a wavelet basis requires:

1. the shortness of the filters (which implies faster decomposition algorithms and a larger number of scales on which log-log plot regressions can be computed for the determination of scaling exponents);
2. the regularity of the wavelets and the number of vanishing moments (which allow to deal with larger classes of signals displaying a wider range of singularity exponents).

These two requirements are contradictory, since, for a given class of wavelets, the longer the filters the more vanishing moments. However, when no specific additional requirement is needed (such as *e.g.* symmetry for the filters) Daubechies wavelets present an optimal compromise, and therefore are usually preferred. Those are the reasons why, in what follows, the results presented derive from using Daubechies wavelets.
The scaling range was chosen as $3 \leq j \leq 7$. Over these scales a weighted polynomial regression has been performed. Moreover, we remarked that information can be extracted only for $p \in [1, 3]$, and that the information is equivalent for each p in this range. Thus, in what follows, we assume that $p = 1$.

As stated above, this analysis is performed on experimental and numerical data. For the experiments, with the aim of reproducing the buccal condition, the configuration considered presents a bone porous structure saturated with water and completely immersed. The simulations have been performed by means of the commercial software COMSOL Multiphysics (Stockholm, Sweden).

We start the analysis by the computation of the structure functions (which examine power-law relations for all orders of moments) related to experimental tests and numerical simulations, in order to extract their main features. The results are plotted in Fig. 4.4, for different levels of stability. From the analysis of the structure functions, and their evolution with respect to rotations, the following observations may be exposed:

- small scales (*e.g.* $j < 3$) do not include any information, in fact they are invariant for each case considered;

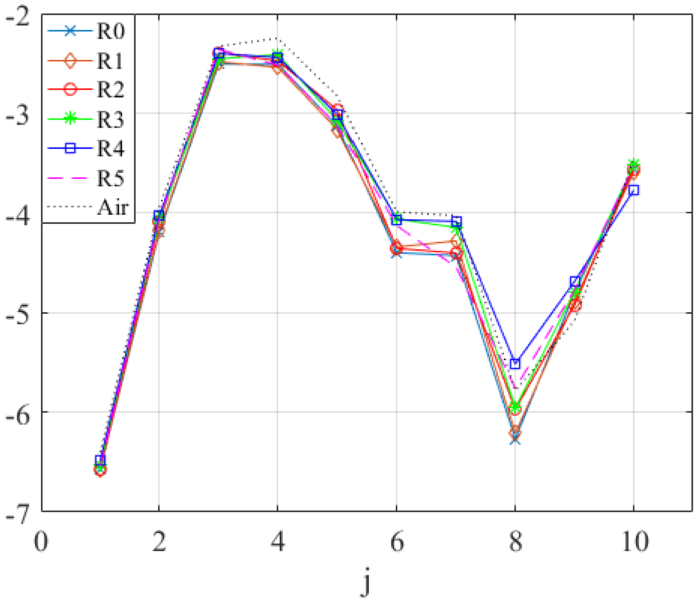

Figure 4.4 – (Colors online). Wavelet structure functions (DWT) (for $p = 1$) performed on the experimental data. On the top left corner a legend for the curves is presented, where "$R0$" represents the implant fully inserted in bone tissue, "Ri" ($i = 0, ..., n$) the implant unscrewed of $2 \times i\pi$-rad, and "Air" the implant located in the air (which means that there is not bone tissue around the implant).

- large scales (*e.g.* $j > 6$) correspond to phenomena not taken into account, such as large fluctuations due to measurement conditions (*e.g.* small movements of the probe);
- following the previous considerations, it is reasonable to take into account only the scale corresponding to $j \in [3, 6]$;
- in contradiction with what is usually met in signal processing, deriving scaling exponents from log-log plots based on such data would not be relevant here.

Using such exponents for classification is the starting point of multifractal analysis methods. Since this is not appropriate here, we will rather base the classification on the richer information supplied by the collection of structure functions at different scales. Note that this option has already shown to be relevant in a different context: for ancient photographic papers classification, structure functions are not scaling invariant because of the typical scales due to the texture of the paper, and classification is performed on structure functions (see [4]).

In the region of interest (ROI) we can observe that: i) the structure functions do not exhibit a linear behavior; ii) the shape does not seem to depend on the configuration. In this context, log-log regressions are not meaningful. As already mentioned earlier in this section, this is not uncommon in multiscale analysis, as structure functions are used also for classification with respect to their shape or the mean values. In light of these observations, mean values have been used in this work.

With the aim of validating this new technique with respect to the results presented in [121, 122, 123, 124], the same simulation with trabecular bone density $\rho = 1170$ kg/m^3 and central frequency $f_c = 10$ MHz are compared for the indicator I, computed following Eq. (4.7), and the mean value of the structure functions.

Therefore, following the classification method described in Sec. 4.3.2, a polynomial regression on the mean values of the structure functions (see Fig. 4.5b) with respect to the unscrewing has been performed. Figure 4.5b illustrates the results for the mean values of the structure functions and, by a comparison with Fig. 4.5a, the coherence with the results for both methods can be appreciated. These results show that a correlation can be clearly observed. A polynomial regression, where the fitted equation presents a quadratic form, well describes the trend of the presented results.

The fact that the mean value of the structure functions increases when the stability is reduced is consistent with the mechanical interpretation of the phenomenon. Indeed, the higher the stability, the more easily the mechanical energy can flow to the surrounding tissues. When the stability is decreased, only a fraction of energy can leave the implant, leading to an higher amplitude of the ultrasonic field. In the specific case considered here, with each rotation of the implant the contact surface with bone is reduced, and so is the mechanical energy flowing out.

In addition, the R-squared coefficient is indicated in the upper left of each figures. This coefficient results to be very close for both cases under exam (see Figs. 4.5a and 4.5b).

Additionally, Figs. 4.5a and 4.5b underline a saturation for low level of stability (*i.e.* for increasing number of rotations).

4.4.2 Sensitivity study

A sensitivity study has been performed in order to test if parameters as trabecular bone density ρ and excitation frequency f_c have an influence on the multiscale study. Actually, the aim of a sensitivity study is to observe how much the variation of the parameters influences the response.

In particular, for each implant unscrewing level, all combinations for the following parameters have been examined:

- ρ: 936, 1053, and 1170 kg/m^3;
- f_c: 8, 9, 10, 11, and 12 MHz.

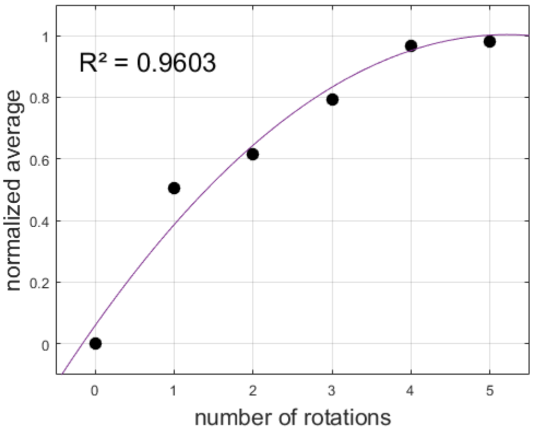

(a)

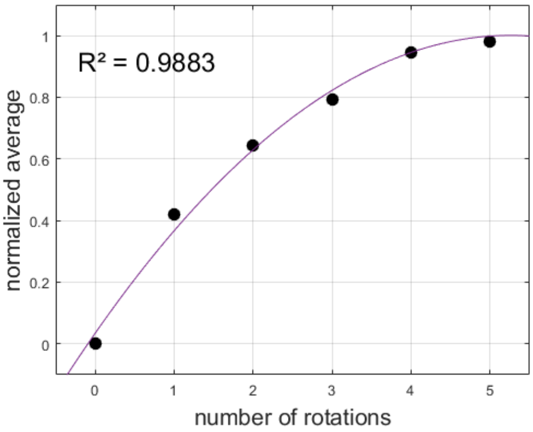

(b)

Figure 4.5 – (Colors online). Polynomial regression for a) the indicator I and b) the mean values of the structure functions (for $p = 1$).

As a reminder, concerning the experiences, the reference values of the trabecular bone density and Young's modulus are given by $\rho_0 = 1170$ kg/m^3 and $E_0 = 2.2108$ GPa. In this sensitivity study, a decreasing of 20% for the trabecular bone density has been considered which carries out $\rho = 936$ kg/m^3. The variation of density and, consequently, the ones of Young's modulus are derived from Eq. (4.5). Moreover, it is important to point out that for all simulations the Poisson's ratio $\nu = 0.3$ remains unchanged. Three trabecular bone densities are examined which are associated to three Young's modulus given in Tab. 4.1.

In this paragraph, the following ”situations” will be presented and discussed:

ρ (kg/m^3)	E (GPa)
1170	2.2108
936	1.4276
1053	1.7983

Table 4.1 – Three trabecular bone densities associated to three Young's modulus for the sensitivity study.

- mean values of the structure functions at fixed p-value, by varying the central frequency f_c to the trabecular bone density ρ;
- mean values of the structure functions at fixed p-value, by varying the trabecular bone density ρ to the central frequency f_c.

The data are presented with respect the number of rotations where the configuration associated is denoted by Ri, for $i = 0, ..., n$. As already said, the configuration associated with R1 corresponds to the implant totally inserted, and then a progressive unscrewing of $i\pi$-rad is realized.

So, the mean values of the structure functions have been analyzed with respect to the variation of frequency (at a fixed value of trabecular bone density) and also to the density (at a fixed value of frequency). Figures 4.6a-4.6c show, by fixing the value of ρ, the evolution of the mean values of the structure functions with respect to changing the frequencies. For a given frequency, the data seem to evolve with implant unscrewing. Furthermore, it is evident that the variation of f_c induces a shift of the curves, but not a distortion in their shape. Actually, starting from 8 MHz, the next curves are like shifted downwards one after another.

Similarly, Figs. 4.7a-4.7c show the evolution of the mean values of the structure functions with respect to changing trabecular bone density and at fixed central frequency. Since the curves are practically superposed, no relevant information can be extracted. It can be only highlighted that a greater solicitation is observable on the implant unscrewing level R2, which corresponds to unscrew the bone implant of π-rad. This consideration has been confirmed also by further simulations considering lower and higher values of trabecular bone density.

Finally, to sum up, with the aim of investigating if central frequency and trabecular bone density represent incident parameters, a sensitivity study has been performed. Hence, the mean values of the structure functions have been considered with respect to the number of rotations R (*i.e.* a progressive unscrewing of the dental implant) by fixing once the central frequency, and then the trabecular bone density. The results obtained show that the response is not affected by the parameters considered.

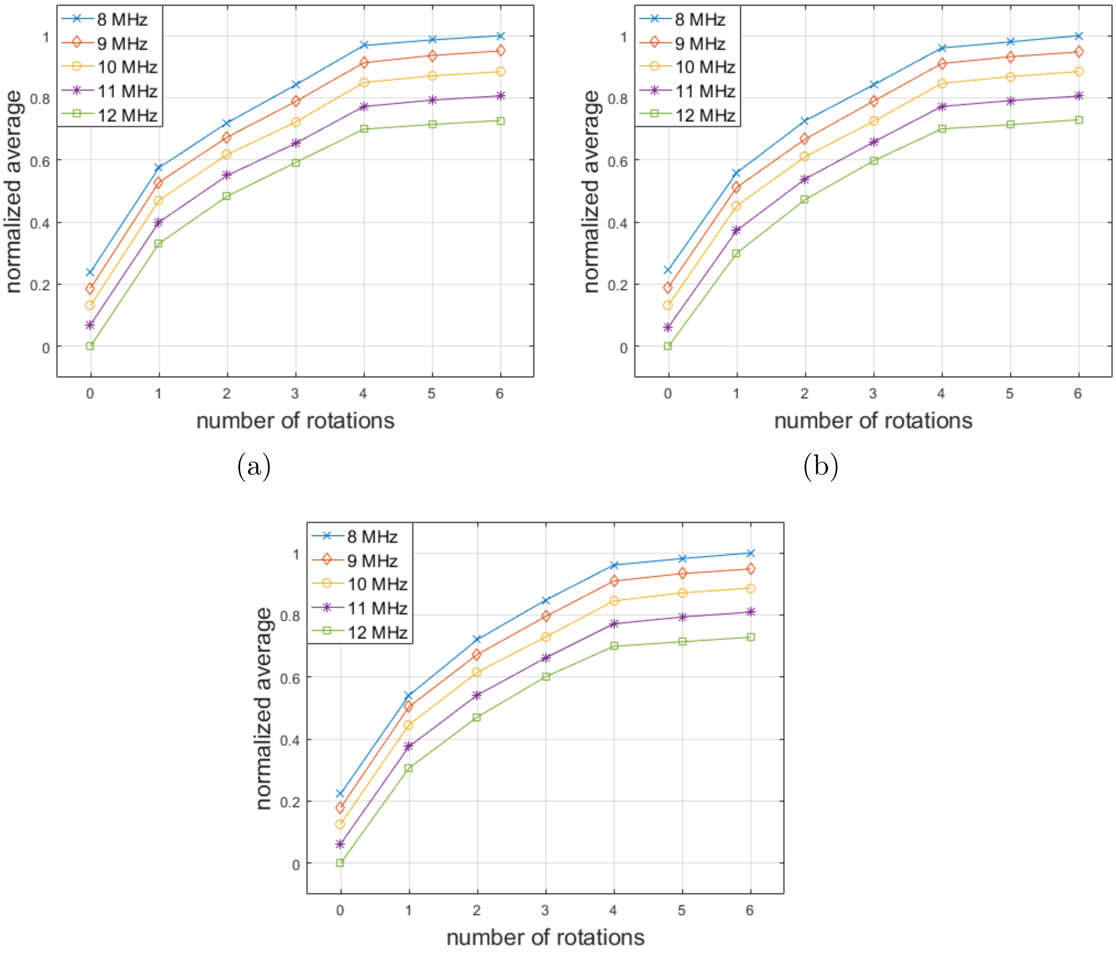

(a)

(b)

(c)

Figure 4.6 – (Colors online). Plots of the mean values of the structure functions to the number of rotations in function of the trabecular bone density: a) $\rho = 936$ kg/m^3, b) $\rho = 1053$ kg/m^3 and c) $\rho = 1170$ kg/m^3. On the top left corner of each figure the legend is given: the different curves represent the correspondent value of central frequency.

4.5 Conclusion

The present work aims at providing a first evidence on the possibility to explore and exploit the multiscale structure of the ultrasonic signal for evaluating dental implant stability. In the example provided, the ultrasonic signal is obtained from a probe fixed to the implant, and the stability is artificially reduced by performing

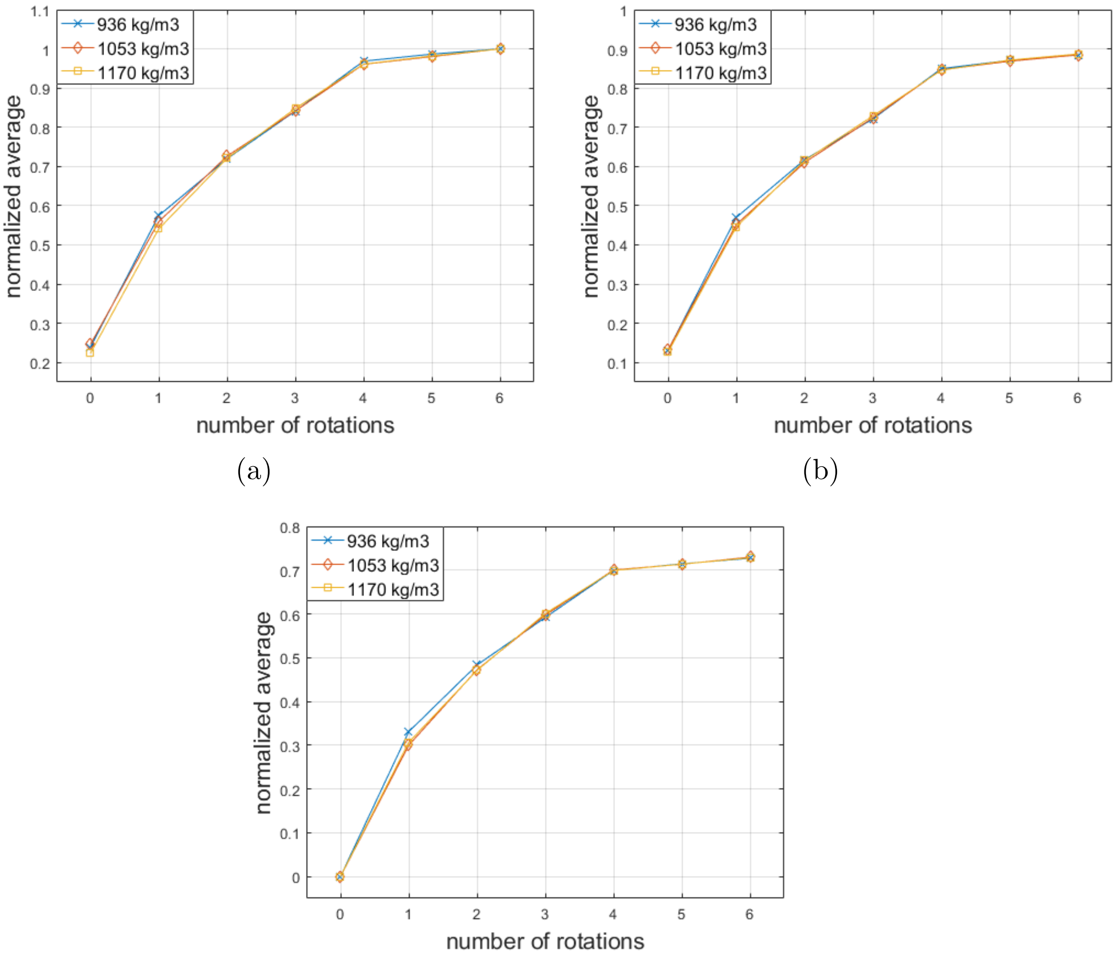

(a) (b)

(c)

Figure 4.7 – (Colors online). Plots of the mean values of the structure functions to the number of rotations in function of the central frequency: a) $f_c = 8$ MHz, b) $f_c = 10$ MHz and c) $f_c = 12$ MHz. On the top left corner of each figure the legend is given: the different curves represent the correspondent value of trabecular bone density.

a progressive unscrewing of the implant itself.

Experimental and numerical results have been compared and then analyzed by signal processing with multiscale methods. Since the use of multifractal analysis has highlighted an absence of log-log regression, the mean values of the structure functions have been considered. By comparison with the indicator used in [73, 74, 121, 122, 123, 124], a coherence between the results can be appreciated.

Furthermore, a sensitivity study has been performed by varying the density of the trabecular bone and the central frequency, showing that these parameters do not have a significant incidence on the evaluation of the stability.
To summarize:

- a 3D axisymmetric configuration has been used for the finite element analysis;
- some preliminary results from multifractal analysis have been carried out;
- the sensitivity study performed has not shown a particular incidence of the parameters investigated in this analysis.

With the aim of introducing a certain fractality in the mechanical model, future works may envisage the introduction of this feature from a geometrical point of view (*e.g.* by using geometrical configurations like Menger sponges and Koch iterations) as well as to find a model which contains ”multifractal elements” [2, 3, 4] by using tools as the scaling exponent, the multifractal spectrum [41] or the log-cumulants.

Conclusion and perspectives

The purpose of this thesis is to develop and validate, numerically, mechanical and signal processing models in order to characterize the mechanical and micro-structural properties of the bone-implant system, by using ultrasonic methods. Between the bone and the implant there is a transient region, that is the *interphase*, where the osteoingration process takes place. In this context, the main difficulty is represented by the complexity of this heterogeneous medium, which is a living tissue whom properties evolve with time. Moreover, as the mature bone, this interphase, which contains newly formed bone tissue, presents a multiscale nature.
On this basis, to understand the predominant phenomena involved and to precisely describe this heterogeneous medium, the complexity of the problem implies a gradual approach.

In the first place, in Chapter 2, with the perspective to properly model the ultrasonic wave propagation in the bone-implant system, we developed a poroelastic model able to take into account the effects dues to the presence of a microstructure. This model presents a generalization of the classic Biot theory, enriched with the higher order derivatives of the displacement field (second gradient). The results for both reflection and transmission have proven to be influenced by the second gradient parameters. Thus, the proposed numerical strategy is validated.

Then, in Chapter 3, with the aim of also taking into account the heterogeneity and the uncertainties resulting from mechanical and micro-structural properties of the interphase region, the model has been adapted by considering a thin layer with both elastic and material properties. This region has been modeled as a transient zone with evolving density profiles. In this way, there is not an abrupt jump between the two media (which are the homogeous medium, *i.e.* the titanium, and the microstructured heterogeneous medium, *i.e.* the bone) but rather an interphase. The accuracy of the model is underlined. According to the results, the influence of the microstructured continuum model starts to impact at higher frequencies. In addition, in this study, both density profiles turned out to be satisfactory.

After that, in Chapter 4, we used an advanced signal processing technique, the multifractal approach, to characterize the bone-implant interphase. In particular, we focused in the experimental and numerical analysis of the dynamic response due to a ultrasonic excitation in a dental implant. The aim was to discriminate the implant stability. To do this, within the large framework of multifractal analysis, here, the mean value of the structure functions has been investigated. After comparison with the method already used in our laboratory (please refer to [73, 74, 121, 122, 123, 124]), a first evidence of the possibility to exploit the multiscale structure of the ultrasonic signal to evaluate the implant stability has been provided. Furthermore, a sensitivity study has been performed and has revealed that the density of the trabecular bone and the central frequency do not have a significant incidence on the evaluation of the stability.

In conclusion, the complex problem of the characterization of the bone-implant interphase has been covered in this work. The main original contributions of this thesis with respect to the existing literature are listed below.

- Addition of the the second gradient parameters to the classical Biot theory in order to take into account the effects due to the presence of the microstructure in the framework of the bone-implant interphase.
- Use of the multifractal approach for the ultrasonic propagation in a heterogeneous medium. In particular, the idea to exploit the multifractal structure of the signal to evaluate dental implant stability is a first.

Further developments

The work presented in this manuscript paves the way for further applications and extensions. The main perspectives envisaged, of which someone is an ongoing project, are listed in the following.

- **Numerical validation of the model including the second gradient parameters with respect to real microstructures.**

  To do this, an ongoing project uses a bone substitute, that can be used for pre-implant surgery in presence of volumetric bone defects, modeled as a gyroid-shaped scaffold. Figure I shows some examples of the gyroid-shaped samples which can be obtained by varying the porosity (ϕ).
  Its ultrasonic behavior is studied. Once characterized this 3D porous structure, we can use it to validate the model presented in Chapter 2.
  At present, only the characterization of the gyroid-shaped scaffold has been

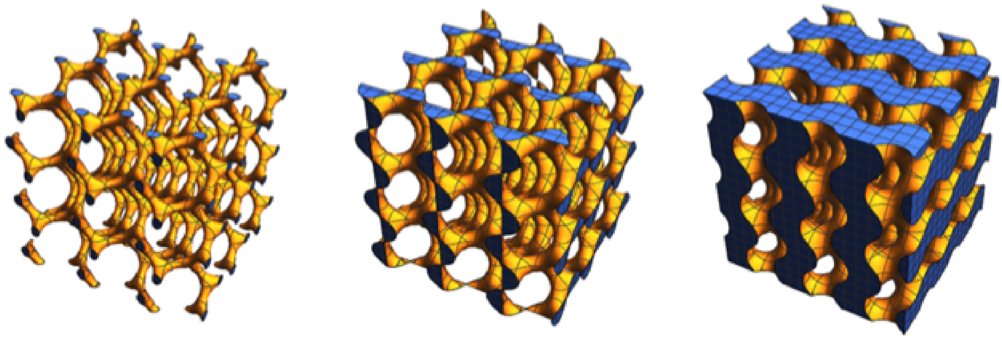

ϕ = 93.6% ϕ = 83.08% ϕ = 49.9%

Figure I – Gyroids' samples for different values of porosity.

realized. Figure II presents some preliminar results for both phase velocity and group velocity for fast and slow waves. The results are illustrated with respect to frequency and the porosity is fixed at $\phi = 80\%$. A dependence of both fast and slow waves on frequency is underlined.

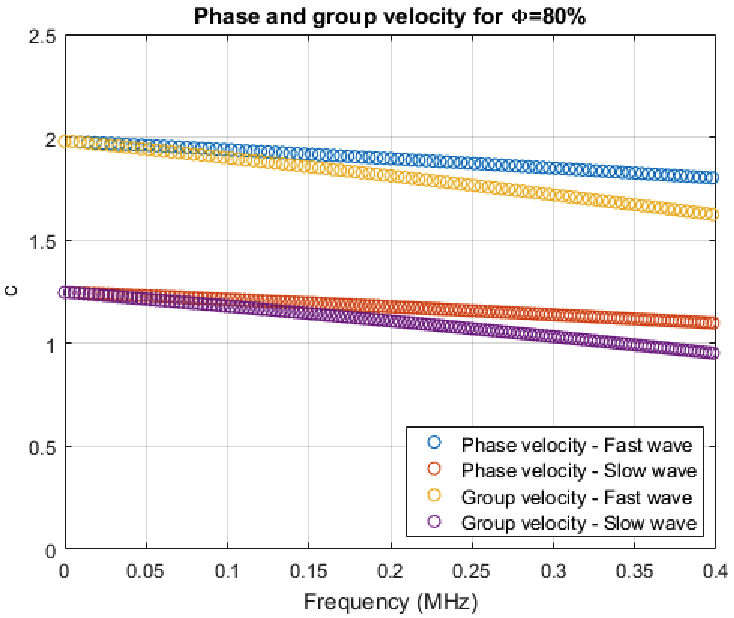

Figure II – Phase velocity (blue and red dotted lines) and group velocity (yellow and purple dotted lines) for fast (blue and yellow dotted lines) and slow (red and purple dotted lines) waves with respect to frequency. The porosity is fixed at $\phi = 80\%$.

Then, a validation of this model also with an experimental campaign on bone or artificial materials is envisaged. We expect a better agreement of the poroelastic model with respect to experimental data, especially in the case of high porosity.
Therefore, always aiming at characterizing the bone-implant interphase, the model presented in Chapter 3 should be tested by using the ease to handle the gyroid-shaped structure to model the implant-interphase-bone system. In this way, the interphase may be modeled, for example, as a gradient of porosity.

- **To move forward in the exploitation of the multifractal analysis in the context of the characterization of the bone-implant interphase.**

  As already announced in Chapter 4, first a certain ”fractality” from a geometrical point of view should be introduced in the system. In particular, an ongoing work (for which the preliminary results are presented in Appendix A) focus on randomized Sierpinski Carpet realized by the percolation process. The first results are encouraging. In the future, other families of fractals should be tested and, even if we deal with a random process, a formulation for the fractal dimension should be given.

Bibliography

[1] A.-e.-n. N. Abd-alla, F. Alshaikh, D. Del Vescovo, and M. Spagnuolo. Plane waves and eigenfrequency study in a transversely isotropic magneto-thermoelastic medium under the effect of a constant angular velocity. *Journal of Thermal Stresses*, 40(9):1079–1092, 2017.

[2] P. Abry, S. Jaffard, and H. Wendt. Irregularities and scaling in signal and image processing: multifractal analysis. *Benoit Mandelbrot: A Life in Many Dimensions*, pages 31–116, 2011.

[3] P. Abry, S. Jaffard, and H. Wendt. A bridge between geometric measure theory and signal processing: Multifractal analysis. In *Operator-Related Function Theory and Time-Frequency Analysis*, pages 1–56. Springer, 2015.

[4] P. Abry, S. G. Roux, H. Wendt, P. Messier, A. G. Klein, N. Tremblay, P. Borgnat, S. Jaffard, B. Vedel, J. Coddington, et al. Multiscale anisotropic texture analysis and classification of photographic prints: Art scholarship meets image processing algorithms. *IEEE Signal Processing Magazine*, 32(4):18–27, 2015.

[5] H. Askes and E. C. Aifantis. Gradient elasticity in statics and dynamics: An overview of formulations, length scale identification procedures, finite element implementations and new results. *International Journal of Solids and Structures*, 48(13):1962–1990, 2011.

[6] N. Auffray, J. Dirrenberger, and G. Rosi. A complete description of bi-dimensional anisotropic strain-gradient elasticity. *International Journal of Solids and Structures*, 69-70:195–206, 2015.

[7] N. Auffray, J. Dirrenberger, and G. Rosi. A complete description of bi-dimensional anisotropic strain-gradient elasticity. *International Journal of Solids and Structures*, 69–70:195–206, 2015.

[8] N. Auffray, H. Le Quang, and Q. C. He. Matrix representations for 3D strain-gradient elasticity. *Journal of the Mechanics and Physics of Solids*, 61(5):1202–1223, 2013.

[9] A. Barkaoui, B. Tlili, A. Vercher-Martínez, and R. Hambli. A multiscale modelling of bone ultrastructure elastic proprieties using finite elements sim-

ulation and neural network method. *Computer methods and programs in biomedicine*, 134:69–78, 2016.

[10] Y. Benveniste. A general interface model for a three-dimensional curved thin anisotropic interphase between two anisotropic media. *Journal of the Mechanics and Physics of Solids*, 54(4):708–734, 2006.

[11] Y. Benveniste and T. Miloh. Imperfect soft and stiff interfaces in two-dimensional elasticity. *Mechanics of materials*, 33(6):309–323, 2001.

[12] A. Berezovski, J. Engelbrecht, and G. A. Maugin. Numerical simulation of two-dimensional wave propagation in functionally graded materials. *European Journal of Mechanics-A/Solids*, 22(2):257–265, 2003.

[13] A. Berezovski, I. Giorgio, and A. D. Corte. Interfaces in micromorphic materials: wave transmission and reflection with numerical simulations. *Mathematics and Mechanics of Solids*, 21(1):37–51, 2016.

[14] D. Bigoni and A. Movchan. Statics and dynamics of structural interfaces in elasticity. *International Journal of Solids and Structures*, 39(19):4843–4865, 2002.

[15] A. Bilotta and E. Turco. Elastoplastic analysis of pressure-sensitive materials by an effective three-dimensional mixed finite element. *ZAMM-Journal of Applied Mathematics and Mechanics/Zeitschrift für Angewandte Mathematik und Mechanik*, 97(4):382–396, 2017.

[16] M. A. Biot. Theory of elasticity and consolidation for a porous anisotropic solid. *Journal of Applied Physics*, 26(2):182–185, 1955.

[17] M. A. Biot. Theory of Propagation of Elastic Waves in a Fluid Saturated Porous Solid. II. Higher Frequency Range. *J. Acoust. Soc. Am.*, 28(2):179–191, 1956.

[18] M. A. Biot and D. G. Willis. The elastic coefficients of the theory of consolidation. *J. appl. Mech*, 15:594–601, 1957.

[19] C. Boutin. Microstructural effects in elastic composites. *International Journal of Solids and Structures*, 33(7):1023–1051, 1996.

[20] P. Brånemark. Osseointegrated implants in the treatment of the edentulous jaw. *Scand J Plast Reconstr Surg*, 11, 1977.

[21] M. Brun, S. Guenneau, A. B. Movchan, and D. Bigoni. Dynamics of structural interfaces: filtering and focussing effects for elastic waves. *Journal of the Mechanics and Physics of Solids*, 58(9):1212–1224, 2010.

[22] J. Caeiro, P. González, and D. Guede. Biomechanics and bone (& ii): Trials in different hierarchical levels of bone and alternative tools for the determination of bone strength. In *Rev. Osteoporosis Metab. Miner.*, volume 5, pages 1–13, 01 2013.

[23] A. Carcaterra, F. Dell'Isola, R. Esposito, and M. Pulvirenti. Macroscopic description of microscopically strongly inhomogenous systems: A mathematical basis for the synthesis of higher gradients metamaterials. *Archive for Rational Mechanics and Analysis*, 218(3):1239–1262, 2015.

[24] J. Chaboche, R. Girard, and A. Schaff. Numerical analysis of composite systems by using interphase/interface models. *Computational Mechanics*, 20(1-2):3–11, 1997.

[25] D. Chappard, M.-F. Baslé, E. Legrand, and M. Audran. Trabecular bone microarchitecture: a review. *Morphologie*, 92(299):162–170, 2008.

[26] S. C. Cowin, editor. *Bone mechanics handbook*. CRC Press, Boca Raton, FL, USA, 2001.

[27] S. C. Cowin. *Bone Mechanics Handbook, Second Edition*. CRC Press, 2001.

[28] R. de Boer, W. Ehlers, and Z. Liu. One-dimensional transient wave propagation in fluid-saturated incompressible porous media. *Archive of Applied Mechanics*, 63(1):59–72, 1993.

[29] F. dell'Isola, M. Guarascio, and K. Hutter. A variational approach for the deformation of a saturated porous solid. A second-gradient theory extending Terzaghi's effective stress principle. *Archive of Applied Mechanics*, 70(5):323–337, 2000.

[30] F. Dell'Isola, A. Madeo, and L. Placidi. Linear plane wave propagation and normal transmission and reflection at discontinuity surfaces in second gradient 3D continua. *ZAMM Zeitschrift fur Angewandte Mathematik und Mechanik*, 92(1):52–71, 2011.

[31] F. Dell'Isola, A. Madeo, L. Placidi, et al. Linear plane wave propagation and normal transmission and reflection at discontinuity surfaces in second gradient 3d continua. *ZAMM-Journal of Applied Mathematics and Mechanics/Zeitschrift für Angewandte Mathematik und Mechanik*, 92(1):52–71, 2012.

[32] F. dell'Isola, P. Seppecher, and A. Madeo. Boundary conditions at fluid-permeable interfaces in porous media: A variational approach. *International Journal of Solids and Structures*, 46(17):3150–3164, 2009.

[33] F. Dell'Isola, U. Andreaus, and L. Placidi. At the origins and in the vanguard of peridynamics, non-local and higher-gradient continuum mechanics: An underestimated and still topical contribution of gabrio piola. *Mathematics and Mechanics of Solids*, 20(8):887–928, 2015.

[34] D. L. Donoho and I. M. Johnstone. Minimax estimation via wavelet shrinkage. *Ann. Statist.*, 26(3):879–921, 06 1998.

[35] J. Engelbrecht and A. Berezovski. Reflections on mathematical models of deformation waves in elastic microstructured solids. *Mathematics and Mechanics of Complex Systems*, 3(1):43–82, 2015.

[36] J. Engelbrecht, A. Berezovski, F. Pastrone, and M. Braun. Waves in microstructured materials and dispersion. *Philosophical Magazine*, 85(33-35):4127–4141, 2005.

[37] Z. E. A. Fellah, J. Y. Chapelon, S. Berger, W. Lauriks, and C. Depollier. Ultrasonic wave propagation in human cancellous bone: application of Biot theory. *The Journal of the Acoustical Society of America*, 116(1):61–73, 2004.

[38] H. M. Frost. Bone's mechanostat: a 2003 update. *The Anatomical Record*, 275(2):1081–1101, 2003.

[39] Y. Gabet, D. Kohavi, R. Voide, T. L. Mueller, R. Müller, and I. Bab. Endosseous implant anchorage is critically dependent on mechanostructural determinants of peri-implant bone trabeculae. *Journal of Bone and Mineral Research*, 25(3):575–583, 2010.

[40] Z. Gao, W. Hong, Y. Xu, T. Zhang, Z. Song, and J. Liu. Osteoporosis diagnosis based on the multifractal spectrum features of micro-ct images and c4. 5 decision tree. In *Pervasive Computing Signal Processing and Applications (PCSPA), 2010 First International Conference on*, pages 1043–1047. IEEE, 2010.

[41] Z. Gao, W. Hong, Y. Xu, T. Zhang, Z. Song, and J. Liu. Osteoporosis diagnosis based on the multifractal spectrum features of micro-ct images and c4.5 decision tree. In *Pervasive Computing Signal Processing and Applications (PCSPA), 2010 First International Conference on Pervasive Computing, Signal Processing and Applications*, pages 1043–1047. IEEE, 2010.

[42] H. Georgiadis, I. Vardoulakis, and E. Velgaki. Dispersive rayleigh-wave propagation in microstructured solids characterized by dipolar gradient elasticity. *Journal of Elasticity*, 74(1):17–45, 2004.

[43] W. Geraets and P. Van der Stelt. Fractal properties of bone. *Dentomaxillofacial Radiology*, 29(3):144–153, 2000.

[44] I. Giorgio, U. Andreaus, F. Dell'Isola, and T. Lekszycki. Viscous second gradient porous materials for bones reconstructed with bio-resorbable grafts. *Extreme Mechanics Letters*, 13:141–147, 2017.

[45] I. Giorgio, U. Andreaus, D. Scerrato, and P. Braidotti. Modeling of a non-local stimulus for bone remodeling process under cyclic load: Application to a dental implant using a bioresorbable porous material. *Mathematics and Mechanics of Solids*, 22(9):1790–1805, 2017.

[46] I. Giorgio, U. Andreaus, D. Scerrato, and F. Dell'Isola. A visco-poroelastic model of functional adaptation in bones reconstructed with bio-resorbable materials. *Biomechanics and modeling in mechanobiology*, 15(5):1325–1343, 2016.

[47] I. Giorgio, U. Andreaus, D. Scerrato, and F. Dell'Isola. A visco-poroelastic model of functional adaptation in bones reconstructed with bio-resorbable materials. *Biomechanics and modeling in mechanobiology*, 15(5):1325–1343, 2016.

[48] H. Gouin. Interfaces endowed with nonconstant surface energies revisited with the d'alembert–lagrange principle. *Mathematics and Mechanics of Complex Systems*, 2(1):23–43, 2013.

[49] P. A. Gourgiotis, H. G. Georgiadis, and I. Neocleous. On the reflection of waves in half-spaces of microstructured materials governed by dipolar gradient elasticity. *Wave Motion*, 50(3):437–455, 2013.

[50] S. Gu and Q.-C. He. Interfacial discontinuity relations for coupled multifield phenomena and their application to the modeling of thin interphases as imperfect interfaces. *Journal of the Mechanics and Physics of Solids*, 59(7):1413–1426, 2011.

[51] G. Haïat, M. Sasso, S. Naili, and M. Matsukawa. Ultrasonic velocity dispersion in bovine cortical bone: An experimental study. *The Journal of the Acoustical Society of America*, 124(3):1811–1821, 2008.

[52] G. Haïat, M. Sasso, S. Naili, and M. Matsukawa. Ultrasonic velocity dispersion in bovine cortical bone: an experimental study. *The Journal of the Acoustical Society of America*, 124(3):1811–1821, 2008.

[53] G. Haïat, H.-L. Wang, and J. Brunski. Effects of biomechanical properties of the bone–implant interface on dental implant stability: from *in silico* approaches to the patient's mouth. *Annual review of biomedical engineering*, 16:187–213, 2014.

[54] M. A. Hakulinen, J. S. Day, J. Töyräs, M. Timonen, H. Kröger, H. Weinans, I. Kiviranta, and J. S. Jurvelin. Prediction of density and mechanical properties of human trabecular bone *in vitro* by using ultrasound transmission and backscattering measurements at 0.2-6.7 MHz frequency range. *Physics in medicine and biology*, 50(8):1629–1642, 2005.

[55] S. Hans and C. Boutin. Dynamics of discrete framed structures: a unified homogenized description. *Journal of Mechanics of Materials and Structures*, 3(9):1709–1739, 2008.

[56] A. M. Holdsworth, N. K.-R. Kevlahan, and D. J. Earn. Multifractal signatures of infectious diseases. *Journal of The Royal Society Interface*, 9(74):2167–2180, 2012.

[57] A. Hosokawa and T. Otani. Acoustic anisotropy in bovine cancellous bone. *The Journal of the Acoustical Society of America*, 103(5):2718–2722, 1998.

[58] E. R. Hughes, T. G. Leighton, G. W. Petley, and P. R. White. Ultrasonic propagation in cancellous bone: A new stratified model. *Ultrasound in Medicine and Biology*, 25(5):811–821, 1999.

[59] E. R. Hughes, T. G. Leighton, P. R. White, and G. W. Petley. Investigation of an anisotropic tortuosity in a biot model of ultrasonic propagation in cancellous bone. *The Journal of the Acoustical Society of America*, 121(1):568–574, 2007.

[60] L. Jeannin and L. Dormieux. Poroelastic behaviour of granular media with poroelastic interfaces. *Mechanics Research Communications*, 83:27–31, 2017.

[61] M. Khider, B. Haddad, and A. T. Ahmed. Multifractal analysis by the large deviation spectrum to detect osteoporosis. In *Systems, Signal Processing and their Applications (WoSSPA), 2013 8th International Workshop on*, pages 112–115. IEEE, 2013.

[62] A. N. Kolmogorov. The local structure of turbulence in incompressible viscous fluid for very large reynolds numbers. *Proceedings: Mathematical and Physical Sciences*, 434(1890):9–13, 1991.

[63] P. Laugier and G. Haïat. *Bone Quantitative Ultrasound*. Springer Science & Business Media, 2010.

[64] T. Lekszycki and F. Dell'Isola. A mixture model with evolving mass densities for describing synthesis and resorption phenomena in bones reconstructed with bio-resorbable materials. *ZAMM-Journal of Applied Mathematics and Mechanics/Zeitschrift für Angewandte Mathematik und Mechanik*, 92(6):426–444, 2012.

[65] Y. Li, A. M. Waas, and E. M. Arruda. A closed-form, hierarchical, multi-interphase model for composites—derivation, verification and application to nanocomposites. *Journal of the Mechanics and Physics of Solids*, 59(1):43–63, 2011.

[66] Y. Liu, N. Xu, and J. Luo. Modeling of interphases in fiber-reinforced composites under transverse loading using the boundary element method. *Journal of Applied Mechanics*, 67(1):41–49, 2000.

[67] B. Lombard and J. Piraux. Numerical treatment of two-dimensional interfaces for acoustic and elastic waves. *Journal of Computational Physics*, 195(1):90–116, 2004.

[68] G. Luo, A. M. Sadegh, H. Alexander, W. Jaffe, D. Scott, and S. C. Cowin. The effect of surface roughness on the stress adaptation of trabecular architecture around a cylindrical implant. *Journal of Biomechanics*, 32(3):275–284, 1999.

[69] A. Madeo, F. dell'Isola, N. Ianiro, and G. Sciarra. A variational deduction of second gradient poroelasticity II: an application to the consolidation problem. *Journal of Mechanics of Materials and Structures*, 3(4):607–625, 2008.

[70] A. Madeo, L. Placidi, and G. Rosi. Towards the Design of Metamaterials with Enhanced Damage Sensitivity: Second Gradient Porous Materials. *Research in Nondestructive Evaluation*, 25(2):99–124, 2014.

[71] B. B. Mandelbrot. The fractal geometry of nature/revised and enlarged edition. *New York, WH Freeman and Co., 1983, 495 p.*, 1983.

[72] K. R. Marutyan, M. R. Holland, and J. G. Miller. Anomalous negative dispersion in bone can result from the interference of fast and slow waves. *The Journal of the Acoustical Society of America*, 120(5):EL55–EL61, 2006.

[73] V. Mathieu, F. Anagnostou, E. Soffer, and G. Haiat. Numerical simulation of ultrasonic wave propagation for the evaluation of dental implant biomechanical stability. *The Journal of the Acoustical Society of America*, 129(6):4062–4072, 2011.

[74] V. Mathieu, F. Anagnostou, E. Soffer, and G. Haïat. Ultrasonic evaluation of dental implant biomechanical stability: an in vitro study. *Ultrasound in Medicine & Biology*, 37(2):262–270, 2011.

[75] R. D. Mindlin. Micro-structure in linear elasticity. *Archive for Rational Mechanics and Analysis*, 16(1):51–78, 1964.

[76] A. Misra and P. Poorsolhjouy. Granular micromechanics model for damage and plasticity of cementitious materials based upon thermomechanics. *Mathematics and Mechanics of Solids*, page 1081286515576821, 2015.

[77] Y. Nagatani and R. O. Tachibana. Multichannel instantaneous frequency analysis of ultrasound propagating in cancellous bone. *The Journal of the Acoustical Society of America*, 135(3):1197–1206, 2014.

[78] V. H. Nguyen and S. Naili. Simulation of ultrasonic wave propagation in anisotropic poroelastic bone plate using hybrid spectral/finite element method. *International Journal for Numerical Methods in Biomedical Engineering*, 28(8):861–876, 2012.

[79] V. H. Nguyen and S. Naili. Ultrasonic wave propagation in viscoelastic cortical bone plate coupled with fluids: a spectral finite element study. *Computer methods in biomechanics and biomedical engineering*, 16(9):963–974, 2012.

[80] V. H. Nguyen and S. Naili. Semi-analytical solution of transient plane waves transmitted through a transversely isotropic poroelastic plate immersed in fluid. *Journal of Engineering Mathematics*, 86(1):125–138, 2014.

[81] V. H. Nguyen, S. Naili, and V. Sansalone. A closed-form solution for in vitro transient ultrasonic wave propagation in cancellous bone. *Mechanics Research Communications*, 37(4):377–383, 2010.

[82] V. H. Nguyen, S. Naili, and V. Sansalone. Simulation of ultrasonic wave propagation in anisotropic cancellous bone immersed in fluid. *Wave Motion*, 47(2):117–129, 2010.

[83] P. H. F. Nicholson, G. Lowet, C. M. Langton, J. Dequeker, and G. Van der Perre. A comparison of time domain and frequency-domain approaches to ultrasonic velocity measurement in trabecular bone. *Physics in Medicine & Biology*, 41(11):2421–2435, 1996.

[84] J. Niiranen, J. Kiendl, A. H. Niemi, and A. Reali. Isogeometric analysis for sixth-order boundary value problems of gradient-elastic kirchhoff plates. *Computer Methods in Applied Mechanics and Engineering*, 316:328–348, 2017.

[85] M. Pakula, F. Padilla, P. Laugier, and M. Kaczmarek. Application of Biot's theory to ultrasonic characterization of human cancellous bones: determination of structural, material, and mechanical properties. *The Journal of the Acoustical Society of America*, 123(4):2415–2423, 2008.

[86] S. Papargyri-Beskou, D. Polyzos, and D. E. Beskos. Wave dispersion in gradient elastic solids and structures: A unified treatment. *International Journal of Solids and Structures*, 46(21):3751–3759, 2009.

[87] S. Papargyri-Beskou, D. Polyzos, and D. E. Beskos. Wave propagation in 3-D poroelastic media including gradient effects. *Archive of Applied Mechanics*, 82(10-11):1569–1584, 2012.

[88] S. Papargyri-Beskou, S. V. Tsinopoulos, and D. E. Beskos. Transient dynamic analysis of a fluid-saturated porous gradient elastic column. *Acta Mechanica*, 222(3-4):351–362, 2011.

[89] L. Placidi, F. dell'Isola, N. Ianiro, and G. Sciarra. Variational formulation of pre-stressed solid-fluid mixture theory, with an application to wave phenomena. *European Journal Of Mechanics A-Solids*, 27(4):582–606, 2008.

[90] L. Placidi, G. Rosi, I. Giorgio, and A. Madeo. Reflection and transmission of plane waves at surfaces carrying material properties and embedded in second-gradient materials. *Mathematics and Mechanics of Solids*, 19(5):555–578, 2014.

[91] B. Pukánszky. Interfaces and interphases in multicomponent materials: past, present, future. *European Polymer Journal*, 41(4):645–662, 2005.

[92] Y. Rahali, I. Giorgio, J. Ganghoffer, and F. Dell'Isola. Homogenization à la piola produces second gradient continuum models for linear pantographic lattices. *International Journal of Engineering Science*, 97:148–172, 2015.

[93] O. Riekkinen, M. A. Hakulinen, M. Timonen, J. Toyras, and J. S. Jurvelin. Influence of overlying soft tissues on trabecular bone acoustic measurement at various ultrasound frequencies. *Ultrasound in Medicine and Biology*, 32(7):1073–1083, 2006.

[94] R. Rizzoni and F. Lebon. Imperfect interfaces as asymptotic models of thin curved elastic adhesive interphases. *Mechanics Research Communications*, 51:39–50, 2013.

[95] G. Rosi and N. Auffray. Anisotropic and dispersive wave propagation within strain-gradient framework. *Wave Motion*, 63:120–134, 2016.

[96] G. Rosi, I. Giorgio, and V. A. Eremeyev. Propagation of linear compression waves through plane interfacial layers and mass adsorption in second gradient fluids. *ZAMM-Journal of Applied Mathematics and Mechanics/Zeitschrift für Angewandte Mathematik und Mechanik*, 93(12):914–927, 2013.

[97] G. Rosi, A. Madeo, and J. L. Guyader. Switch between fast and slow Biot compression waves induced by "second gradient microstructure" at material discontinuity surfaces in porous media. *International Journal of Solids and Structures*, 50(10):1721–1746, 2013.

[98] G. Rosi, V. H. Nguyen, and S. Naili. Reflection of acoustic wave at the interface of a fluid-loaded dipolar gradient elastic half-space. *Mechanics Research Communications*, 56:98–103, 2014.

[99] G. Rosi, V. H. Nguyen, and S. Naili. Surface waves at the interface between an inviscid fluid and a dipolar gradient solid. *Wave Motion*, 53:51–65, 2015.

[100] G. Rosi, L. Placidi, and N. Auffray. On the validity range of strain-gradient elasticity: a mixed static-dynamic identification procedure. *European Journal of Mechanics-A/Solids*, 69:179–191, 2018.

[101] G. Rosi, L. Placidi, V.-H. Nguyen, and S. Naili. Wave propagation across a finite heterogeneous interphase modeled as an interface with material properties. *Mechanics Research Communications*, 84:43 – 48, 2017.

[102] G. Rosi, I. Scala, V.-H. Nguyen, and S. Naili. Wave propagation in strain gradient poroelastic medium with microinertia: closed-form and finite element solutions. *Zeitschrift für angewandte Mathematik und Physik*, 68(3):58, 2017.

[103] D. Sanchez-Molina, J. Velazquez-Ameijide, V. Quintana, C. Arregui-Dalmases, J. R. Crandall, D. Subit, and J. R. Kerrigan. Fractal dimension and mechanical properties of human cortical bone. *Medical engineering & physics*, 35(5):576–582, 2013.

[104] J. D. Savage and R. Rajagopal. Dental implants. `http://www.aomsurgery.com/dental-implants/cost-of-implants/`.

[105] I. Scala, G. Rosi, V.-H. Nguyen, and S. Naili. Closed-form and finite element solutions of wave propagation in strain gradient poroelastic medium with micro inertia. In *Poromechanics VI*, pages 1690–1697. Sixth Biot Conference on Poromechanics, 2017.

[106] I. Scala, G. Rosi, V.-H. Nguyen, S. Naili, R. Vayron, G. Haïat, S. Seuret, and S. Jaffard. Evaluation of dental implant stability using ultrasonic characterization and multifractal analysis. AFM, Association Française de Mécanique, 2017.

[107] I. Scala, G. Rosi, V.-H. Nguyen, R. Vayron, G. Haïat, S. Seuret, S. Jaffard, and S. Naili. Ultrasonic characterization and multiscale analysis for the evaluation of dental implant stability: A sensitivity study. *Biomedical Signal Processing and Control*, 42:37–44, 2018.

[108] I. Scala, G. Rosi, L. Placidi, V.-H. Nguyen, and S. Naili. Effects of the microstructure and density profiles on wave propagation across an interface with material properties. *Continuum Mechanics and Thermodynamics*, pages 1–16, 2019.

[109] M. Schanz. Poroelastodynamics: linear models, analytical solutions and numerical methods. *Applied Mechanics Reviews*, 62(3):30803, 2009.

[110] M. Schanz and H. Antes. Application of 'operational quadrature methods' in time domain boundary element methods. *Meccanica*, 32:179–186, 1997.

[111] G. Sciarra, F. dell'Isola, and O. Coussy. Second gradient poromechanics. *International Journal of Solids and Structures*, 44(20):6607–6629, 2007.

[112] G. Sciarra, F. dell'Isola, N. Ianiro, and A. Madeo. A variational deduction of second gradient poroelasticity I: general theory. *Journal of Mechanics of Materials and Structures*, 3(3):507–526, 2008.

[113] A. Selvadurai. A mixed boundary value problem in potential theory for a bimaterial porous region: An application in the environmental geosciences. *Mathematics and Mechanics of Complex Systems*, 2(2):109–122, 2014.

[114] L. Sennerby and N. Meredith. Resonance frequency analysis: measuring implant stability and osseointegration. *Compendium of continuing education in dentistry (Jamesburg, NJ: 1995)*, 19(5):493–8, 1998.

[115] S. M. Suhr. *A Fractal-Based Mathematical Model for Cancellous Bone Growth Considering the Hierarchical Nature of Bone*. PhD thesis, Wright State University, 2016.

[116] M. C. Sukop. Porosity, percolation thresholds, and water retention behavior of random fractal porous media. 2001.

[117] D. Ta, W. Wang, K. Huang, Y. Wang, and L. H. Le. Analysis of frequency dependence of ultrasonic backscatter coefficient in cancellous bone. *The Journal of the Acoustical Society of America*, 124(6):4083–4090, 2008.

[118] E. Turco. A strategy to identify exciting forces acting on structures. *International Journal for Numerical Methods in Engineering*, 64(11):1483–1508, 2005.

[119] B. Vafaeian, L. Le, T. Tran, M. El-Rich, T. El-Bialy, and S. Adeeb. Microscale finite element modeling of ultrasound propagation in aluminum trabecular bone-mimicking phantoms: A comparison between numerical simulation and experimental results. *Ultrasonics*, 68:17 – 28, 2016.

[120] I. Vardoulakis and D. E. Beskos. Dynamic behavior of nearly saturated porous media. *Mechanics of Materials*, 5(1):87–108, 1986.

[121] R. Vayron, P. Karasinski, V. Mathieu, A. Michel, D. Loriot, G. Richard, G. Lambert, and G. Haïat. Variation of the ultrasonic response of a dental implant embedded in tricalcium silicate-based cement under cyclic loading. *Journal of Biomechanics*, 46(6):1162–1168, 2013.

[122] R. Vayron, V. Mathieu, A. Michel, and G. Haïat. Assessment of in vitro dental implant primary stability using an ultrasonic method. *Ultrasound in Medicine & Biology*, 40(12):2885–2894, 2014.

[123] R. Vayron, V. H. Nguyen, R. Bosc, S. Naili, and G. Haïat. Finite element simulation of ultrasonic wave propagation in a dental implant for biomechanical stability assessment. *Biomechanics and Modeling in Mechanobiology*, 14(5):1021–1032, 2015.

[124] R. Vayron, V.-H. Nguyen, R. Bosc, S. Naili, and G. Haïat. Assessment of the biomechanical stability of a dental implant with quantitative ultrasound: A three-dimensional finite element study. *The Journal of the Acoustical Society of America*, 139(2):773–780, 2016.

[125] K. R. Waters and B. K. Hoffmeister. Kramers-Kronig analysis of attenuation and dispersion in trabecular bone. *The Journal of the Acoustical Society of America*, 118(6):3912–3920, 2005.

[126] K. A. Wear. Frequency dependence of ultrasonic backscatter from human trabecular bone: theory and experiment. *The Journal of the Acoustical Society of America*, 106(6):3659–3664, 1999.

[127] K. A. Wear. Measurements of phase velocity and group velocity in human calcaneus. *Ultrasound in Medicine and Biology*, 26(4):641–646, 2000.

[128] K. A. Wear. Measurements of phase velocity and group velocity in human calcaneus. *Ultrasound in Medicine and Biology*, 26(4):641–646, 2000.

[129] H. Wendt, P. Abry, and S. Jaffard. Bootstrap for empirical multifractal analysis. *IEEE Signal Processing Magazine*, 24(4):38–48, 2007.

[130] H. Wendt, S. G. Roux, S. Jaffard, and P. Abry. Wavelet leaders and bootstrap for multifractal analysis of images. *Signal Processing*, 89(6):1100–1114, 2009.

[131] J. L. Williams. Ultrasonic wave propagation in cancellous and cortical bone: prediction of some experimental results by Biot's theory. *The Journal of the Acoustical Society of America*, 91(2):1106–1112, 1992.

[132] S. T. Yaghoubi, V. Balobanov, S. M. Mousavi, and J. Niiranen. Variational formulations and isogeometric analysis for the dynamics of anisotropic gradient-elastic euler-bernoulli and shear-deformable beams. *European Journal of Mechanics-A/Solids*, 69:113–123, 2018.

[133] F. Yasar and F. Akgunlu. Fractal dimension and lacunarity analysis of dental radiographs. *Dentomaxillofacial Radiology*, 34(5):261–267, 2005.

Appendix A

Investigation of the multifractal response of random fractals realized by percolation process

A.1 Introduction

Fractal geometries are often found in the biological materials. Even if there are not perfect fractals at all scales (as it happens instead for each natural structure), in the human body, we can find several structures that can be considered as such. For example, we need only think to the tree-shaped structers of lungs, to the small intestine, to the bloodstream, to the neuron patterns, to the bone tissue, etc. Historically, the first organ identified as fractal has been the pulmonary system. Biologically, this organisation allows above all to maximize the interaction with a greater surface, and, consequently, to have something space saving. Then, biologists found a fractal organisation at all levels of human body, *i.e.* self-similar properties at smaller and smaller levels.

Because of the irregularity and also the complexity of biological objects, a Euclidean geometrical quantification is often too difficult. This led the way to the fractal analysis approach.

In the case of bone tissue, there are structure changes at cellular scale, thus, as already said, it is not a perfect fractal, but rather a *biological* fractal. In this context, several fractal parameters can be investigated to characterize the microstructure of porous media (especially bone tissue). In the literature, the most studies focus on parameters such as:

- the fractal dimension (FD), which can be seen as a measure of the irregularity of many physical process;

- the lacunarity, a term introduced by Mandelbrot [71] to describe fractals' characteristics of same dimension but different texture appearance;
- the multifractal spectrum, which gives information about the variability of the function regularity.

The FD of human bone porous microstructure is related to its mechanical properties [103]. Therefore, FD and lacunarity can differentiate quantitatively the textures differences of trabecular bone radiographies [133]. Concerning the multifractal spectrum, it has been used to classify bone micro-architecture texture and so to discriminate pathological and normal cases [40, 61].

Thus, the multifractal analysis has several applications in medicine, allowing to characterize the microstructure of porous media and discriminate some patologies. There are applications for medical imaging, osteoporosis, heart rate, diagnostic for cancer, diabetic retinopathie, pharmacology, etc.

The present Appendix can be considered as a sequel of the work presented in Chapter 4 [107]. In fact, in order to continue exploring and exploiting the multiscale structure of the ultrasonic signal *via* the multifractal analysis, here a "fractality" in the mechanical model, from the geometrical point of view, has been introduced.

After a dissertion about the considered geometrical configuration and a rapid overview on the finite-difference time-domain (FDTD) method (used here for the simulations), the preliminar results for the structure functions are presented and discussed.

A.2 Geometrical configuration

Before introducing the geometrical configuration, it is important to give an overview of its main component, that is the fractal structure, and how it is generated. In particular, random fractals realized by percolation process have been considered here because of their scale properties.

In the generation of this geometry, three parameters are handled:

- the maximum number of iterations of a Sierpiński Carpet, which is given by counting the number of black boxes $N_n = 8^n$;
- the probability of getting a pore at each iteration level (1/9 for standard carpet), denoted with p;
- the fractal scaling parameter (3 for standard Sierpiński Carpet), denoted with b.

In what follows, we will firstly describe the general case of the generation of random fractals and then focus on the *modus operandi* of the generator used in this work. Let the probability of getting a pore at each iteration level be a number with $0 < p < 1$. We denote the starting unit square ($p = 0$) as E_0. Then, we divided it

into 9 squares of sides 1/3. Now, these squares, E_1, have independent probability p of being selected. And so we can go on. All can be resumed by considering that E_k is a random collection of squares of side 3^{-k}. In this way, we have described in what consists a general random fractal.
Now, according to [116], the generator that we used in the following distinguishes beetween a homogeneous and a heterogeneous case. In the homogeneous case, a random permutation of the integer 1 through b^E is assigned to each site of a lattice and then make those with an integer value $j \leq pb^E$ solids. Here, E is the Euclidian embedding dimension 1, 2, or 3. On the other hand, in the heterogeneous case, we can summarize the steps to generate the prefractals as follows:

1. set the probability p that a site is a solid;
2. generate a uniformly distributed random number in the interval $[0, 1]$ for each site in a space divided into b^E sites;
3. if the random number is greater than p, make the site a pore.

An example of the 2D geometry that can be obtained is shown in Fig. A.1 (in black is represented the solid and in white the pores).

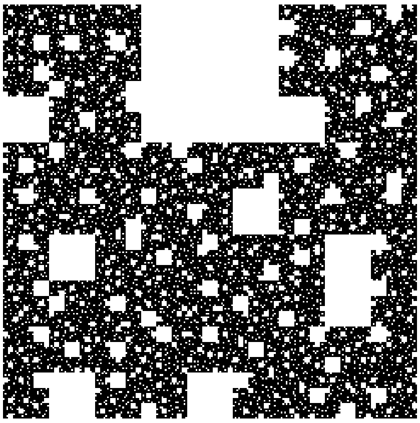

Figure A.1 – Geometry for iteration 5, $p = 0.1$ (which corresponds to a porosity of $\phi = 32.05\%$) and $b = 3$.

Figure A.2 shows the geometrical configuration: three repetitions of the random fractal (in yellow) for iteration 5, $p = 0.1$ and $b = 3$ are dipped in water (in blue). The random fractal used here derives from the the Sierpiński Carpet, a plane fractal, which consists of subdividing a shape into smaller copies of itself, removing one or more copies, and continuing recursively (depending on the iteration chosen). Then, the parameter b, which, as already said, is the fractal scaling parameter, is set equal to 3 because this is the value for standard Sierpiński Carpet. In addition, the probability to have a pore (and so a hole in the solid) at each iteration level,

p, is 1/9 for standard carpet.
The repetition of the chosen fractal geometry gives enough time and space to the signal to travel and interact with the microstructure.
On the axes, we have the pixels dimensions.

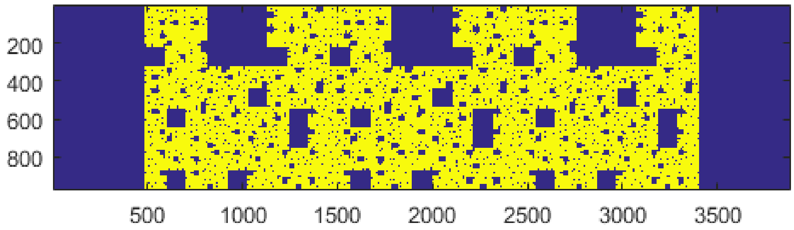

Figure A.2 – Geometrical configuration.

The transducer, located in the first fluid domain (as well as the receiver), generates a signal correspondent to the fractional brownian motion. The representation of the signal source is illustrated in Fig. A.3.

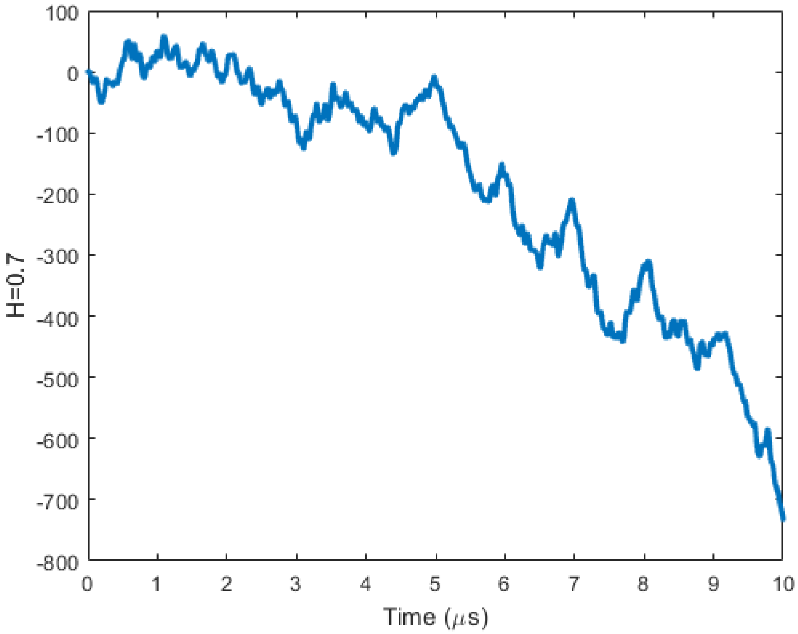

Figure A.3 – Signal source: fractional brownian motion for $H = 0.7$, where H corresponds to the Hurst parameter H $(0 < H < 1)$.

A.3 FTDT method

The open software SimSonic2D have been used to perform numerical simulations. This software is based on the Finite-Difference Time-Domain (FTDT) method, which computations are based on the system of elastodynamic equations, that in the cartesian coordinates read

$$\rho(x)\dot{v}_i(x,t) = \sum_{j=1}^{d} \sigma_{ij,j}(x,t) + \theta_{ij}(x,t),$$

$$\dot{\sigma}_{ij}(x,t) = \sum_{j=1}^{d}\sum_{i=1}^{d} C_{ijkl}(x)v_{k,l}(x,t) + f_i(x,t),$$

where x and t are the time and space variable, respectively, $\rho(x)$ represents the mass density, C_{ijkl} is the fourth rigidity tensor and d is the space dimension (which in SimSonic2D is $d = 2$). The considered media are completely defined by these parameters. Moreover, $v_i(x,t)$ is the displacement velocity, $\sigma_{ij}(x,t)$ the stress tensor, f_i are the vector components of force sources and θ_{ij} are the tensor components of strain rate sources. Through this set of equations, the propagation in heterogeneous, anisotropic and elastic media is fully described. In this model, absorption is not taken into account.

Using a Voigt notation and cosidering the symmetry of the rigidity tensor, we are able to rewrite the equations above under matrix form in the following 2D formulation

$$\begin{bmatrix} \dot{\sigma}_{11} \\ \dot{\sigma}_{22} \\ \dot{\sigma}_{12} \end{bmatrix} = \begin{bmatrix} C_{11} & C_{12} & 0 \\ C_{12} & C_{22} & 0 \\ 0 & 0 & C_{66} \end{bmatrix} \begin{bmatrix} v_{1,1} \\ v_{2,2} \\ v_{2,1} + v_{1,2} \end{bmatrix}.$$

Concerning the boundary conditions, we have:

- symmetry conditions on the upper and lower boundaries of the geometrical configuration;
- PML (perfectly matched layer) condition elsewhere.

The PML condition is commonly used to truncate computational regions in numerical methods to simulate problems with open boundaries, especially in the FDTD and FE methods. In particular, it works out so that if we have a non-PML medium with PML boundaries, the waves incident upon these boundaries do not reflect at the interface.

In order to obtain the convergence of the numerical results, that one of temporal (Δt) and spatial (Δx) resolution is a key-choice. With this in mind, in the present study the element's sizes of each domain are equal to $\lambda_{min}/40$, where λ_{min} is the smallest wavelength in the domain and it can be computed as $\lambda_{min} = c_{min}/f$, where c_{min} represents the smallest speed of sound among all those present and

f is the central frequency. The time step has been chosen in order to respect a necessary condition for convergence, *i.e.* the Courant-Friedrichs-Lewy (CFL) condition. This stability condition is given by the following equation

$$\Delta t \leq \frac{1}{\sqrt{d}} \cdot \frac{\Delta x}{c_{max}},$$

where d is the space dimension (here $d = 2$), and c_{max} is the largest speed of sound among all those present.

A.4 Signal processing

In Chapter 4 we have already talk about the use of multifractal analysis in medicine. If the work presented there aimed at giving a first evidence of the possibility to exploit this advanced signal processing technique to evaluate dental implant stability, here the objective is to dig deep in the exploration and exploitation of the multiscale structure of the ultrasonic signal. In particular, now, fractal elements are added in the mechanical model.
The results presented in the following refer to the key-concepts introduced in Chapter 4.

A.5 Results and discussion

In this study, the simulations have been performed through the open source software SimSonic2D (cf. Sec. A.3). Then, the results have been analysed *via* the Wavelet Leader and Bootstrap based multifractal analysis (WLBMF) toolbox [129, 130].
As already done for Chapter 4, a selection of the process parameters settings is necessary. Two types of analysis have been performed: the discrete wavelet transform (DWT) and the Leaders' wavelet transform (LWT), with $N_\psi = 3$ vanishing moments. Here, the scaling range was chosen as $9 \leq j \leq 13$. Therefore, since we can extract coherent results for all positive as well as for all negative values of q, in the following only two representative examples (*i.e.* $q = 3$ and $q = -3$) will be presented.

In the simulation performed two materials have been considered: the water as fluid and the titanium for the fractal geometry, which in Fig. A.2 have been respresented in blue and yellow, respectively. Note that, concerning the materials, the choice of titanium instead of bone is done to have more evident results in the ultrasonic response, but the same (with the same results) can be do for bone tissue. Mass density ρ and elastic constants in the two media considered in this

	ρ [g/cm^3]	$C_{11} = C_{22} = C_{33}$ [GPa]	$C_{12} = C_{31} = C_{23}$ [GPa]	$C_{44} = C_{55} = C_{66}$ [GPa]
Water	1.0	2.25	2.25	0
Titanium (Ti)	4.42	163.0	80.282	41.357

Table A. I – Mass density and elastic constants used to model water and porous implant substitute properties.

study are summarized in Tab. A. I. In particular, $C_{11} = C_{22} = C_{33} = \lambda + 2\mu$, $C_{12} = C_{31} = C_{23} = \lambda$ and $C_{44} = C_{55} = C_{66} = \mu$, where λ and μ are the classic Lamé coefficients.
The central frequency was set equal to 20 MHz.

Moreover, concerning the fractal parameters four values of p (for which the correspondence to the percentage of porosity is given in Table A. II) and three values of the fractal scaling parameter b ($b = 3, 4, 5$) are investigated.

p	porosity (ϕ)
0.1	32.05%
0.2	57.94%
0.3	76.8%
0.4	88.86%

Table A. II – Correspondance between the values p and the percentage of porosity (ϕ) of the sample.

An example of an output of the simulations performed *via* SimSonic2D is given in Fig. A.4. In particular, this output signal corresponds to the simulations with the geometrical configuration shown in Fig. A.2, for wich $p = 0.1$ and $b = 3$.

In the following, the results for the structure functions are given. In particular, Figs. A.5-A.6 show the results for $q = 3$ and Fig. A.7 for $q = -3$.

In addition, concerning Fig. A.7 a zoom is presented, so that we focus on the scaling range $8 \leq j \leq 12$, and only the results for LWT are illustrated (this is common for $q < 0$). For all results, we can remark a clear separation between the fractal scaling values. Thus, a monotone trend with respect to the parameter b (with $b = 3, 4, 5$) is evident.

Since we deal with a random structure, both fractal parameters investigated (p and q) in the construction of the geometry affect the fractal dimension (FD).

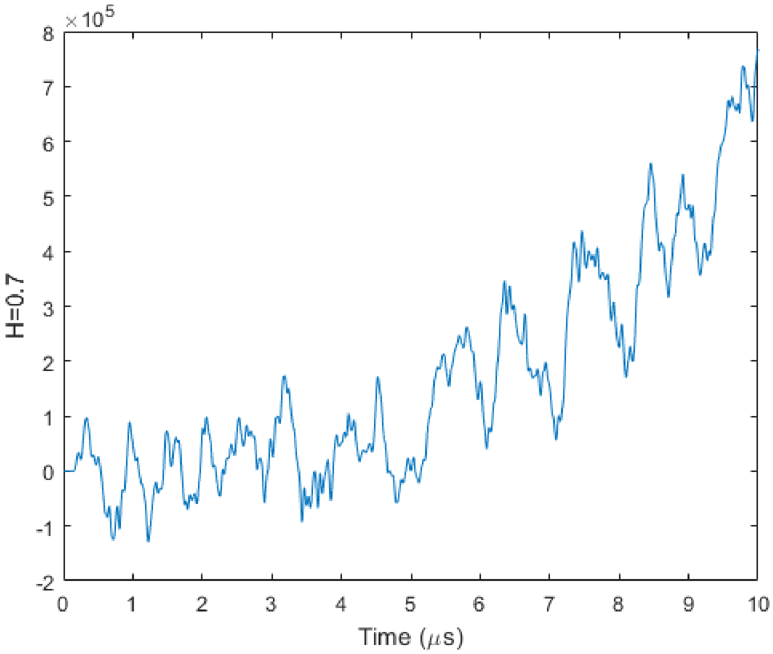

Figure A.4 – Example of an output signal of the simulations performed *via* SimSonic2D.

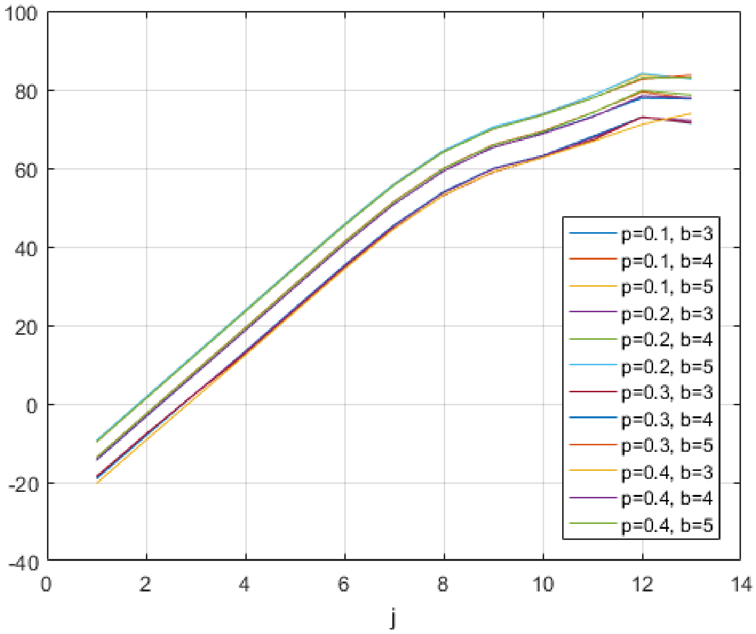

Figure A.5 – Structure functions (DWT) for q= 3.

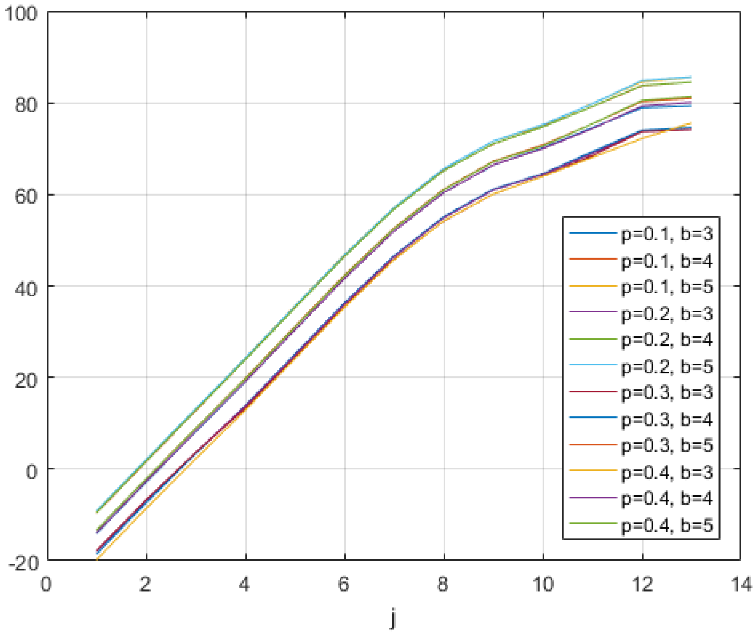

Figure A.6 – Structure functions (LWT) for q= 3.

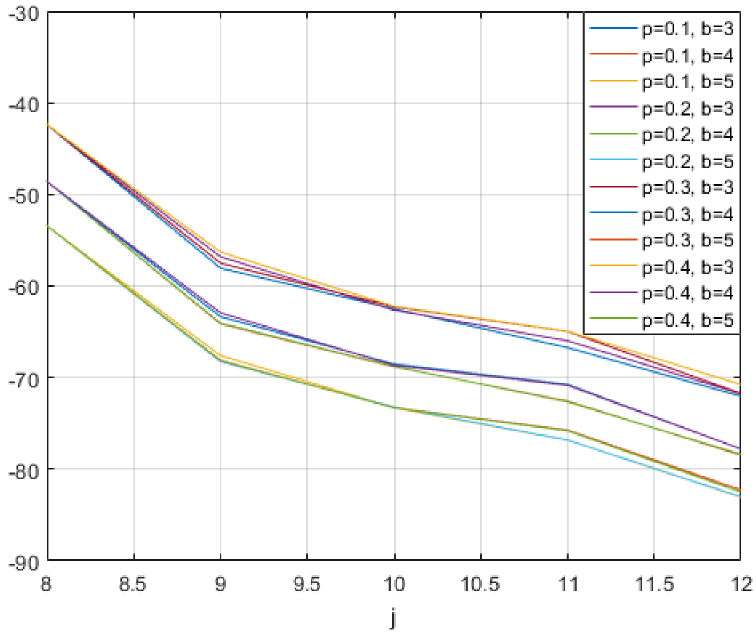

Figure A.7 – Structure functions (LWT) for q= -3.

A.6 Conclusion

This work aims at exploring and exploiting the multiscale structure of the ultrasonic signal *via* the multifractal analysis. With respect to the previous work presented in Chapter 4 [107], here, we investigate the ultrasonic wave propagation in a *fractal* geometry, where this ”fractality” has been added artificially in the mechanical model. As in the previous work, also here the multifractal spectra do not present a clair and/or discriminant behavior. Thus, we have focused again on the study of structure functions.

In particular, in this study, we test the variation of two fractals parameters (p and q) in the building of the geometry. The results are promising, since they allow to clearly discriminate the structure function with respect to the fractal scaling parameter b.

Now, we are interested in how they act. Thus, in further works, firstly some other family of fractals may be tested to ensure that these parameters are always discriminant or if we deal with something more complex. Also a formulation for the random case of the FD with respect to these two parameters is necessary.

List of Figures

List of Tables

List of publications and presentations

Publications

- I. Scala, C. Spingarn, Y. Rémond, A. Madeo and D. George. Mechanically-driven bone remodelling simulation: application to LIPUS treated rat calvarial defects. *Mathematics and Mechanics of Solids*, 22(10): 1976-1988, 2017.
- G. Rosi, I. Scala, V.-H. Nguyen and S. Naili. Wave propagation in strain gradient poroelastic medium with micro inertia: closed-form and finite element solutions. *Zeitschrift für angewandte Mathematik und Physik*, 68(3): 58,2017.
- I. Scala, G. Rosi, V.-H. Nguyen, R. Vayron, G. Haïat, H. Yahia, S. Seuret, S. Jaffard and S. Naili. Ultrasonic characterization and multifractal analysis for the evaluation of dental implant stability: a sensitivity study. *Biomedical Signal Processing & Control*, 42: 37-44, 2018.
- I. Scala, G. Rosi, L. Placidi, V.-H. Nguyen and S. Naili. Effects of the microstructure and density profiles on wave propagation across an interface with material properties. *Continuum Mechanics and Thermodynamics*, 1-16, 2019.

International congress with refereed proceedings

- G. Rosi, I. Scala, V.-H. Nguyen, S. Naili, R. Vayron, G. Haïat, H. Yahia, S. Seuret and S. Jaffard. Numerical simulations and multifractal signal processing used in ultrasonic characterization of bone-implant interface in case of dental implants. *Congrès Français d'Acoustique*, Le Mans (France), 11-15 april 2016.
- I. Scala, G. Rosi, V.-H. Nguyen and S. Naili. Closed-form and finite element solutions of wave propagation in strain gradient poroelastic medium with

micro inertia. *6th Biot Conference on Poromechanics*, Paris (France), 9-13 july 2017.

- I. Scala, G. Rosi, V.-H. Nguyen, S. Naili, R. Vayron, G. Haïat, S. Seuret and S. Jaffard. Evaluation of dental implant stability using ultrasonic characterization and multifractal analysis. *Congrès Français de Mécanique*, Lille (France), 28 aout - 1^{st} september 2017.

Poster

- I. Scala, G. Rosi and S. Naili. Ultrasonic gyroid scaffolds for bone tissue engineering. *8th World Congress of Biomechanics*, Dublin (Ireland), 8-12 july 2018.

Abstract

This thesis focus on the ultrasonic characterization of bone-implant *interphase*. This region is a transition zone where the osteointegration process (*i.e.* the healing process of the tissues surrounding the implant) takes place. Thus, this interphase is of crucial importance in the long-term anchorage of the implant, since it depends on the quantity and quality of the surrounding bone tissue. However, other than being a complex medium in constant remodeling, the newly formed bone presents a multiscale and time evolving nature. All these reasons make the characterization of the bone-implant interphase critical and difficult. In this context, ultrasound methods are nowadays widely used in the clinic field because of their ability to give information about the biomechanical properties of bone tissue.

On this basis, with the aim of characterizing the mechanical and microstructural properties of the bone-implant interphase by ultrasound methods, it is important to develop and validate mechanical models and signal processing methods. Due to the complexity of the problem, in order to precisely describe the bone tissue surrounding the implant, first an accurate modelling of bone tissue is essential. Thus, the interaction between an ultrasonic wave and bone tissue has been investigated by also taking into account the effects dues to the microstructure. To do this, a generalized continuum modelling has been used. In this context, a transmission/reflection test performed on a poroelastic sample dipped in a fluid enhanced the reliability of the model. The reflected and transmitted pressure fields result to be affected by the microstructure parameters and the results coming from the dispersion analysis are in agreement with those observed in experiments for poroelastic specimens. Then, the problem has been complicated by considering the interphase taking place between the bone and the implant. In this way, we could handle the complexity added by the presence of the newly formed tissue. As already said, the fact that this interphase is a heterogeneous medium, a mixture of both solid and fluid phases whose properties evolve with time is an additional difficulty. Thus, in order to model the interaction of ultrasonic waves with this interphase, a thin layer with elastic and inertial properties has been considered in the model. The effects on the reflection properties of a transition between a homogeneous and a microstructured continuum have been investigated.

Therefore, the characterization of the medium also *via* advanced signal processing techniques is investigated. In particular, the dynamic response due to the ultrasonic excitation of the bone-implant system is analyzed through the multifractal approach. A first analysis based on the wavelet coefficients pointed out a multifractal signature for the signals from both simulations and experiences. Then, a sensitivity study has also shown that the variation of parameters such as central frequency and trabecular bone density does not lead to a change in the response. The originality lies in the fact that it is one of the early efforts to exploit the multifractal approach in the ultrasonic propagation inside a heterogeneous medium.

Keywords: bone tissue, finite element method, interphase, multifractal analysis, second gradient, wave propagation

Résumé

Cette thèse se concentre sur la caractérisation ultrasonore de l'*interphase* os-implant. Cette région est une zone de transition où a lieu le processus d'ostéointégration (*i.e.* le processus de guérison du tissu entourant l'implant). Donc, cette interphase a un rôle crucial dans l'ancrage à long-terme de l'implant, puisqu'elle dépend de la quantité ainsi que la qualité du tissu osseux environnant. Ensuite, en plus d'être un milieu complexe en remodelage continu, l'os néoformé présente une nature multi échelle et qui évolue dans le temps. Toutes ces motivations rendent la caractérisation de l'interphase os-implant critique et difficile. Dans ce contexte, les méthodes ultrasonores sont largement utilisées aujourd'hui dans le domaine clinique pour leur capacité de donner des informations sur les propriétés biomécaniques du tissu osseux.
Compte tenu de ces éléments, dans le but de caractériser les propriétés mécaniques et microstructurales de l'interphase os-implant à travers des méthodes ultrasonores, il est important de développer et valider des modèles mécaniques ainsi que de méthodes de traitement du signal. A cause de la complexité du problème, afin de décrire avec précision le tissu environnant l'implant, il est d'abord essentiel une modélisation fiable du tissu osseux. Pour cela, on étudie l'interaction entre une onde ultrasonore et le tissu osseux, en considérant aussi les effets dus à la microstructure. Pour ce faire, un modèle continu généralisé a été utilisé. Dans ce contexte, un test de transmission/réflexion réalisé sur un échantillon poroélastique immergé dans un fluide a renforcé la fiabilité du modèle. Les champs de pression réfléchi et transmis sont influencés par les paramètres de la microstructure. De plus, les résultats issus de l'analyse de dispersion sont en accord avec ceux observés dans les expériences pour les échantillons poroélastiques. Après, le problème a été compliqué en considérant une interphase qui se situe entre l'os et l'implant. Ainsi, on peut gérer la complexité ajoutée par la présence du tissu néoformé. Comme on l'a déjà mentionné, une difficulté additionnelle est représentée par le fait que l'interphase est un milieu hétérogène, un mélange de phases solides et fluides dont les propriétés évoluent avec le temps. Donc, afin de modéliser l'interaction des ondes ultrasonores avec une interphase, on a considéré dans le modèle une couche très fine avec des propriétés élastiques et inertielles. En partant de ça, on a étudié les

effets des propriétés de réflexion d'une transition entre un milieu homogène et un milieu microstructuré.
De même, il a aussi été étudié la caractérisation du milieu *via* des techniques avances de traitement du signal. En particulier, la réponse dynamique due à l'excitation ultrasonore du système os-implant a été analysée à travers une approche multifractale. Une première analyse basée sur les coefficients des ondelettes a montré une signature multifractale pour les signaux dérivants des simulations et aussi des expériences. Ensuite, une étude de sensibilité a aussi montré que la variation des paramètres tels que la fréquence centrale et la densité de l'os trabéculaire ne contribue pas à un changement dans la réponse. L'originalité réside dans le fait qu'il s'agit d'un des premiers efforts d'exploiter l'approche multifractale dans la propagation ultrasonore dans un milieu hétérogène.

Mots clés : analyse multifractale, interphase, méthode des éléments finis, propagation d'onde, second gradient, tissu osseux